Investigations of Ultra Shallow Junction Ion Implanted Biaxial Tensile Strained Silicon by means of X-Ray, Raman and Photoacoustic Techniques

by

Ken Horan *B.Sc. M.Eng.*

Dublin City University

School of Electronic Engineering
Research Supervisor

Prof. Patrick J. McNally

Thesis submitted for the degree of Doctor of Philosophy

2012

The most exciting phrase to hear in science,
the one that heralds the most discoveries,
is not "Eureka!" but "That's funny..."
-Isaac Asimov

Declaration

I hereby certify that this material, which I now submit for assessment on the programme of study leading to the award of Ph.D. is entirely my own work, that I have exercised reasonable care to ensure that the work is original, and does not to the best of my knowledge breach any law of copyright, and has not been taken from the work of others save and to the extent that such work has been cited and acknowledged within the text of my work.

Signed: ..... (Candidate)

ID No.: 56211315

Date: .....

Acknowledgements

My Ph.D. research experience is one which will not soon be forgotten. The last four years have been characterised by often-times excruciating frustration, punctuated by moments of clarity. For all that however, it has been a period of commensurate rewards and enlightenment.

For affording me the opportunity to undertake such an edifying venture, I am indebted to Prof. Patrick McNally. This is to say nothing of his ceaseless support, direction and (at times most important) patience over the years of the project. Immense as Prof. McNally's contribution was however, he is far from the only one to whom I owe thanks.

Dr. Lisa O'Reilly, in her capacity as the post doctoral researcher on the project provided day-to-day guidance and support throughout, and her arrangement of sample sourcing and processing was critical.

Dr. Nick Bennett and Prof. Nick Cowern are owed a deep debt of gratitude for their assistance with sample annealing and electrical characterisation. For the ion-implantation I thank Prof. Russell Gwilliam. Dr. Bennett was also responsible for the arrangement of the SIMS data reported herein and for this I additionally thank him.

The interpretation of SXRT images can by times seem a black art. The evaluation of the topographs collected over the course of the project was assisted immensely (whether directly or indirectly) by discussions with some of the most distinguished and prolific experts in the

field, with whom I have been privileged to work. These include Prof. Turkka Tuomi, Dr. Andreas Danilewsky, Prof. Brian Tanner and Prof. McNally himself. Special thanks are also owed to Dr. Aapo Lankinen in regard to x-ray measurements, for both his interpretive contributions and early HR-XRD measurements, which, although not reported on herein, were crucial in the early stages of the project.

The help and support of my colleagues in DCU has been invaluable. My great appreciation goes to the technical staff including Mr. Robert Clare and Mr. Billy Roarty, whose help at critical times throughout the project was invaluable. Special thanks in this matter are owed to Dr. Jennifer Stopford, Dr. Philip Perry and Dr. Lu Xu for their help with the PAS system. Finally in this category come my fellow NPL research students. The shared experiences of countless frustrations, tool failures and undergrad tutorials, along with the odd success, will not be forgotten. Of special note are my office-mates, Aidan Cowley, Jen Stopford, Monjarul Alam, Dave Allen, Rajani KV and Stuart Corr.

On a personal note I wish to thank both my parents and my long suffering girlfriend. My parents have been supportive of all my decisions in life (letting me dig my own hole by times), and for this I thank them. Without their support I could not have achieved half as much. Finally, to Danielle, for her immense patience, understanding and consideration, I owe tremendous thanks and say,

"It's done!"

Contents

Abstract

The application of strain to the active channel region of the metal-oxide-semiconductor-field-effect-transistor (MOSFET) has become a necessary practice in integrated circuit (IC) fabrication. The introduction of strain allows increased carrier mobilities, and concomitant device performance enhancements, which are independent of MOSFET scaling. Biaxial tensile strained silicon (ε-Si), resulting from epitaxial growth of silicon on a $Si_{1-x}Ge_x$ virtual substrate gives rise to enhanced electron mobilities and, for certain dopants, increased electrical activation. For these reasons it is the material of interest in this thesis.

The prospects for industrial implementations of ε-Si are heavily dependent on the effects of device processing steps, and the controllability of defect and dopant profiles. Of special interest to the current work is the suitability of ε-Si subjected to low energy antimony implants and low thermal budget rapid thermal anneal (RTA), for the production of ultrashallow, abrupt junctions, appropriate for future generation source-drain extensions (SDE).

Examined in the wider project are the effects of strain on dopant activation and diffusion through Differential Hall and SIMS measurements carried out by project partners. These measurements provide context for the work herein and demonstrate the desirability of ε-Si as a n-MOSFET channel material.

For our part, the effects of implant and anneal processes are investigated through both high

resolution x-ray diffraction and micro-Raman (μ-Raman) spectroscopy. Synchrotron x-ray topography is used to identify the strain relaxation processes in both the ε-Si epilayer and the $Si_{1-x}Ge_x$ virtual substrate.

Data obtained during the project called into question the validity of traditional μ-Raman interpretations in the context of degenerately doped silicon, under these conditions additional theoretical considerations are necessary. The μ-Raman data presented herein demonstrates sensitivities to both implant damage and to dopant activation and these dependencies are theoretically accouncted for.

Finally, Photoacoustic Spectroscopy is shown to be a technique capable of non-destructive detection of ion implant damage within the top $\sim$10 nm of the silicon. These uniquely sensitive measurements araise due to the particular experimental set up used which invoke a strong dependence on the thermal interface resistance within the sample.

Table of Acronyms

4PP	4 Point Probe
ANKA	Angstroemquella Karlsruhe
b	Burgers Vector
BRST	Back Reflection Section Topography
CB	Carbon Black
CCC	Channel Cut Crystal
CCD	Capacitively Coupled Device
CMP	Chemical Mechanical Polishing
DCA	Dual Channel Analyzer Crystal
E	Energy
ε-Si	Biaxially Tensile Strained Silicon
EDRc	Enhanced Dynamic Range Detector
EF	Fermi Energy
EM	Electro Magnetic Radiation
F-D	Fermi Dirac
FR	Frank Read Source
G	Gibb's Free Energy
He-Cd	Helium-Cadmium
HR-XRD	High Resolution X-Ray Diffraction

IC	Integrated Circuit
ITRS	International Technological Roadmap for Semiconductors
LABRT	Large Area Back Reflection Topography
LAT	Large Area Transmission
MD	Misfit Dislocations
MFR	Modified Frank Read Source
MOSFET	Metal Oxide Semiconductor Field Effect Transistor
$\mu - Raman$	micro Raman
NUV	Near Ultraviolet
OD	Optical Density
PA	Photoacoustic
PAS	Photoacoustic Spectroscopy
PCL	Phonon Coherence Length
PCM	Phonon Coherence Model
RG	Rosencwaig and Gersho
RSF	Relative Sensitivity Factors
RSM	Reciprocal Space Map
RTA	Rapid Thermal Anneal
SDE	Source/Drain Extensions
SF	Stacking Faults
SHO	Simple Harmonic Oscillator
SiGe	Silicon Germanium
SIMS	Secondary Ion Mass Spectroscopy
SPER	Solid Phase Epitaxial Regrowth
ST	Section Transmission
SXRT	Synchrotron X-Ray Topography

TED	Transient Enhanced Diffusion
SRIM	TRansmission of Ions in Matter
ULE	Ultra Low Energy
VG	Gate Voltage
VS	Source Voltage
VS	Virtual Substrate
XRD	X-Ray Diffraction
XRT	X-Ray Topography

Table of Symbols

Symbol	Assignment	Context
$\mathbf{a}, \mathbf{b}, \mathbf{c}$	crystal lattice translational vectors	XRD
a	thermal diffusion coefficient	Photoacoustics
	lattice constant	General
α	angle between substrate [001] direction and the surface normal	XRD
	molecule's polarizability	Raman
	thermal diffusivity	Photoacoustics
a_c	hydrostatic conduction band deformation potential	Electrical Conductivity
B	magnetic field	Electrical Conductivity
	isothermal bulk modulus	Photoacoustics
$\mathbf{b}$	Burgers vector	General
β	angle between epilayer [001] direction and surface normal	XRD
	optical absorption coefficient	Photoacoustics
C	concentration	SIMS
	elastic constant tensor	Raman
	lattice stiffness tensor	Dopant Activation
C_p	specific heat capacity (constant pressure)	Photoacoustics
C^{ss}	dopant solid solubility	Electrical Conductivity
Δ	valley degeneracy	Electrical Conductivity

Symbol	**Assignment**	**Context**
d	inter-planar spacing	XRD
D	shear strain deformation potential	Raman
D_0	phonon deformation potential	Raman (Carrier Density)
$D(\omega)$	density of states per unit volume	Raman (Carrier Density)
E	electric field of incident radiation	Raman (Classical)
	energy	Raman (Quantum)
	energy	General
ε	strain	General
E_F	Fermi energy	General
E_f	Young's Modulus	Raman
$E_G(0)$	average transition energy	Raman (Carrier Density)
F	force	General
$\mathbf{G}$	reciprocal lattice vector	XRD
γ	relative angle between the substrate and epilayer [001] directions	XRD
	specific heat ratio	Photoacoustics
Γ_0	natural linewidth	Raman
η	refractive index	Raman
h	Planck,Äôs constant	General
	thickness	General
I	current	Electrical Conductivity
	ion current	SIMS
	intensity	Raman/Photoacoustics
$\mathbf{k}$	wave-vector	XRD/Raman
k	Boltzmann's constant	General
κ	thermal conductivity	Photoacoustics

Symbol	**Assignment**	**Context**
L	phonon coherence length	Raman
λ	wavelength	General
m	lattice misfit	Raman
M	silicon atomic mass	Raman (Carrier Density)
μ	carrier mobility	Electrical Conductivity
	chemical potential	Dopant Activation
	chemical potential	Electron Energy
	optical absorption coefficient	XRD/SXRT
	dipole moment	Raman
	thermal diffusion length	Photoacoustics
$\hat{\mathbf{n}}$	crystal plane normal vector	XRD
N	number of unit cells per volume	Raman (Carrier Density)
n-	n-type	General
ν	frequency	Raman
	Poisson's Ratio	Raman
	carrier drift velocity	Electrical Conductivity
N_d	carrier density	General
p	pressure	Photoacoustics
p-	p-type	General
p, q, r	phonon deformation potentials	Raman
q	electronic charge	Electrical Conductivity
Q	atomic displacement along the normal co-ordinate relative to the equilibrium position	Raman
$\mathbf{r}$	lattice vector	XRD
R	resistance	Electrical Conductivity
	degree of relaxation	XRD

R	Raman Tensor	Raman
ρ	density	Photoacoustics
$\rho(\mathbf{r})$	electron probability density	XRD
R_H	Hall Coefficient	Electrical Conductivity
R_{therm}	thermal reflection coefficient	Photoacoustics
S	lattice stiffness tensor	Raman
σ	stress	General
	conductivity	Electrical Conductivity
	wave-vector	Photoacoustics
t	thickness	XRD
T	temperature	General
τ	Stress	Dislocation Dissociation
θ	detector angle	XRD
t_p	penetration depth	SXRT
T_{therm}	thermal transmission coefficient	Photoacoustics
V	voltage	Electrical Conductivity
	volume	Dopant Activation
V_G	gate voltage	General
ϕ	specimen angle rotating about the surface normal	XRD
	specimen angle rotating about the horizontal	XRD
Ψ	molecular vibration wavefunction	Raman
	thermal energy	Photoacoustics
ω	specimen angle rotating about the vertical	XRD
	energy $[cm^{-1}]$	Raman

Chapter 1

Biaxial Tensile Strained Silicon

The application of strain to the active channel region of the metal-oxide-semiconductor-field-effect-transistor (MOSFET) has become a necessary practice in integrated circuit (IC) fabrication. This has largely been in reaction to short-channel effects and the architectural and processing changes they have necessitated. The sense of strain used (tensile/compressive) is determined by the band structure deformation required, e.g. tensile (compressive) strain is generally used to enhance *n*- (*p*-) channel MOSFET performance. The stressor employed is determined by the dimensionality (uniaxial/biaxial) and extent (local/global) of the required strain. In the case of global biaxial tensile strain (considered in the current work) the common stressor is a $Si_{1-x}Ge_x$ virtual substrate (VS), with an x-dependent lattice constant.

The global nature of the $Si_{1-x}Ge_x$ virtual substrate makes its incorporation into current complementary-metal-oxide-semiconductor (CMOS) processing practices challenging due to the disparity of the resulting *n*- and *p*- type conductivity enhancements. As a result, current applications tend to employ local solutions such as nitride capping layers (tensile) or source/drain implants (compressive) [1]. The prospect of dual-channel devices however may allow the benefits of the additional strain available through the use of virtual substrates to

be reaped. In addition to this, the fact that the strained layer remains exposed in the VS configuration, allows the possibility of increased dopant activation, detailed later.

The extent of industrial implementation of biaxial tensile strained silicon (hereafter referred to as strained silicon or ε-Si), epitaxially grown on $Si_{1-x}Ge_x$ virtual substrates is heavily dependent on the effects of device processing steps, and the controllability of defect and dopant profiles. Of special interest to the current work is the suitability of ε-Si combined with low energy antimony implants and low thermal budget rapid thermal anneal (RTA), for the production of ultrashallow, abrupt junctions, appropriate for future generation source-drain extension (SDE) production.

1.1 History of Strained Silicon

CMOS Scaling

Today's computing technology is the culmination of almost 70 years of academic, military and industrial research efforts. From the vacuum tube computing of the 1940s, to today's proliferation of compact computers and "smart phones", capable of feats not even envisaged 20 years ago, the semiconductor industry is arguably the most progressive and fast moving industry in the world. Major milestones along this development path include the discovery of the "point contact transistor" by Bardeen, Brattain and Shockley in 1947 (the discovery earned the three the 1956 Nobel prize in physics), Kahng and Atalla's production of the first operational MOSFET in 1960 [2], and the invention of the integrated circuit (IC), (invented independently by Kilby and Noyce in 1958 and 1959, respectively - Kilby received the Nobel prize in physics in 2000 for the invention).

Since its invention, IC development has been characterized by an exponential growth in com-

puting power and an exponential reduction in cost per function. These enhancements have largely been commensurate with the scaling of the fundamental component - the MOSFET.

MOSFETs are used as the building blocks of ICs. The specific materials and fabrication practices have evolved over the years, however the general construction and principles of MOSFET operation have changed little since its invention. MOSFETs can be used as amplifiers, however in the majority of today's ICs they are switching elements [3].

Since the 1960's, the density of MOSFETs on a chip has been characterized by the self fulfilling prophesy referred to as "Moore's Law" in which Gordon Moore predicted that the density of transistors would double every 12 months; his initial prediction referred to the decade up to 1975 [4] and figure 1.1a is a reproduction of a graph from his original paper. In 1975 Moore revised the intergenerational period to 24 months [5], [6]. Figure 1.1b demonstrates the validity of this revised "law" over the past 4 decades.

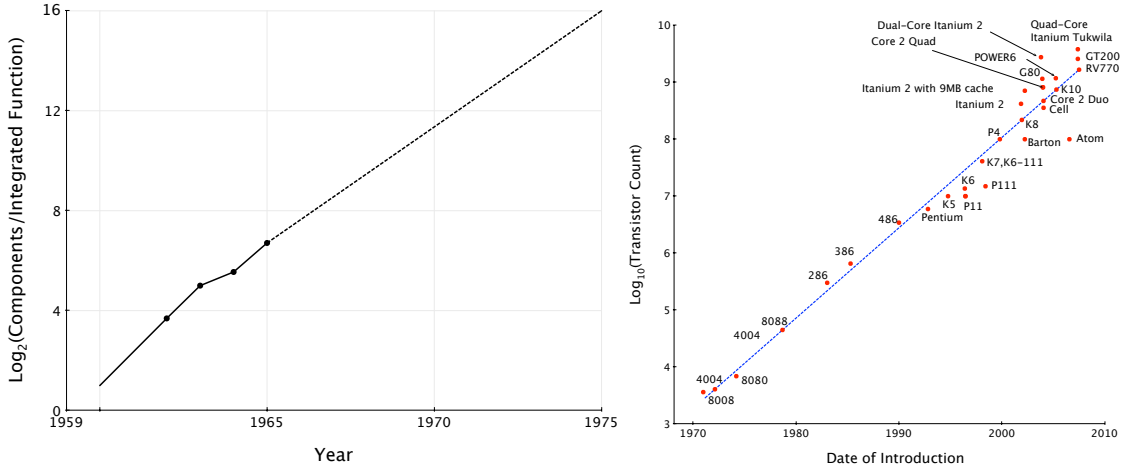

(a) (b)

Figure 1.1: (a) Gordon Moore's originally predicted component density trend for the years 1965 - 1975 [4]. (b) Demonstration of the validity of Moore's Law (revised) over the past 40 years. The red dots, represent the Intel chip-sets and the dashed blue line exhibits Moore's revised law [5,6].

End of Commensurate Enhancements

Over the past two decades it has become apparent that the continued scaling of the MOSFET alone will increasingly fail to provide the commensurate performance enhancements enjoyed through-out the 60's, 70's and 80's. During this era development relied largely on advances in lithography technology. In the current era however, additional obstacles have emerged exemplified by short-channel effects. One of the most prominent short channel effects is Drain Induced Barrier Lowering (DIBL), which results in a reducing effective channel length. At its extreme, this effect can be summarized as the loss of transistor action due to overlapping source and drain space-charge regions, figure 1.2 depicts this concept.

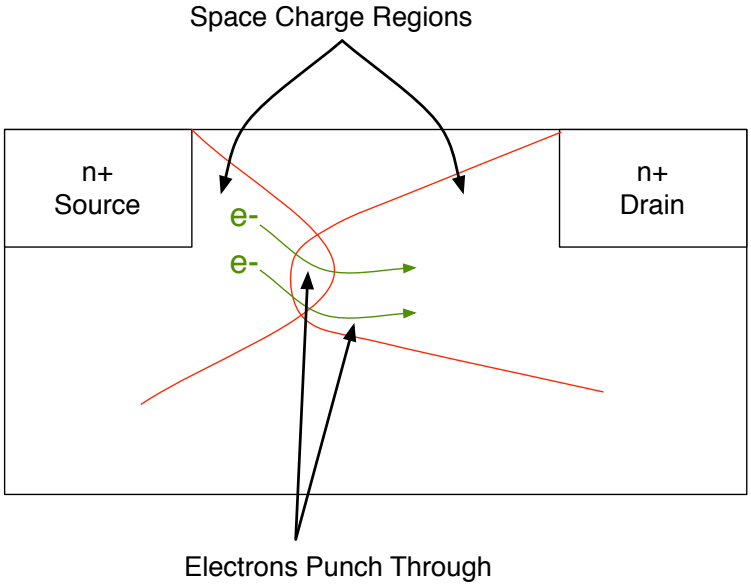

Figure 1.2: Drain Induced Barrier Lowering : As the potentials applied to the source and drain contacts increase, the drain space charge region reduces the potential on the gate electrode required to for the channel inversion layer. At its ultimate extent, the source and drain space-charge-regions come in contact and electrons are provided a conduction channel and "punch through".

In order to limit the extent of the source and drain space-charge regions, additional doping has been introduced into the channel region. This doping however introduces problems of its own, the most significant of which is the necessity to operate the device under conditions of increased gate voltage (V_G). This operation at higher vertical electric fields results in a loss of electron mobility due to increased scattering; initially by acoustic phonon scattering and at even higher effective fields, by surface roughness scattering [7]. Figure 1.3 shows the "universal mobility curve" depicting the effect of increased vertical electric fields on the electron mobility in inversion MOSFETs. The effects of surface roughness scattering in region 3 of figure 1.3, can be reduced somewhat by planarization techniques e.g. chemical mechanical polishing (CMP), however the phonon scattering of region 2 is an intrinsic process. These reductions in mobility need to be counteracted in order to maintain acceptable MOSFET transductance characteristics, thus, a high mobility alternative to bulk silicon has become increasingly necessary.

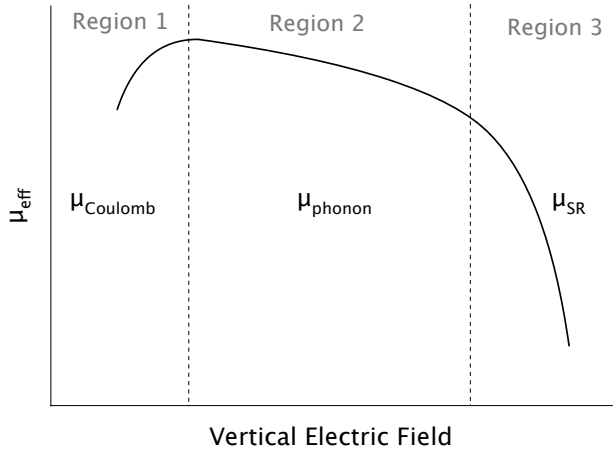

Figure 1.3: Universal mobility curve for bulk Si inversion MOSFETs from [7]. At low vertical voltages, Coulombic forces dominate scattering events. In the intermediate regions electron-phonon scattering becomes important and drives the electron mobility down. Finally at high vertical electric fields the conduction electrons become confined at the device surface and surface scatternig becomes the dominant factor.

Biaxial Tensile Strained Silicon

It is against this backdrop that ε-Si technology has advanced as it provides device performance enhancements independent of scaling. Initially this performance enhancement manifested itself as an increased conduction electron mobility, but subsequently, improved dopant activation and diffusion properties have also become evident.

n-Type Devices

In 1985 Abstreiter *et al.* [8] identified the 2 dimensional electron gas (2DEG) nature of conduction in ε-Si pseudomorphically grown on $Si_{1-x}Ge_x$ virtual substrates. He also identified the lifting of the threefold degeneracy of the conduction band. Abstreiter's ε-Si however was so densely populated by defects that the increased scattering resulted in electron conductivities worse than those of bulk silicon.

In 1991, Fitzgerald *et al.* [9] introduced the concept of compositional grading in the $Si_{1-x}Ge_x$ virtual substrate. This technique reduced the dislocation density in the active ε-Si region by 2 orders of magnitude ($10^8 cm^{-2}$ to $10^6 cm^{-2}$) and over a period of two years made possible dramatic improvements in low temperature (4 K) electron mobilities in ε-Si (19,000 cm^{-2}/Vs to 96,000 cm^{-2}/Vs [9] and subsequently up to 170,000 cm^{-2}/Vs [10]).

In 1998 it was demonstrated that the incorporation of CMP into the growth process could reduce the threading dislocation density by a further order of magnitude in buffer layers graded to pure Ge [11].

Two years after the introduction of ε-Si growth on compositionally graded SiGe, Welser *et al.* reported the first MOSFET based on this technology [12]. Welser's MOSFET was based on a $Si_{0.71}Ge_{0.29}$ VS. It was an n-type MOSFET and demonstrated effective mobilities

70% greater than those of bulk Si n-MOSFETs. Welser followed this work with a systematic examination of the effect of strain on electron mobility by fabricating MOSFETs on $Si_{1-x}Ge_x$ VS with $x = 0.1 - 0.37$ [13]. This study showed the effective electron mobility enhancement factor ($\mu_{strained}/\mu_{bulk}$) saturated at a value of 1.8×, at a VS Ge content of ∼20%.

In 1998, Rim *et al.* [14] demonstrated the advantages of ε-Si in device structures by revealing a 45% enhancement in transductance. In contrast to the devices previously investigated, these n-MOSFETs were short-channel devices with channel lengths of 0.1 μm. The high doping in the channel, necessary to suppress short channel effects at this channel length, required very high effective fields, however n-channel mobility enhancements of 75% (over control bulk Si devices) were still observed in the ε-Si inversion layers.

p-Type Devices

It should be pointed out that research efforts were also invested in ε-Si [15], ε-Ge [16], and ε-$Si_{1-x}Ge_x$ [17]p-MOSFET performance, in parallel to the n-MOSFET, with varying degrees of success. Nayak showed in 1993 that the gate overdrive in these devices needed to be sufficiently high so as to avoid hole confinement at the ε-Si/ε-$Si_{1-x}Ge_x$ interface, however Nayak *et al.* subsequently revealed that at high gate overdrive levels the hole mobility in the ε-Si layer actually drops below that of bulk Si [18]. Thus, while ε-Si can provide hole mobility enhancements (40-50% [18], [15]), these enhancements are subject to strong dependences on gate overdrive. Greater success has been shown in compressively strained Ge and $Si_{1-x}Ge_x$ materials. This led to the development of structures comprising of a ε-Si capping layer and buried ε-$Si_{1-x}Ge_x$ channel. This structure provided greatly improved enhancements in hole mobility (4-5 ×) [19]. Lee *et al.* took this heterostructure to its conclusion by employing ε-Si/ε-Ge on relaxed $Si_{1-x}Ge_x$ ($x = 0.7 - 1.0$) virtual substrates [20] and attained peak hole mobility enhancements of 8×, with minimal variation with respect to gate overdrive.

Recent Work

More recent research into *n*-channel ε-Si/$Si_{1-x}Ge_x$ structures has focused on industrial integration and scalability. To this end, interest turned to the effects of industrial processing on ε-Si and the effect of strain on critical dopant properties. In 1996, Kringhoj *et al.* [21] experimentally demonstrated the retardation of Sb diffusion in ε-Si, an effect previously predicted in theoretical work by Cowern [22].

In 2002, Sadigh *et al.*, while investigating boron activation in compressively strained silicon postulated the enhanced activation of *n*-type dopants, more specifically antimony, in tensile strained silicon [23], a postulate confirmed experimentally by Bennett *et al.* [24], [25], although the mechanism of this enhancement is different to that put forward by Sadigh [26].

Also in 2002, work carried out in the University of Warwick revealed the benefits of terrace graded virtual substrates by growing virtual substrates through alternating graded and constant composition layers. In this structure, the relaxation proceeds in the graded layers, with the uniform layers localizing threading dislocations and dispersing dislocation pile-ups [27].

Current Work

The source/drain extensions of future generation MOSFETs will require the production of ultrashallow (<10 nm), abrupt junctions [28]. Consideration of the previously cited literature, suggests that a combination of ε-Si and antimony may be appropriate for the production of such features in *n*-MOSFETs. The current work aims to investigate this proposition by examining future scale source/drain extensions in one dimension. More specifically, the effects of low energy antimony implantation and low thermal budget RTA on strain relaxation, and

the effects of strain on dopant activation are investigated across a range of strain levels, implant doses and anneal temperatures.

Owing to observations made during the process of the thesis, the viability of μ-Raman spectroscopy as a strain characterisation technique is investigated in the context of future device dimensions and doping levels. Additionally, photoacoustic spectroscopy is advanced as an alternative means of nondestructive, qualitative characterisation of post implant damage.

1.2 Mechanics of Strained Silicon

Pseudomorphic Growth

Strain can be imposed on silicon in a number of ways depending on the sense (compressive/tensile) and dimensionality (uniaxial/biaxial) required. The current work is concerned with strain imposed by psuedomorphic heteroepitaxial growth.

In a heteroepitaxial growth process a material of lattice constant a_0 is deposited on a crystal of lattice constant a, where $a \neq a_0$. Under the correct conditions, if the lattice misfit ($|a - a_0|$) is sufficiently small the first atomic layer deposited will adhere to the lattice constant of the substrate, i.e. the layer will be strained, figure 1.4 demonstrates this concept.

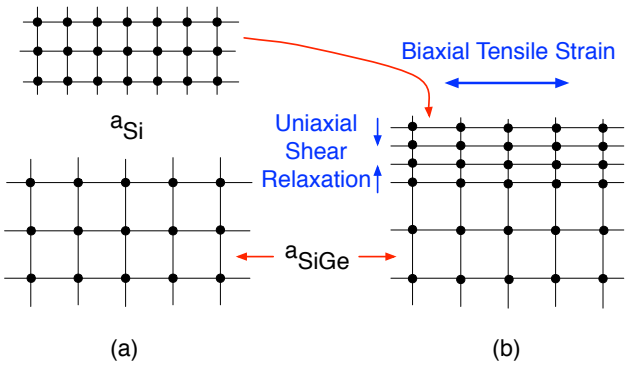

Figure 1.4: Pseudomorphic growth of ε-Si on $Si_{1-x}Ge_x$. (a) The lattice constant of $Si_{1-x}Ge_x$ (a_{SiGe}) is greater than that of Si (a_{Si}). (b) During pseudomorphic growth, the deposited Si layer conforms to the lattice constant of the underlying $Si_{1-x}Ge_x$ virtual substrate in the in-plane dimensions. Lattice energy is minimized through shear relaxation in the out-of-plane dimension.

In the current work, a layer of silicon ($a_{Si} = 5.436A$) is deposited on a $Si_{1-x}Ge_x$ virtual substrate of fractional germanium content x. The lattice constant of germanium ($a_{Ge} = 5.646A$) is larger than that of silicon. The lattice constant of the binary virtual substrate is approximated by a linear interpolation between the lattice constant of Si and that of Ge (Vegard's Law [29]),

$$a_{Si_{1-x}Ge_x} = (1-x)\, a_{Si} + (x)\, a_{Ge} \tag{1.1}$$

It should be noted that parabolic deviations from Vegard's Law have been reported and are well documented [30], [31], however these deviations have been shown to be small and to have little effect on results. For a fully pseudomorphically strained layer, this leads to an in-plane strain of [31],

$$\varepsilon_{||} = \frac{a_{Si_{1-x}Ge_x} - a_{Si}}{a_{Si}} = 0.042x \tag{1.2}$$

The strain imposed on the silicon capping layer is hydrostatic in the plane of growth, however silicon is a Poisson material, and the energy of the lattice is minimized through the shear

uniaxial compression in the out-of-plane direction [23]. This out-of-plane strain is given by [31],

$$\varepsilon_{\perp} = -\varepsilon_{\parallel} \frac{2\nu}{1-\nu} \tag{1.3}$$

where ν is Poisson's ratio for silicon. The combination of these processes leads of an overall tetragonal distortion of the lattice. This tetragonal distortion breaks the cubic symmetry of the lattice, and, as will be demonstrated subsequently, has dramatic effects on the material properties.

Stress Relaxation

Strain related stress inherently introduces the prospect of instability in a structure. In a crystalline structure, stress can be accommodated by elastic strain and/or by misfit dislocations, as shown in figure 1.5. It has been demonstrated that, for a given misfit strain, pseudomorphic growth continues only to a certain "critical thickness" above which, stress relaxation through the formation of misfit dislocation segments becomes energetically favorable [32], [33], [34].

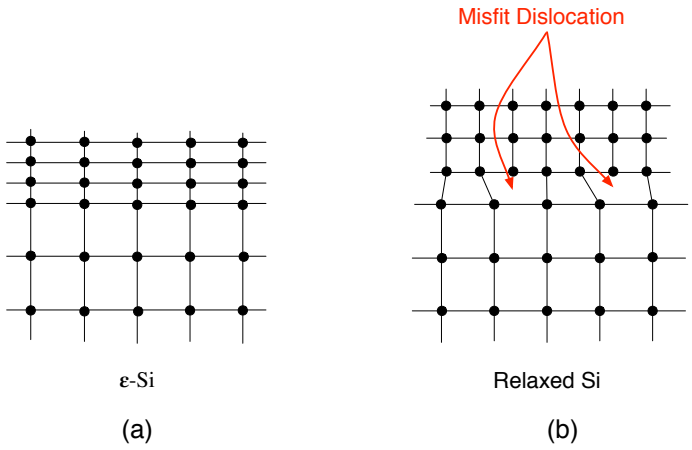

Figure 1.5: Stress accommodation by (a) elastic strain and (b) misfit dislocation.

Dislocations in crystalline silicon are of three main types, edge (dislocation line direction perpendicular to Burgers vector), screw (dislocation line direction parallel to Burgers vector) and 60° mixed (line direction at a 60° angle to Burgers vector) [34], [35], where the Burgers vector describes the lattice distortion due to the dislocation. Of these three dislocation types (depicted in figure 1.6 [36]), edge dislocations have the greatest nucleation energy and screw dislocations cannot relieve tetragonal stress, therefore the most common type of dislocation responsible for stress relaxation in ε-Si is the 60° mixed type [34], [37]. In silicon and other diamond-structure materials, these dislocations lie in the $\langle 110 \rangle$ directions and glide along $\{111\}$ planes. For the remainder of this discussion it is assumed that the dislocations in question are of the 60° mixed type.

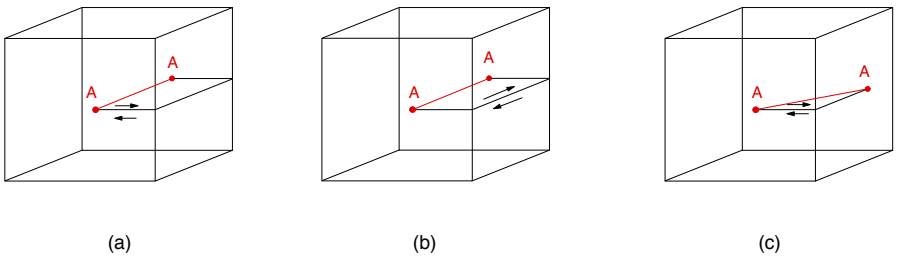

Figure 1.6: Schematic representation of the three types of dislocations to be found in diamond-structure crystals. Line AA represents the dislocation line. (a) if the atoms above the dislocation are shifted in a direction perpendicular to AA an edge dislocation is formed; (b) if the shift is parallel to AA, a screw dislocation results and (c) a shift at some arbitrary angle (neither perpendicular nor parallel) a mixed-type dislocation is formed [36].

Dislocation Glide

Initial considerations of strain relaxation put forward by Van der Merwe [38] and Matthews & Blakeslee [32] were based on the principle of the mechanical equilibrium of in-grown

threading dislocations and their subsequent glide. The basic principle of these treatments is depicted in figure 1.7 [33], where F_{stress} is the force exerted by the background stress field (proportional to the layer thickness and the square of the strain) and F_{self} is an attractive force between the dislocation and the free surface (resulting from a reduction of the stored energy of the dislocation due to the increasingly compliant material in the vicinity of the free surface). When $F_{stress} < F_{self}$ the material is stable and strain relaxation is energetically prohibited. Van der Merwe defined the critical thickness as that at which $F_{stress} = F_{self}$. This equivalence however is nominal only, as there are other contributory factors e.g. the Peierls-Nabarro stress (a periodic stress arising from the discrete nature of the material at the dislocation's core, depicted in figure 1.8 [36]). Beyond this thickness, if growth continues, the situation arises in which F_{stress} is sufficiently greater than F_{self}, that the threading dislocation advances, extending a strain relieving misfit segment in its wake.

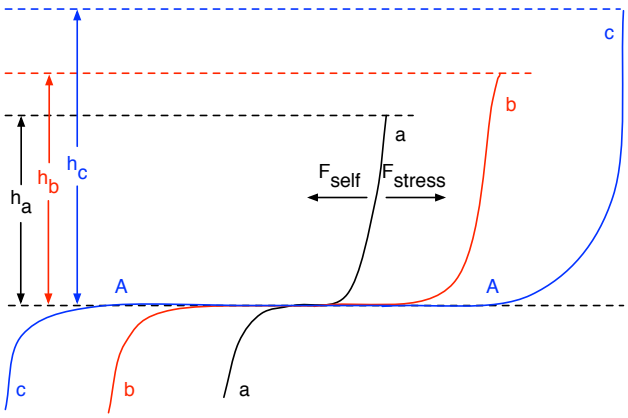

Figure 1.7: Elongation of a threading dislocation, leading to the formation of a misfit segment AA. h_a is sub-critical resulting in no glide of the dislocation, h_b is equal to the critical thickness and dislocation glide begins. Once growth proceeds to h_c, the critical thickness has been surpassed and F_{stress} dominates the force balance extending the interface misfit dislocation [33].

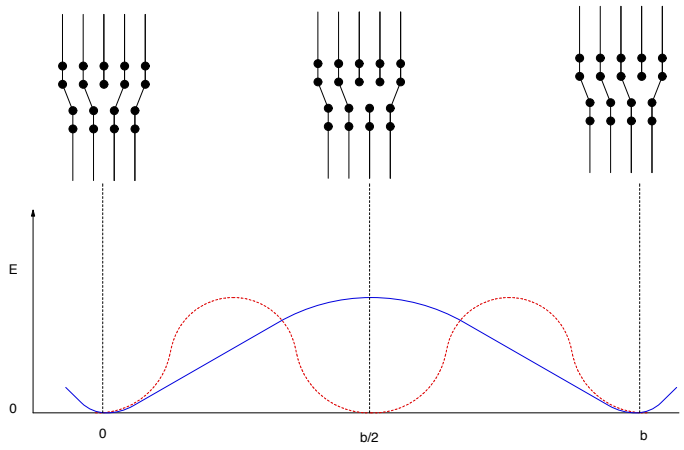

Figure 1.8: Peierls-Nabarro periodic stress arising from the quantized nature of the crystal in the vicinity of the dislocation core. Shown are two periodic energy variation scenarios [36]. The red dotted line represents the motion of a disociated dislocation, whereas the blue solid line represents the motion of a pure dislocation.

While giving insight into some of the mechanics of strain relaxation, this treatment is predicated by a requirement of high in-grown threading dislocation densities, a situation which is rare in modern single crystal silicon, dislocations must thus be nucleated before glide can proceed.

Dislocation Nucleation

The strain energy which can be relieved by dislocation glide is limited by the dislocation density and the average dislocation glide distance. Modern growth techniques limit in-grown threading dislocation densities and largely suppress the previously described effects in as-grown strained crystals. Relaxation of stress thus necessitates dislocation nucleation. Two main sources of dislocations present themselves; dislocation half-loops and modified Frank-Read sources.

Dislocation Nucleation by Surface Half-Loops

Heterogeneous Nucleation

In modern crystals there is a low but finite density of pre-existing defects, precipitates and other impurities. These inclusions result in localized stress gradients, which under the influence of, for example thermal cycling, can exceed the dislocation formation energy of the crystal in question. Due to the increased compliance of a free surface, this formation energy is reduced in this vicinity, thus making nucleation sites on a free surface more likely. After formation, the dislocation expands under the influence of the formative force.

Upon intersection with the underlying epilayer/substrate interface a misfit segment forms as the stress field drops to zero beyond this interface. At this intersection, in addition to the misfit segment, threading dislocations are formed on either end of the misfit. These separate, extending the strain relieving misfit segment, and assuming they are not blocked, exit the crystal. This process is depicted in figure 1.9 [34].

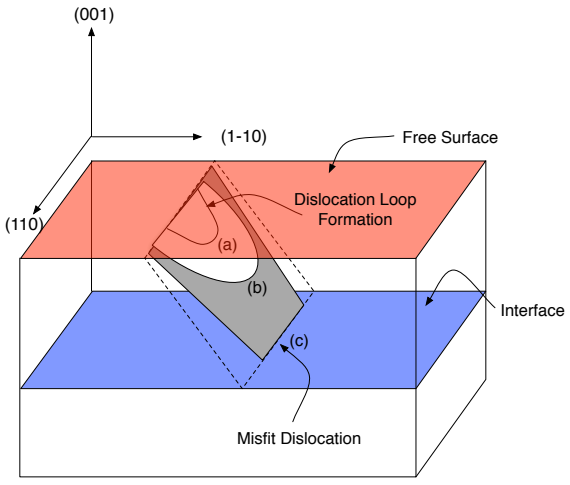

Figure 1.9: Process of half-loop dislocation formation (a) dislocation nucleation, (b) dislocation expansion,(c) intersection with interface resulting in formation of misfit segment and threading segments [34].

Homogeneous Nucleation

Homogeneous nucleations are spontaneous processes resulting within an ideally perfect crystalline region and are characterized by extremely large activation energies. The dearth of defect and particulate dislocation activation sites in modern crystalline materials implies that in many regions of the crystal, half-loop nucleation should proceed via these extremely high-energy homogeneous processes. This requirement is generally relaxed in real crystals however by the presence of surface cross-hatch and through dislocation dissociation.

Surface Crosshatch

Surface morphology can provide an alternate means of stress relaxation. It has been shown that a transition from Frank-van der Merwe growth to Stranski-Krastanow growth, can, under certain conditions, be energetically favourable in strained epilayers [39]. This results because the unconstrained surfaces of the island formations provide elastic relaxation, which can outweigh the increased surface energy [39], [40]. These energy losses result in the introduction of a periodic surface roughness [31]. This surface roughness generally manifests itself in a cross-hatch pattern of V-shaped trenches [41]. Over the majority of the structure, the material experiences relaxation, however at cusps between islands, there is an increased stress due to the elastic distortion of vertical lattice planes (depicted in figure 1.10 [39]). These cusps act as "stress-concentrators" [42], preforming a role similar to that of the inclusions mentioned previously.

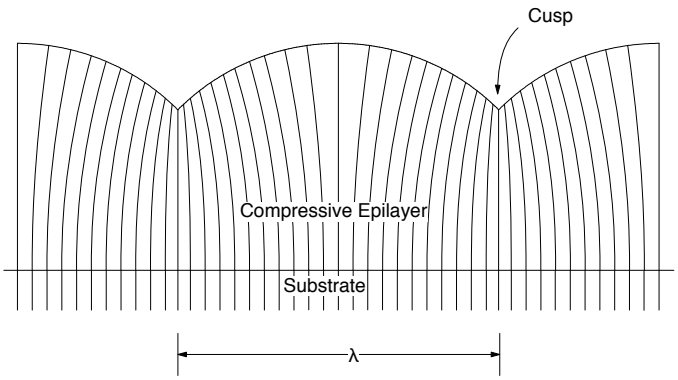

Figure 1.10: Formation of islands in strained epitaxial material, can result in strain relaxation through lateral dilation of the lattice at the unconstrained surfaces. At the cusps between islands however, this dilation results in increased stress [39].

Dislocation Dissociation

Dislocation dissociation is the process by which the displacement vector of a dislocation is decomposed into lower energy components. The proportionality of a dislocation's energy to the square of its Burgers vector ($E \propto \mathbf{b}^2$) means that such a dissociation reduces the overall energy of the dislocation. Because $\mathbf{b} = 1/2\langle 110 \rangle$ is the smallest perfect Burgers vector in diamond structure materials, dissociation of 60° mixed dislocations results in the formation of partial dislocations (90° partial and 30° partial). Figure 1.11 [34] exemplifies the process.

The anisotropy of the effective forces acting on the partials shown in figure 1.11 introduces the possibility of stacking fault formation and differentiates between the critical thickness of a compressively strained layer and that of an equally strained tensile layer.

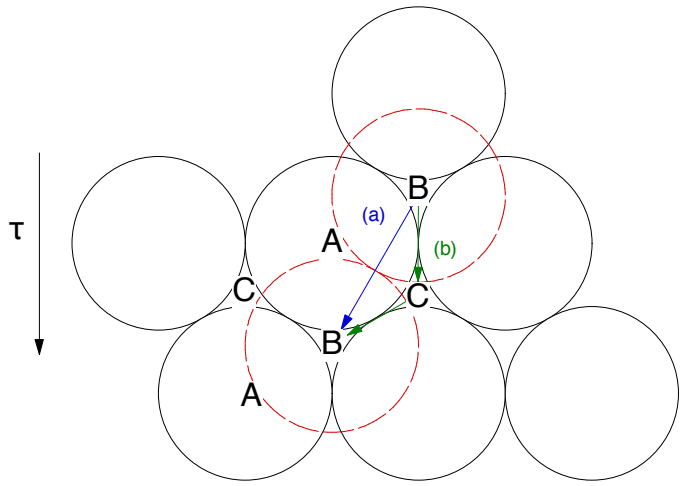

Figure 1.11: Dissociation of pure 60° dislocation into partial 30° and 90° dislocations. A, B and C are atomic stacking positions, i.e. the lattice changes from an AB stacking configuration to an AC configuration during dissociation. (a) and (b) represent the perfect and dissociated slip vectors. τ is the applied stress (in this case tensile) [34].

In order for dissociation to occur, the first partial to nucleate must be the 90° component. Under tensile stress (depicted in figure 1.11) this partial experiences a larger effective force and therefore is activated at a critical thickness below that of the 30° partial. This situation can lead to a stacking fault being introduced between the 90° partial critical thickness and that of the annihilating 30° partial. Compressive stress reverses this situation, requiring at least the activation energy of the 30° partial before dislocation nucleation can proceed. Under this condition however, the 90° partial follows immediately and no stacking fault can be formed. Thus the sense of the stress determines whether dislocation nucleation begins at the activation energy of the 90° partial (tensile) or that of the 30° partial (compressive).

Modified Frank-Read Mechanism

Frank-Read Sources

Before the modified Frank-Read mechanism can be considered, the traditional Frank-Read (FR) mechanism must first be reviewed. The Frank-Read mechanism is one by which a single dislocation can multiply, giving rise to a series of dislocation loops which continue to be produced as long as the driving force remains.

During its motion through a crystal lattice, a dislocation can move between parallel glide planes (climb or jog) and during these processes the dislocation can become pinned; if this happens, a FR source is formed. The immobile dislocation is subject to the same stress field as previously, but now this force's effect is to warp the dislocation as depicted in figure 1.12. At some point, the dislocation turns back on itself and eventually the two ends meet to form a closed dislocation loop as well as reforming the original dislocation. The closed loop expands until it reaches the surface, where two threading arms are formed, these separate, thus expanding a misfit dislocation segment. Due to the reformation of the original dislocation, the process repeats itself.

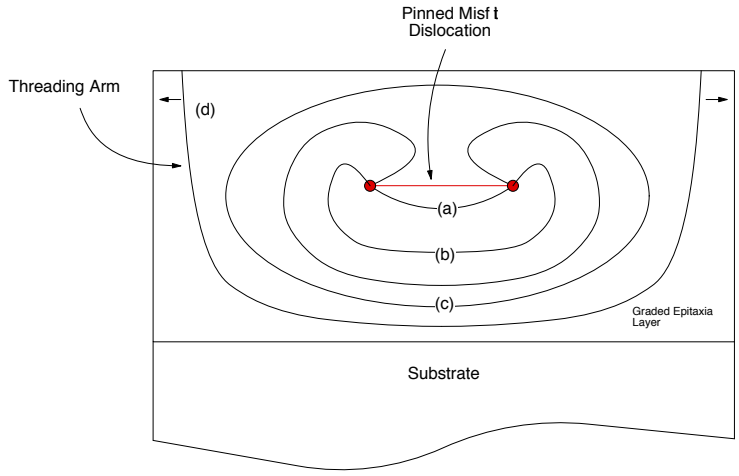

Figure 1.12: Frank Read dislocation source: Once a dislocation becomes pinned, the stress field acts to warp the dislocation. The dislocation will eventually turn back on itself sufficiently to create a closed loop, in addition to this closed loop, the original dislocation is reformed. As the closed loop expands, it reaches the layer interfaces and forms misfit and threading segments. The process repeats itself as long as a sufficiently large background stress field exists.

Modified Frank-Read Sources

The modified Frank-Read (MFR) dislocation source can arise due to the blocking interaction between an existing interfacial misfit dislocation and an approaching threading arm.

Upon production of a misfit segment, the elastic energy in its immediate vicinity is lowered. The implication of this, is that as a threading dislocation approaches an existing misfit dislocation, its mechanical equilibrium becomes altered. This can result in the threading dislocation being blocked. If the interacting dislocations have the same Burgers vector, the dislocations split, forming two dislocations, each containing a 90° bend. Figure 1.13 (a)

depicts a threading dislocation moving along its glide plane towards a preexisting misfit dislocation and (b) depicts the post-annihilation configuration [42].

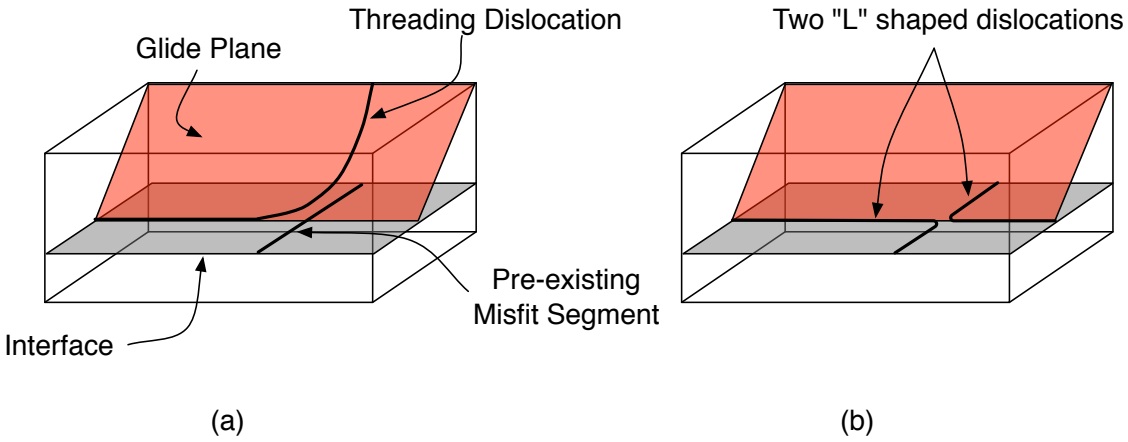

Figure 1.13: (a) Threading dislocation moving in its glide plane toward a preexisting interface misfit dislocation. Strain relaxation in the vicinity of the misfit segment alters the mechanical equilibrium, if this reduction in stress energy is sufficient, the threading dislocation will cease gliding, (b) under correct conditions, dislocations with parallel Burgers vectors meeting in such a way that will split forming two dislocations each containing a 90° bend [42].

The interaction of dislocations implies an additional contributory force in their mechanical equilibrium; the interaction force. This interaction force acts to minimize the length of the dislocations in question, thus, progression of the dislocation requires strain relaxation in addition to dislocation shortening. If the two L-shaped dislocations are considered to form a local system of quadrants, these criteria are satisfied in only one of the four quadrants, where both the interaction and stress forces are directed toward the substrate, figure 1.14 demonstrates this principle.

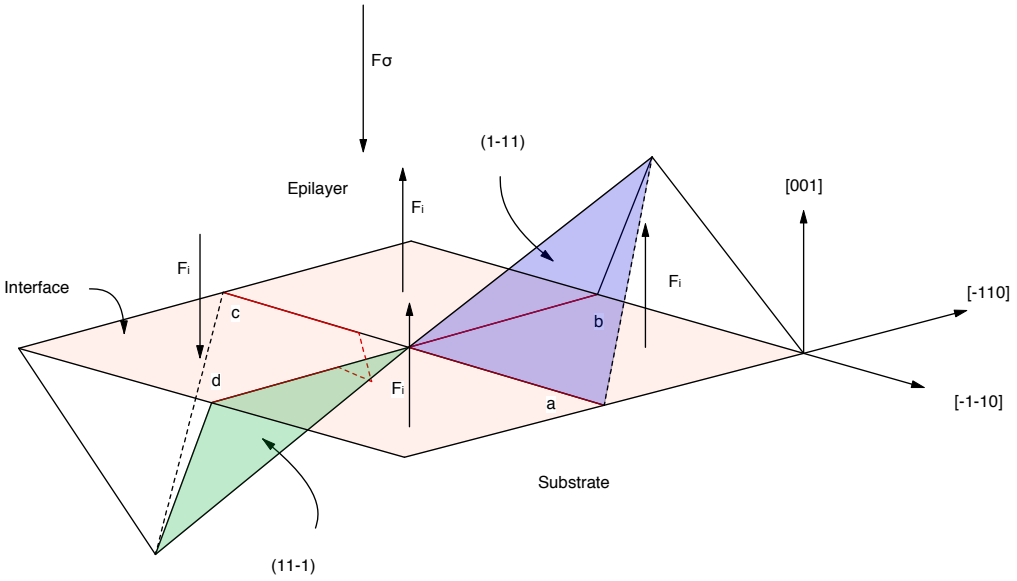

Figure 1.14: After the formation of two "L" shaped dislocations, the interaction force between the two dislocations acts to minimize their lengths. The stress force remains pointed towards the substrate. In only one quadrant do these forces act together, resulting in one of the dislocation corners being pushed into the substrate [42].

If the stress field continues to increase, the declined tip expands on the two intersecting glide planes and curls back on itself in a fashion similar to the Frank-Read source. When the back-curling expansions meet at the common line between the two planes, a dislocation loop is formed, in addition to the reformation of the original declined dislocation tip. This loop then expands until it reaches the surface where two threading arms are formed and separate, forming misfit dislocations on the same glide planes as the parent dislocations but spatially separated from them [43]. This process is depicted in figures 1.15 (a-d).

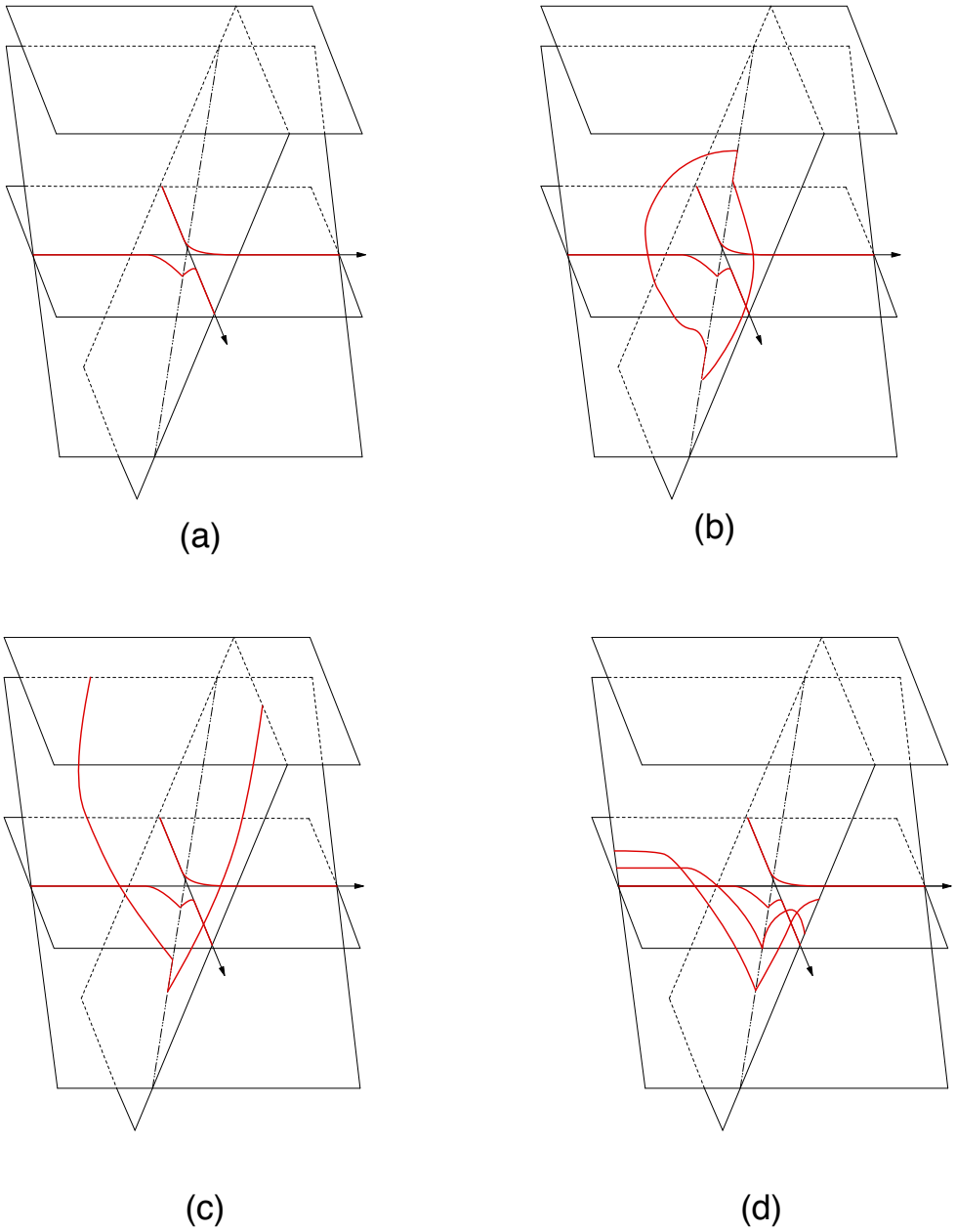

Figure 1.15: (a) The corner of one of the misfit dislocations is pushed into the substrate. (b) The inclined tip expands on the two intersecting glide planes and forms a closed loop at the line common to the planes. (c) The dislocation loop expands to the surface at which point threaders are formed and separate forming misfit dislocations. (d) The repeated reformation of the dislocation results in a build-up of misfit dislocations below the MFR source [43].

The repeated dislocation formation and downward turning of one of the corners results in a dislocation pile-up under the MFR source. Each dislocation introduces a small step on the sample surface, therefore this pile-up of dislocations can lead to large undulations on the semiconductor surface which are deleterious to processing registry. In addition to this, any threading dislocations approaching this misfit pile-up will be halted resulting in a threading dislocation pile-up and the necessity for the production of new mobile threading dislocations. This threading dislocation pile-up is detrimental to device performance giving rise to large leakage currents.

Layer Grading

Over the past couple of decades, the methods of virtual substrate growth have evolved. There have been three major methods used during this period: constant composition, step/linear grading and terrace grading. This section aims to give an overview of the principles of, and dominant relaxation processes in, each.

Constant Composition

Initial growth of virtual substrates was performed on the basis of a constant composition virtual substrate. Simply, this is an above critical thickness deposition of a material with the required lattice constant e.g. $Si_{0.7}Ge_{0.3}$. In this case, once dislocations become energetically favorable, surface half-loops nucleate and generate misfit dislocations as described previously. This mechanism of nucleation, in this type of material, results in co-planar misfit dislocations with a high probability of mobility suppressing interactions. This limits the strain relieving efficiency of individual misfit segments, requiring the nucleation of new dislocations. In addition to this, blocking interactions prevent the threading components of the dislocations from gliding to the sample edges, therefore, these materials are characterised by extremely high threading dislocation densities.

Step & Linearly Graded Composition

In a step graded virtual substrate, the final lattice constant is achieved through a series of layers with incrementally increasing lattice constant. This allows the misfit dislocations necessary for strain relaxation to be spread over multiple interfaces, thus reducing their density on any individual plane. The natural evolution of this method is to increase the number of steps in the process, thus progressively reducing the interface misfit dislocation densities. This evolution leads logically to the linearly graded VS, a system in which, theoretically, each atomic layer can constitute a step.

The resulting dispersion of misfit dislocations reduces the density of orthogonal dislocation interactions. This reduces the threading dislocation density as it maximizes the number of threaders reaching the crystal edges and minimizes the number of nucleation events necessary for strain relaxation.

The predominant strain relaxation mechanism in these layers is the MFR mechanism. This shift in paradigm can be explained by means of the critical "pinning" distance. This minimum distance between dislocation pinning points arises through the relation, $\tau = {}^{Gb}/_{L}$, where τ is the shear stress required to activate a FR source, G is the shear modulus, b is the dislocation Burgers vector and L is the distance between the pinning events [43].

Terrace Graded VS

Terrace grading in virtual substrates aims to reap the benefits of linearly graded layers (low threading dislocation densities) while suppressing the problematic dislocation pile-ups and surface undulations associated with their relaxation. A virtual substrate of this kind is made up of alternating layers of linearly graded and constant composition $Si_{1-x}Ge_x$. Strain relaxation in these structures occurs predominantly in the linearly graded layers, thus reducing the density of threading dislocations. The constant composition layers separate the MFR

multiplication sources. This necessitates the development of new sources in each subsequent graded layer, and limits the degree of dislocation pile-up at each source. The resulting dispersion of pile-up sources reduces the amplitude of the surface crosshatch associated with relaxation of linearly graded $Si_{1-x}Ge_x$ layers as demonstrated in figure 1.16 [27].

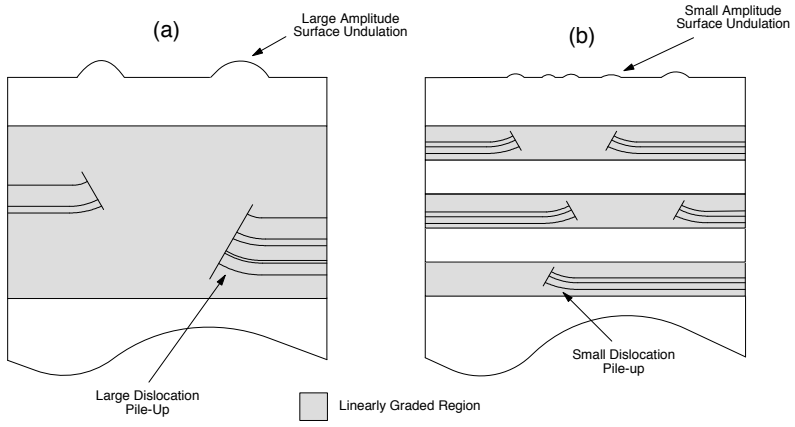

Figure 1.16: Reduction of dislocation pile up resulting from terrace graded $Si_{1-x}Ge_x$ structure. (a) Large dislocation pile up within linearly graded virtual substrate, (b) introduction of periodic constant composition layers suppresses the magnitude of individual pile-ups [27].

Lattice Tilt

The previously discussed mechanisms of strain relaxation involve the formation and expansion of 60° mixed dislocations. For these individual dislocations within diamond structure materials, eight slip systems exist, four for each dislocation direction (parallel to [110] and $\left[1\bar{1}0\right]$) [44]. Given that the MFR mechanism involves the co-evolution of orthogonal dislocations this number of slip systems reduces to four when considering this mechanism, these are detailed in table 1.1 [45].

Slip Systems for Independent Relaxation	Dislocation line	Glide Plane	Burgers Vector	Slip System for MFR Relaxation
G1	$[110]$	$(1\bar{1}\bar{1})$	$\frac{1}{2}[101]$	MFR1
G2	$[\bar{1}10]$	$(11\bar{1})$		
G3	$[110]$	$(1\bar{1}1)$	$\frac{1}{2}[10\bar{1}]$	MFR2
G4	$[\bar{1}10]$	(111)		
G5	$[\bar{1}\bar{1}0]$	$(1\bar{1}1)$	$\frac{1}{2}[011]$	MFR3
G6	$[\bar{1}10]$	$(11\bar{1})$		
G7	$[\bar{1}\bar{1}0]$	$(1\bar{1}\bar{1})$	$\frac{1}{2}[01\bar{1}]$	MFR4
G8	$[\bar{1}10]$	(111)		

Table 1.1: Slip systems of individual dislocations and modified Frank Read sources within silicon [45].

The 60° mixed dislocations considered presently can be decomposed into a combination of a misfit component, a screw component and a tilt component. Taking MFR1 of table 1.1 as an example, the Burgers vector is decomposed as follows,

$$\frac{1}{2}[101] = \frac{1}{4}[1\bar{1}0] + \frac{1}{4}[110] + \frac{1}{2}[001] \tag{1.4}$$

where, for the portion of the corner parallel to [110], $\frac{1}{4}[1\bar{1}0]$ is the misfit component, $\frac{1}{4}[110]$ is the screw component and $\frac{1}{2}[001]$ is the tilt component, producing tilt about [110]. For the concomitant corner portion, $\frac{1}{4}[1\bar{1}0]$ is the screw component, $\frac{1}{4}[110]$ is the misfit component and $\frac{1}{2}[001]$ remains the tilt component but this time the tilt is about $[1\bar{1}0]$. Taking this system as a whole and assuming symmetric expansion of the two portions, the misfit components relieve misfit stress, the screw components counteract each other resulting in zero net twist and the tilt components combine to result in a tilt around [100]. This intra-

slip-system non-zero net out-of-plane Burgers vector, requires the symmetric production and expansion of the MFR2 slip-system of table 1.1 in order to result in zero macroscopic tilt. Similar arguments apply to the MFR3/MFR4 system combination. Within a planar growth process, the production of dislocations should remain symmetrical, however should there be a departure from planar growth, asymmetries can be introduced.

Figure 1.17 depicts a stepwise hetero- interface where the epitaxial layer is assumed to be under tensile stress. As the stress forces acting on a pair of glide systems is related to the degree of constraint of the local region, at the step edge the asymmetric reduction in lattice constraint across the two glide systems results in the asymmetric production of dislocations across the two. The nature of the constraint asymmetry causes the sense of the misfit dislocation tilt component to oppose the coherent tilt [45].

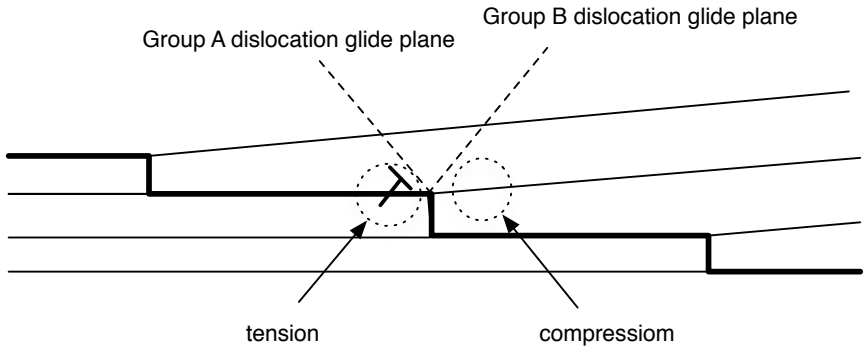

Figure 1.17: The asymmetric reduction in constraint at a step edge results in asymmetric production of misfit dislocations in oppositely sensed dislocation slip systems [45].

The step-wise interface depicted in figure 1.17 can result from lattice miscut or island formation. The long range coherence of a miscut introduces an additional inherent macroscopic tilt component. Figure 1.18 demonstrates these two tilt sources.

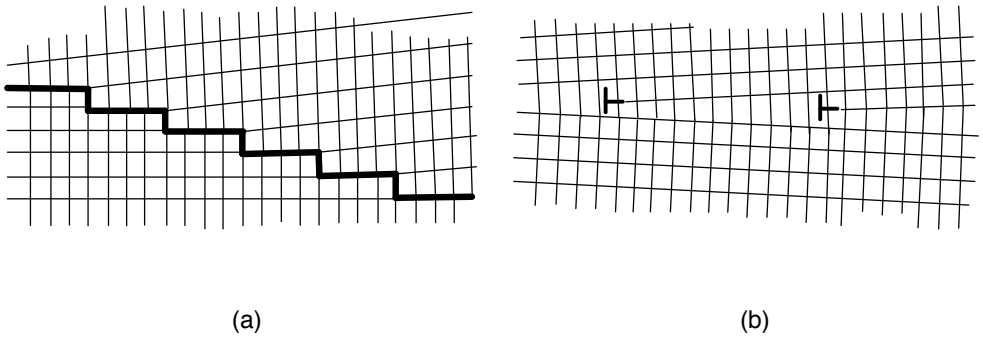

Figure 1.18: Tilt sources within epitaxial layers. (a) Coherent tilt due to lattice miscut. (b) Misfit dislocation array with net non-zero out-of-plane Burgers vector [45].

1.3 Theory of Strained Silicon

Band Structure of Strained Silicon

Bulk crystalline silicon has six conduction band valleys located on the three equivalent $\langle 100 \rangle$ axes in k-space, 85% of the way between the Brillouin zone center and its edge. Heteroepitaxial growth of ε-Si on a $Si_{1-x}Ge_x$ virtual substrate imposes a tetragonal distortion on the crystal lattice. This tetragonal distortion comprises of both hydrostatic and shear uniaxial components. Concomitant with each of these is a change in the band structure of the material. Figure 1.19 shows qualitatively, the contributions of hydrostatic and uniaxial shear strain to the energy levels of the six-fold degenerate silicon conduction band.

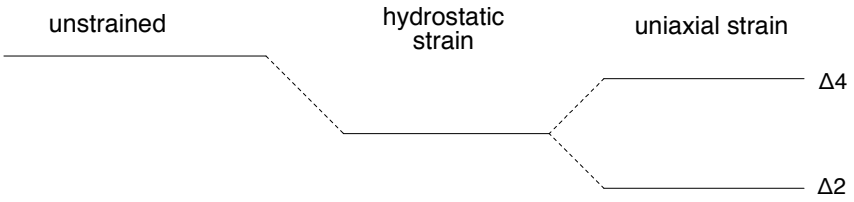

Figure 1.19: Schematic diagram of the contributions of hydrostatic and uniaxial strain to the energy levels of the bottom of the silicon conduction band.

Hydrostatic Strain

Hydrostatic strain accompanies a change in the material volume i.e. expansion or contraction. The nature of this strain is such that it results in a uniform shift of the six-fold degenerate conduction band (causes no lifting of the band degeneracy). In the case of ε-Si the conduction band energy shift is negative and its magnitude is given by [46],

$$\Delta E_{ch} = a_c \frac{\Delta V}{V} = a_c \left(2\varepsilon_{\parallel} + \varepsilon_{\perp}\right) = 2\varepsilon_{\parallel} \frac{1-2\nu}{1-\nu} a_c \tag{1.5}$$

where a_c is the hydrostatic conduction band deformation potential, and all other terms are as previously defined.

Shear Strain

Unlike hydrostatic strain, shear strain does lift the six-fold degeneracy of the conduction band as it breaks the cubic symmetry of the lattice. This deformation raises the energy

of the four in-plane $\langle 100 \rangle$ valleys with respect to the two out-of-plane $\langle 001 \rangle$ valleys by an amount $\Delta E_{cu} = 0.67x\ eV$, where x is the fraction of germanium in the virtual substrate [47], [48]. Subsequent to these energy shifts, the chemical equilibrium of the valleys is restored by the redistribution of the conduction electrons. The redistribution results in the preferential occupation of the out-of-plane $\langle 001 \rangle$ valleys, which, as will be demonstrated subsequently, results in large enhancements in the effective electron mobility of ε-Si. Figure 1.20 demonstrates the effect of shear strain on the silicon conduction band.

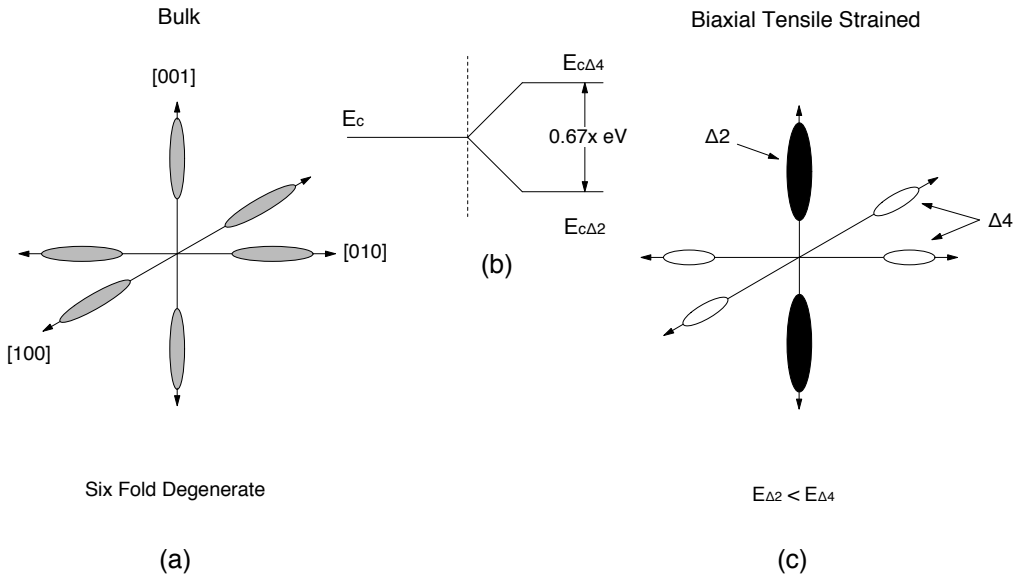

Figure 1.20: (a) Bulk silicon's six conduction band valleys lying in the mutually perpendicular $\langle 100 \rangle$ directions. (b) The shear component of the biaxial tensile strain lifts the six-fold energy degeneracy, the energy of the four in-plane energy valleys is raised and that of the two out-of-plane valleys is lowered. (c) The shift in the energy levels initiates a repopulation of the valleys favoring the lower energy Δ_2 valleys. Throughout the figure, the shading of valleys is indicative of relative population [46].

Electron Mobility in Biaxial Tensile Strained Silicon

The electron mobility improvements associated with strained silicon at room temperature and above are the result of two effects stemming from the lifting of the sixfold degeneracy in the silicon conduction band. These effects are the reduced effective mass of conduction electrons and the suppression of intervalley phonon scattering [49], [20], [47].

Conduction Electron Effective Mass

The surfaces of constant energy of the silicon conduction valleys are prolate spheroids, giving rise to an anisotropic effective mass, $m_l = 0.91m_0$ and $m_t = 0.19m_0$ (where m_0 is the rest mass of the electron and m_l and m_t are the effective masses of conduction electrons traveling parallel and perpendicular to the major axis of the valley) [47]. Thus for electrons drifting in a [100] orientated electric field, the effective mass of the conduction electrons will be a weighted combination of these masses [20],

$$m^* = \left[\frac{1}{3m_l} + \frac{2}{m_t}\right]^{-1} \tag{1.6}$$

The previously mentioned preferential occupation of the out-of-plane $\langle 001 \rangle$ valleys, leads to a reduction in the effective mass of electrons exposed to in-plane electric fields. The effective conductivity mass ratio (assuming x is large enough to fully populate the $\langle 001 \rangle$ valleys) between bulk and strained silicon, is given by [47],

$$r = \left(m_l^{-1} + 2m_t^{-1}\right)/3m_t \tag{1.7}$$

Equation (1.7) is sufficient to account for the conductivity differences between the materials at low temperatures, e.g. 77 K [47], however at higher temperatures the suppression of intervalley phonon scattering becomes relevant.

Intervalley Phonon Scattering Suppression

Electron-phonon scattering processes in crystalline silicon can be broken down into two general categories: inter- and intra-valley scattering. Intervalley scattering is sub-categorized into f- and g- type scattering [47] (f-type involves a change of the electron's orientation i.e. from longitudinal to transverse or vice-versa, g-type does not [50]). Figures 1.21 (a) & (b) show the scattering mechanisms from (a) the lower energy out-of-plane valleys and (b) the higher energy in-plane valleys. The scattering mechanisms shown in figure 1.21 (a) & (b) dominate the conductivity of silicon at room temperature [47].

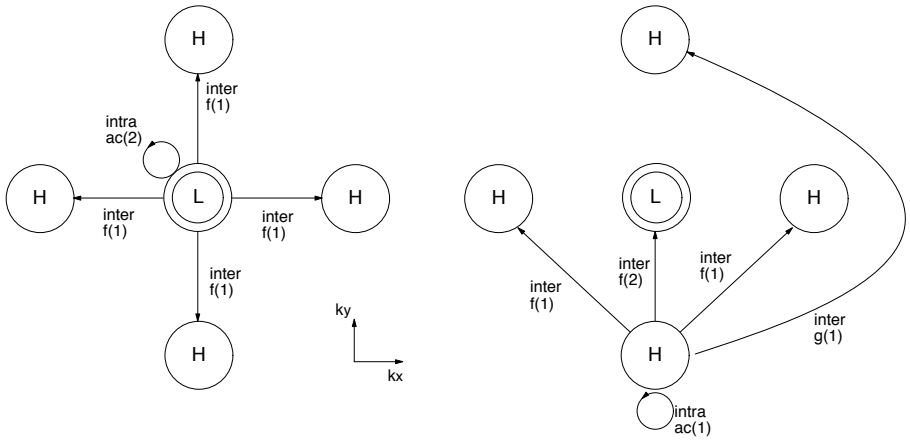

Figure 1.21: Scattering mechanisms from (a) the lower energy out-of-plane valleys and (b) the higher energy in-plane valleys [47]. Within the figure, intra and inter denote intra- and inter- valley scattering processes, respectively; ac, f and g descriptors stand for acoustic, f-type intervalley scattering and g-type intervalley scattering, respectively; and H and L indicate the relative energies of the valleys within biaxial tensile strained silicon, H meaning higher, L meaning lower.

Intra-valley phonon scattering is dominated by acoustic phonons and figure 1.21 labels them as such. These phonon modes are very low energy, low momentum and they therefore

dominate low temperature silicon conductivity. Parenthetically, there is another intra-valley scattering process which involves high energy, low momentum optical phonons [50]. The second order nature of these scattering events however precludes any appreciable effect they may have on electron conductivity in silicon [51], they are mentioned here only in the context of consistency, as they give rise to the Raman effects introduced in chapter 5.

At room temperature, the higher energy phonon modes become sufficiently populated to contribute significantly to conduction electron scattering. As such, inter-valley scattering by high energy, high momentum optical phonons must be considered; indeed at room temperature their contribution to silicon conductivity is comparable to intra-valley acoustic phonon scattering [48].

At room temperature, the lifting of the energy degeneracy of the six conduction band valleys results in a suppression of the inter-valley scattering due to an effective reduction in the density of destination states. This means that at room temperature there is an additional conductivity improvement.

Dopant Activation

In addition to increased electron mobility, the conductivity of ε-Si can benefit from increased activation of certain dopants. Initial investigations by Sadigh [23] revealed increased activation for boron dopants in biaxial compressive strained silicon. These activation enhancements were attributed to the combined effects of local strain relaxation due to the incorporation of the smaller boron atoms in the lattice and the strain induced increase of the crystal's Fermi energy (E_F). In this work, the Fermi energy shift was shown to be the dominant effect, accounting for $\sim$90% of the activation enhancement. Similar effects for n-type dopants in ε-Si have been demonstrated by Adey *et al.* [52]. These results however are based on

Maxwell-Boltzmann (M-B) statistics, making their applicability to degenerately doped materials questionable. More recent considerations by Diebel [53] and Ahn *et al.* [26], couched in Fermi-Dirac (F-D) statistics, produce qualitatively similar predictions, attributing however, the increased solid solubility almost entirely to volumetric rather than chemical effects.

In the work of Ahn *et al.* the strain dependence of the solid solubility is given by [26],

$$\frac{C^{ss}\left(\overrightarrow{\varepsilon}\right)}{C^{ss}\left(0\right)} = \exp\left(-\frac{\Delta E_A^f\left(\overrightarrow{\varepsilon}\right)}{kT}\right) \tag{1.8}$$

where,

$$\Delta E_A^f\left(\overrightarrow{\varepsilon}\right) = -V_0 \Delta \overrightarrow{\varepsilon}_A \cdot C \cdot \overrightarrow{\varepsilon} - \Delta\mu_A\left(\overrightarrow{\varepsilon}\right) + qfE_{act}\left(\overrightarrow{\varepsilon}\right) \tag{1.9}$$

in which V_0 is the activation volume of an antimony atom, C is the lattice stiffness tensor of the host material, μ_A is the chemical potential of an impurity in a solubility-limiting cluster/precipitate, q is the charge state, f is the fraction of ionized dopants and E_{act} is the activation energy of a charge carrier in a dopant level [26]. The first term on the right-hand side of (1.9) accounts for the volumetric effects due to an isolated impurity. The second term accounts for the induced strain due to an individual atom in a large cluster and is generally considered to be negligible. The third term, for degenerately doped semiconductors, can also be disregarded, as when the dopant band merges with the conduction/valance band, $\Delta E_{act}\left(\overrightarrow{\varepsilon}\right)$, becomes negligible. As a result, the solubility enhancement factor given in (1.8) reduces to [26]

$$\frac{C^{ss}\left(\overrightarrow{\varepsilon}\right)}{C^{ss}\left(0\right)} = \exp\left(-\frac{\Delta E_A^f}{kT}\right) = \exp\left(\frac{V_0 \Delta \overrightarrow{\varepsilon} \cdot C \cdot \overrightarrow{\varepsilon}}{kT}\right) \tag{1.10}$$

In light of this, when calculating the solubility enhancements for different species, their activation volume becomes the pertinent property. Although arsenic is atomically larger than silicon, long range bond length reductions, mean that the incorporation of substitutional arsenic has little volumetric significance in the silicon lattice [52]. Antimony bond lengths in silicon do not show similar reductions relative to pure silicon. This means that antimony

activation is enhanced through localized stress relaxation effects accompanying the incorporation of the atomically larger dopant in the ε-Si lattice. Figure 1.22 demonstrates the activation enhancements of antimony and arsenic in silicon as a function of strain [26].

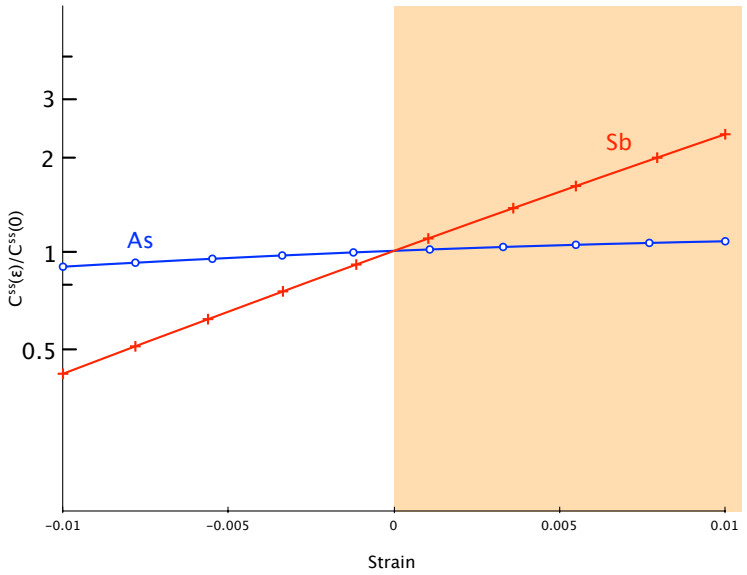

Figure 1.22: Activation trends for antimony and arsenic as a function of strain. Volumetric effects lead to increased activation of antimony in tensile strained silicon [26].

Dopant Diffusion

Inhomogeneous dopant distributions, such as those resulting from ion-implantation give rise to dopant redistribution through diffusion. As with activation, diffusion is a thermally driven process and occurs largely during annealing. General considerations of dopant diffusion within the silicon crystal, proceed in accordance with Fick's law,

$$J = -D \cdot \nabla C \tag{1.11}$$

where J is the dopant flux, D is the diffusion coefficient, C is the dopant concentration and the negative sign indicates that diffusion occurs in the direction of reducing concentra-

tion. While this approach allows analyses and predictions of dopant diffusion, it assumes a homogeneous host material. This simplification can be acceptable for dopants which dissolve interstitially e.g. oxygen, however for substitutional dopants, the crystalline nature of the material must be considered. Although a fully atomistic treatment of dopant diffusion is beyond the scope of this thesis, a cursory understanding of defect mediated diffusion is beneficial to interpretation of the relative diffusion rates in strained and unstrained silicon.

Transient Enhanced Diffusion

Transient enhanced diffusion (TED) is the process by which the point defects and dopants introduced during ion implantation diffuse as coupled pairs through the material. While antimony has been shown to diffuse predominantly through vacancy mediation [54], [55], [56], arsenic has shown fractional diffusivities attributable to self-interstitials of between ∼0.35 and ∼0.55 [57], [55], [58].

Central to the calculation of dopant diffusivity, therefore, is the consideration of the equilibrium density of appropriate mediators. The stress response of this density is characterized by the relaxation volume of the defect (the volume change in the vicinity of the defect upon formation). Parenthetically, a second stress response consideration is the ease with which the defects migrate through the host material, characterized by the migration volume (the additional volume change when the defect reaches the saddle point of migration), however this is accepted to be negligible [22]. Equation (1.12) gives the strain response of the defect density and figure 1.23 demonstrates the formation and migration of a vacancy defect,

$$\frac{C^{i,a}(\sigma)}{C^{i,a}(0)} = \exp\left(\frac{2\sigma_{biax}V^r}{3kT}\right) \tag{1.12}$$

where $\frac{C^{i,a}(\sigma)}{C^{i,a}(0)}$ is the stress response of the equilibrium defect density (a identifies the defect in question), σ_{biax} is the applied biaxial stress and V^r is the vacancy relaxation volume.

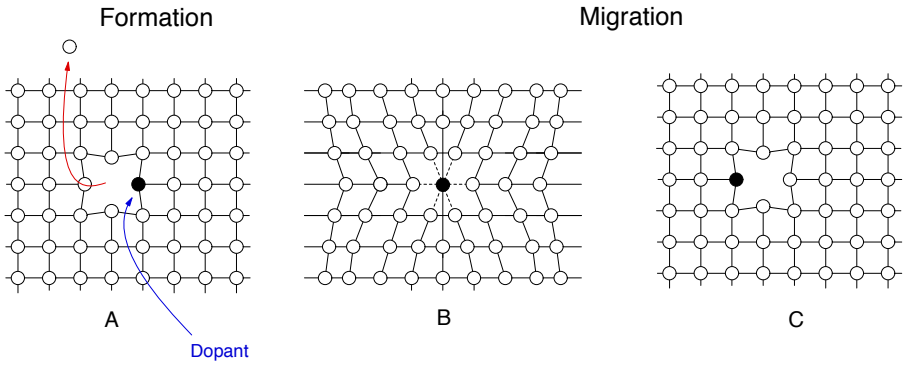

Figure 1.23: Schematic representation of vacancy formation and vacancy mediated dopant migration [22].

Due to antimony's almost purely vacancy mediated diffusion, and arsenic's reliance on self-interstitial mediation, any differences between the defect relaxation volumes will be reflected in the species' diffusivities. Using the conventional stress notation i.e. tensile stress being positive, it follows from (1.12) that the equilibrium density of vacancies is expected to reduce in the presence of tensile stress due to their negative formation volume [59]. The resulting suppression of antimony diffusion in ε-Si is well documented [21], [60] while arsenic diffusivities have been shown to increase in the presence of both compressive and tensile stress (although more so in the case of compressive stress) due to the dual contributions of vacancies and self-interstitials [61].

1.4 Sample Description

Sample Structure

The samples discussed in this thesis are Czochralshi grown (001) p-type silicon. They were sourced from IQE Silicon Ltd. and AdvanceSis Ltd. The ε-Si layers of the IQE samples were grown to a thickness of 17.5 nm, atop linearly graded $Si_{0.83}Ge_{0.17}$ virtual substrates. The AdvanceSis samples were grown in accordance with terrace graded technology. The atomic percentage of Ge in the AdvanceSis virtual substrates range from 10% to 30%, with ε-Si capping layer thicknesses of between 9 nm and 42 nm. Table 1.2 provides a breakdown of the percentage Ge in the substrates, the corresponding ε-Si capping layer thicknesses, the sample source and the calculated theoretical critical thicknesses according to Maree [34]. Figure 1.24 depicts a cross-section of the samples investigated.

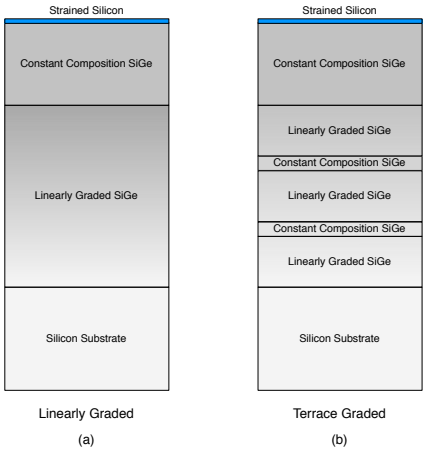

Figure 1.24: Schematic of sample cross-section : (a) linearly and (b) terrace graded virtual substrate samples. Each sample has a constant compositional $Si_{1-x}Ge_x$ layer where x lies between 0.1 and 0.3. This layer is capped with a ε-Si layer with thickness of between 9 nm and 42 nm.

Nominal VS Ge Content (at%)	Source	Theoretical Critical Thickness (nm)	ε-Si Layer Thickness 1 (nm)	ε-Si Layer Thickness 2 (nm)	ε-Si Layer Thickness 3 (nm)
10	AdvanceSiS	103.32	20	NA	NA
15	AdvanceSiS	46.10	17.5	NA	NA
17	IQE	35.95	17.5	NA	NA
20	AdvanceSiS	26.04	15	24	42
23	AdvanceSiS	19.73	12	15	NA
26	AdvanceSiS	15.48	8	15	NA
30	AdvanceSiS	11.66	9	12	15

Table 1.2: Breakdown of samples indicating theoretical critical thickness, grown ε-Si cap layer thickness and source.

Sample Processing

In order to investigate the propriety of the material combination in question for the production of ultra shallow abrupt junctions the above described structures were subjected to ultra low energy (ULE) ion implantation and rapid thermal anneal (RTA) processes. These surface modifications allow the production of the required features.

Ion Implantation

In order to generate the ultra shallow junctions required by the ITRS [28], 2 keV Sb ion implantation was employed. This low implant energy limits the penetration depth of the

dopants to roughly the top 9 nm of the sample. Further, in order to compensate for the small cross-sectional areas of source/drain extensions their conductivity must be maximized. To this end, degenerate doping is required. In the current work, implant doses of between of $1 \times 10^{14} cm^{-2}$ and $1 \times 10^{15} cm^{-2}$ were used.

Figure 1.25 shows the results of penetration depth simulations carried out using SRIM 2011 (Stopping and Range of Ions in Matter) calculations [62]. The simulations were carried out on the basis of a 2 keV antimony implant into silicon. Figure 1.25 also plots the damage profile arising within the same simulations. It should be noted that since the y-axes of these profiles are in units of $A^{-1} Ion^{-1}$, they take no account of implant dose and so further calculations are necessary to determine actual damage levels.

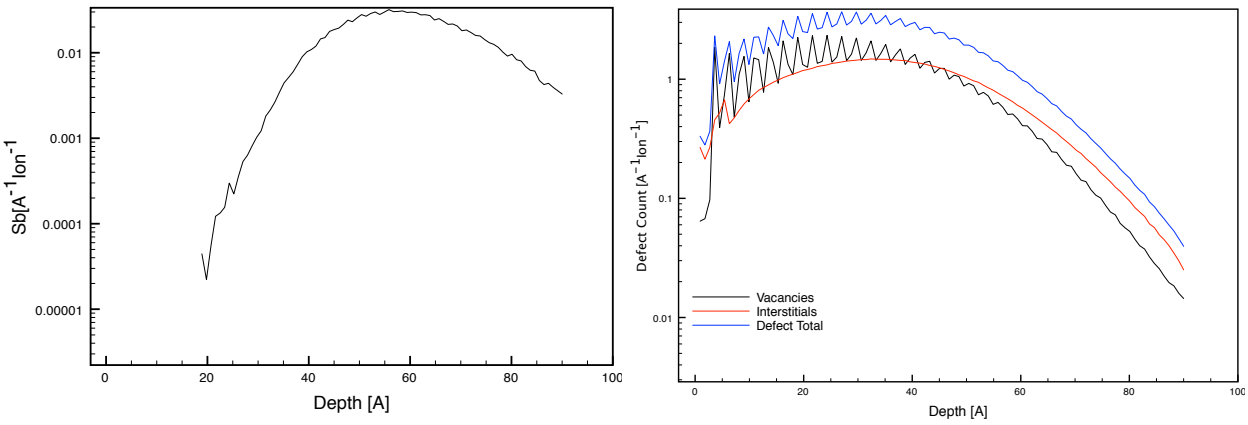

(a) Antimony Ions

(b) Defects

Figure 1.25: SRIM calculated profiles of (a) dopant distribution and (b) radiation damage distribution, resulting from a 2 keV Sb implantation in silicon.

Annealing

The controlled application of thermal energy to an ion-implanted sample allows the structure to return to the more stable crystalline form and can maximize activation of dopants. The

method of application depends on the specific goals of the process and the restrictions on the thermal budget. The current work requires above equilibrium dopant solubilities, and three annealing processes have demonstrated this characteristic, namely flash annealing, laser annealing and rapid thermal annealing which gives rise to solid phase epitaxial regrowth (SPER). Of the three, RTA induced SPER has demonstrated the highest dopant solubility levels [63] as shown in figure 1.26.

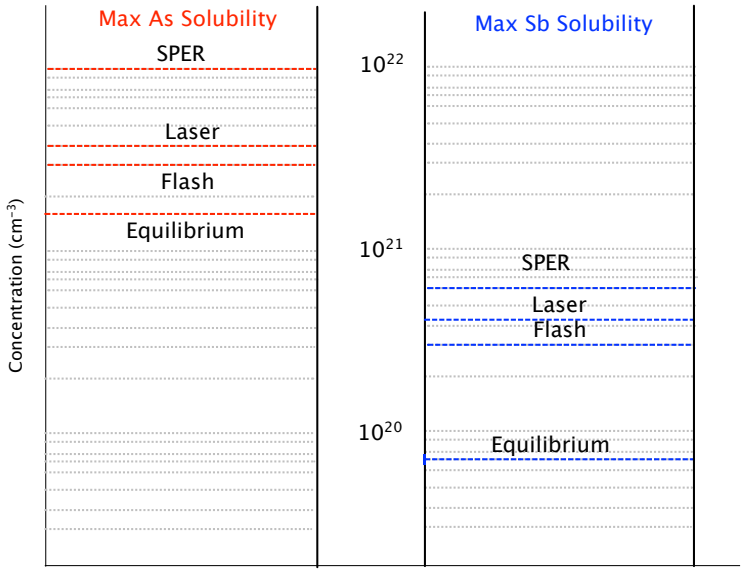

Figure 1.26: Solid solubility levels achievable for As and Sb dopant in bulk Si using laser, flash and SPER annealing techniques [63].

SPER

In samples which retain a crystalline seed, it is possible to regrow the radiation damaged region in registry with this. In the resulting process (SPER), the amorphous/crystalline interface moves towards the sample surface, leaving crystalline material in its wake. It has been shown that for covalently bonded solids in the $\langle 100 \rangle$ and $\langle 110 \rangle$ orientations, amorphous layers can be regrown into nominally defect free structures at temperatures of $\geq 500°C$ [64] with regrowth rates dependent on anneal temperature. Parenthetically however, for $\langle 111 \rangle$

silicon this has been shown not to be the case [65]

SPER is an Arrhenius process with an activation energy less than that of dopant diffusion. This allows dopants to be "frozen" in place under correctly chosen annealing conditions. The resulting preservation of the dopant profile allows peak activation levels comparable to peak dopant concentrations, well above the equilibrium solid solubility of the material [64]. These high activation levels are meta-stable however, as the equilibrium levels are restored if annealing duration or temperature is sufficiently long or high, respectively.

In the present work, 10 second rapid thermal anneals (RTA) at temperatures of $600°C$, $700°C$, $800°C$ were used, as this annealing method has been shown to initiate solid phase epitaxial regrowth (SPER) with increased activation [64].

Chapter 2

Activation and Diffusion Studies

Although the major thrust of this thesis is not in the electrical characterisation of the samples, an investigation of ε-Si would be incomplete without consideration of the impacts of strain on the material's electrical properties, and the diffusion of implanted species. The measurements reported in this chapter were carried out by partners on this project, and as such the presented analysis is far from exhaustive. The electrical data pertaining to this project has been extensively published [66], [67], [26], [68] and [69] and examples of the diffusion data can be found in references [66] and [69]. The electrical and diffusion data are presented at such an early stage in the document as they provide experimental support for the introductory assertions with regard to ε-Si antimony activation and diffusion, in addition to providing guidance and context for the investigations to follow.

In this project, the electrical characterisation was carried out using a combination of Van der Pauw (sheet resistance) and differential Hall (carrier density) measurements. These were carried out in the Advanced Technology Institute within the University of Surrey. The dopant profile characterisation was carried out using secondary ion mass spectroscopy (SIMS), also in conjunction with the University of Surrey.

2.1 Van der Pauw Measurements

Traditional global resistivity characterisation is carried out by four point probe (4PP) measurements, however this technique provides no means of decoupling the effects of mobility enhancements and carrier density increases. Van der Pauw sheet resistance measurements were used as they avoid the penetration issues associated with the 4PP technique. In a 4PP measurement, the efficacy of the probe contacts is assured by weighting the probe arm. This results in penetration of the probe tips into the sample. As a result of the ultra-shallow nature of the implant profiles being investigated, this penetration can result in large errors in the measured sheet resistances. Van der Pauw measurements proceed through deposited ohmic contacts rather than weighted mechanical contacts, thus avoiding these errors [70]. In addition to this when used in conjunction with Differential Hall measurements, they can decouple the mobility and carrier density effects.

Principles of Application

Van der Pauw measurements in general require small ohmic edge contacts and a homogeneously thick sample free of discontinuities. The measurements reported herein were carried out in a clover leaf geometry shown in figure 2.1. This geometry somewhat simplifies the application of the contacts as the central region is under test and the leaves constitute edge contacts.

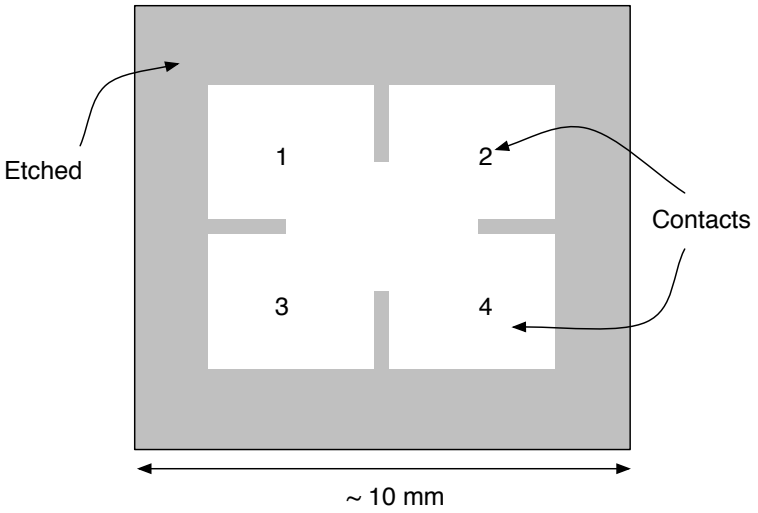

Figure 2.1: Cloverleaf pattern used to fulfill the criteria of Van der Pauw measurements.

Referring to figure 2.1 , a current is applied between contacts 3 and 4 (I_{34}) and the associated voltage is measured across contacts 2 and 1 (V_{21}). The resulting resistance ($R_{34,21}$) is then calculated using the equation [71],

$$R_{34,21} = \frac{V_{21}}{I_{34}} \tag{2.1}$$

$R_{42,13}$ is calculated in a similar manner

$$R_{42,13} = \frac{V_{13}}{I_{42}} \tag{2.2}$$

Van der Pauw developed an expression relating these terms to the sheet resistance,

$$R_s = \exp\left(-\frac{\pi}{R_s}R_{34,21}\right) + \exp\left(-\frac{\pi}{R_s}R_{42,13}\right) \tag{2.3}$$

If the sample geometry provides a line of symmetry between points 2 and 3 (as is the case in the cloverleaf structure), $R_{34,21}$ and $R_{42,13}$ will be equal and the sheet resistance becomes

$$R_s = \frac{\pi}{\ln 2}R_{34,12} \tag{2.4}$$

2.2 Differential Hall Technique

Differential Hall measurements were used to characterize the carrier densities, and, in conjunction with the aforementioned Van der Pauw measurements, the carrier mobility within the ε-Si samples. The differential Hall technique provides a means of depth profiling the carrier density within a sample through a sequence of Hall measurements and etch processes. These measurements were carried out on the same cloverleaf samples as the Van der Pauw measurements. Hall measurements are based on the Hall effect.

The Hall Effect

In a sample, the application of a magnetic field perpendicular to a flowing current results in the production of a small voltage perpendicular to both the current and the magnetic field. Measurement of this transverse voltage, known as the Hall voltage (V_H) allows calculation of the nominal majority carrier density. The Hall voltage is generated as follows.

Any charge carrier moving at a drift velocity, ν_d, will be acted upon by the Lorentz force, F, which is given by,

$$\mathbf{F} = q\left(\nu_d \times \mathbf{B}\right) \tag{2.5}$$

where q is the elementary charge and $\mathbf{B}$ is the magnetic field. The dependence of the Lorentz force on q, results in the separation of electrons and holes. This separation results in a voltage which opposes the Lorentz force, known as the Hall voltage. The system thus generates an equilibrium potential difference at which the Lorentz force is precisely counter-balanced, by the Hall voltage. The cross product of (2.5) orients the Hall voltage perpendicular to both the current and magnetic field, figure 2.2 depicts this process.

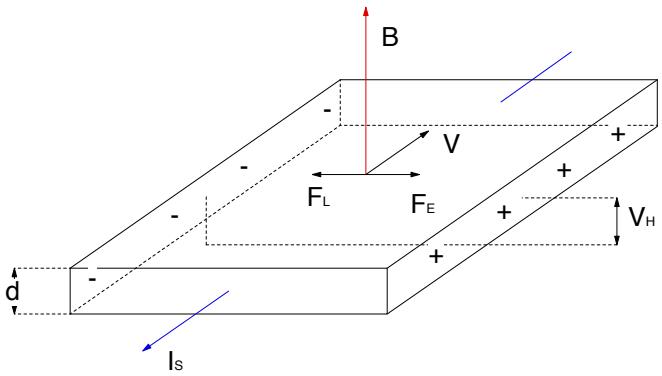

Figure 2.2: Generation of the Hall voltage. **V** and **B** are the applied voltage and magnetic fields respectively; I_s is the current flow; $\mathbf{F}_L$ and $\mathbf{F}_E$ and the Lorentz force and electric force resulting from the subsequent separation of charges and $\mathbf{V}_H$ is the Hall voltage.

Measurement of the Hall voltage (V_H) allows calculation of the Hall coefficient

$$R_H = \frac{V_H}{\mathbf{IB}} \tag{2.6}$$

and thus the net carrier density through the relation

$$N = \frac{r}{eR_H} \tag{2.7}$$

where r is the Hall scattering factor, a term related to the fraction of dopants which are active; for the current samples, this term has been determined to be unity [70].

Given the sheet resistance, R_s (as calculated by the Van der Pauw method outlined previously) the Hall coefficient can additionally be used to determine the Hall mobility [25],

$$\mu_H = \frac{R_H}{Rs} \tag{2.8}$$

In general the distinction should be noted between the Hall mobility and the conventional

mobility of carriers. As these terms are related through the Hall scattering factor ($\mu_c = \frac{\mu_H}{r}$) and this is currently considered to be unity, the distinction is currently not necessary.

Differential Hall Measurements

By carrying out a series of Hall measurements interleaved by the sequential removal of a small thickness of the sample, a depth profile of the carrier density can be attained. This process constitutes a differential Hall measurement. By taking a Van der Pauw measurement concurrently with each Hall measurement, a depth profile of the carrier mobility can additionally be calculated.

The Hall coefficient of the removed layer at each step is given by

$$R_H\sigma^2 = \frac{\delta\left(R_H\sigma_s^2\right)}{\delta x} \tag{2.9}$$

where σ is the conductivity of removed layer ($\sigma = Rs^{-1} = \frac{\delta\sigma_s}{\delta x}$; σ_s is the measured conductivity) and x is the sample depth. The Hall mobility of the removed layer is thus given by

$$\mu_H = \frac{R_H}{R_s} = R_H\sigma = \frac{\delta\left(R_H\sigma_s^2\right)}{\delta\sigma_s} \tag{2.10}$$

As $\sigma = e\mu_H N$, the carrier density within the layer is given by

$$N = \frac{\sigma}{e\mu_H} = \frac{\left(\delta\sigma_s\right)^2}{e\delta x \cdot \delta\left(R_H\sigma_s^2\right)} \tag{2.11}$$

Both the Van der Pauw and Hall measurements were carried out on an Accent HL5900 Hall system. For both measurement types all permutations of contact pair combinations and current polarities were measured, an average of eight measurements was taken as the final result [25].

The removal of material layers was achieved by the growth and removal of native oxide layers. Room temperature reactions between silicon and oxygen forms a thin layer of native oxide $\sim$ 1-2 nm. The consumption of silicon during this reaction means removal of this oxide constitutes the removal of a similar depth of silicon. The oxide was selectively removed by a HF acid dip, this was followed by a water dip which removed any excess HF acid and also aided in the regrowth of the oxide layer.

The measurement process was automated with operator defined etch and oxidation times. The layer thicknesses were determined by measuring the final crater depth and the etch rate was assumed to be constant throughout.

2.3 Secondary Ion Mass Spectrometry

Secondary Ion Mass Spectrometry (SIMS) is a popular technique for determining the distribution of impurity atoms and molecules within a matrix. During a SIMS analysis the sample is slowly sputtered away by a primary ion beam and the subsequent collision cascade results in the emission of secondary particles. The vast majority of these particles are neutrally charged, however a small fraction ($\sim$5%) leave the surface as ions, allowing ion counting via mass spectrometry. The process is depicted in figure 2.3.

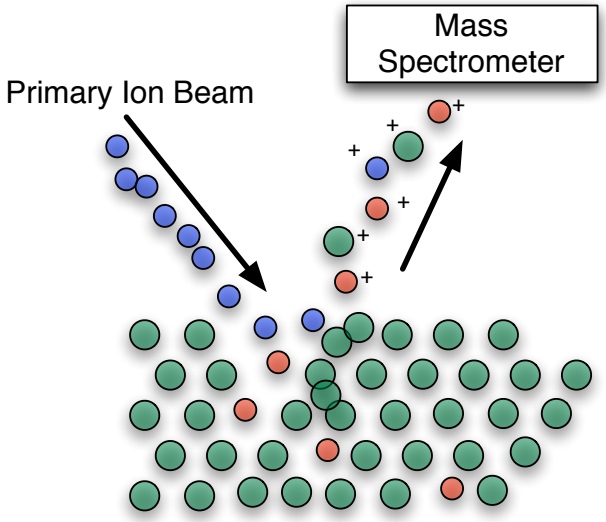

Figure 2.3: Process of Secondary Ion Mass Spectroscopy.

As SIMS relies on secondary ions for analysis, the ionization efficiency (ion yield) for a given system must be maximized. The ion yields are strong functions of the atomic ionization potential for positive ions and electron affinity for negative ions. These dependencies are not definitive however, as the ion yield depends on both the species of interest and the matrix.

An additional parameter in determining the ionization efficiency is the choice of primary ion. For oxygen bombardment, positive ion yield is increased. This is due to oxygen's high electron affinity (which favors electron capture) and high ionization energy (which prohibits positive charging) which result in the transfer of electrons to the oxygen ions rendering the target positively charged. Negative ion enhancement is achieved through cesium bombardment as a result of work function reduction and the concomitant additional electron concentrations.

The ion counts of a SIMS analysis can be converted to quantitative concentration data via

the use of tabulated relative sensitivity factors (RSF) through the equation [72],

$$C_E = RSF_E \frac{I_E C_M}{I_M} \tag{2.12}$$

where the M and E subscripts differentiate between the host matrix and element, and I and C values are the secondary ion intensities and concentrations respectively. If the matrix concentration is assumed to be constant (valid for trace element analysis) it can be combined with the elemental RSF to provide the more convenient [72],

$$C_E = RSF \frac{I_E}{I_M} \tag{2.13}$$

where $RSF = C_M RSF_E$.

Finally, depth profiles are extracted by calculating the average sputtering rate through profilometry of the final indent. The assumption of constant sputtering rate is a limitation of SIMS.

The data presented herein was measured commercially by CSMA-MATS under the instruction of project partners in Surrey University. The profiles result from a 500 eV cesium beam with a sputter-limited resolution of 2nm/decade. The beam scan area was $300 \times 300 \mu m$ but only the central $66 \times 66 \mu m$ area was analyzed in order to avoid crater wall sputtering contamination. During measurements, the samples were rotated at 20 rpm to minimize crater roughness and improve depth calibration.

2.4 Results & Discussion

The electrical measurements were carried out on the $Si_{0.83}Ge_{0.17}$ samples with a nominal strain of 0.7% in the top 17.5 nm ε-Si layer. These were implanted with antimony doses ranging from $1 \times 10^{14} cm^{-2}$ to $1 \times 10^{15} cm^{-2}$ and arsenic doses of $4 \times 10^{14} cm^{-2}$ and $1 \times 1^{15} cm^{-2}$.

All implants were carried out at an energy of 2 keV and were subjected to 10 s anneals in N_2 at 600°C, 700°C and 800°C. Figure 2.4 compares the sheet carrier densities of $4 \times 10^{14} cm^{-2}$ antimony and arsenic implants as a function of anneal temperature in both strained and bulk silicon.

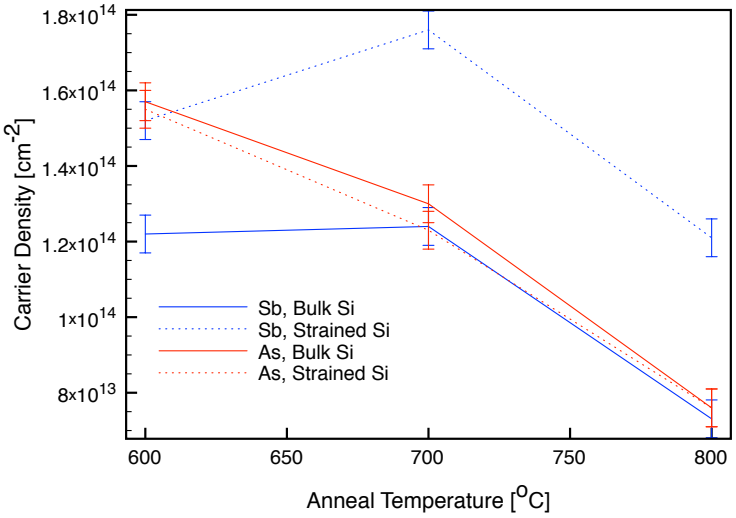

Figure 2.4: Carrier density as a function of anneal temperature for 4×10^{14} cm^{-2} antimony and arsenic implants in bulk silicon and ε-Si samples having a $Si_{0.83}Ge_{0.17}$ virtual substrate.

Using the carrier densities as indicators of activation levels, figure 2.4 demonstrates the antimony and arsenic activation trends within bulk and strained silicon. The inter-species trends are consistent with the volumetric arguments of Ahn *et al.* [26] presented in chapter 1.1.

Arsenic demonstrates negligible activation differences between the strained silicon and bulk silicon. Antimony on the other hand demonstrates large increases in activation upon application of strain, consistent with the energetic favorability of large atom inclusion within the tensile strained lattice [26].

The trends with respect to anneal temperature are also interesting. For arsenic, the max-

imum activation is reached upon the 600°C anneal and subsequent to this, we see arsenic deactivation, most likely due to clustering effects. Very little difference is observed between the thermal trends of arsenic in bulk and strained silicon.

For antimony, the 700°C anneal has little additional impact on the bulk activation, however a dramatic increase in activation is observed within the strained material. Subsequent to the 800°C anneal, the onset of deactivation is observed for both the bulk and strained material. Lai *et al.* has attributed the discrepancy between the trends for the two host material types to an increase in the cluster formation energy in ε-Si, as demonstrated in figure 2.5 [67].

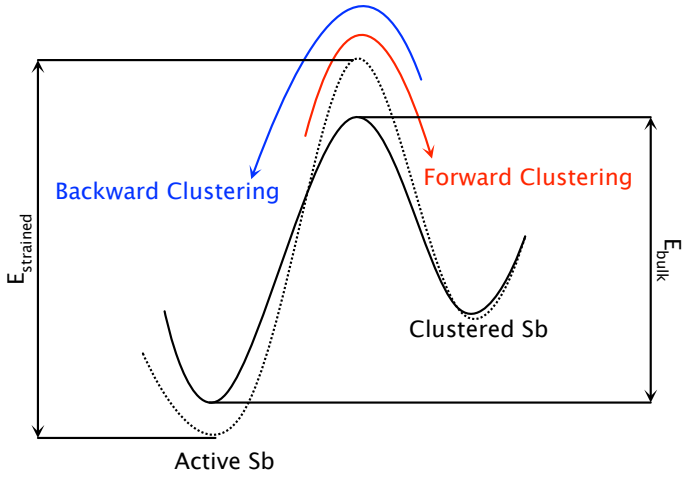

Figure 2.5: Barrier height difference for Sb clustering in bulk and tensile strained silicon. The energetic favourability of Sb activation in ε-Si results in more stable active Sb and an increased potential barrier to cluster activation [67].

Figure 2.4 identifies that within ε-Si, antimony activation is enhanced with respect to that of arsenic, it also appears that an optimum anneal temperature exists for these implants in the region of 700°C. The crucial processing parameter of implant dose however remains to be considered. As the trends of figure 2.4 are indicative of all implant doses investigated,

the considerations of implant dose concentrate on the 700°C annealed samples. Figure 2.6 thus plots the carrier densities of the 700°C annealed samples as a function of implantation dose.

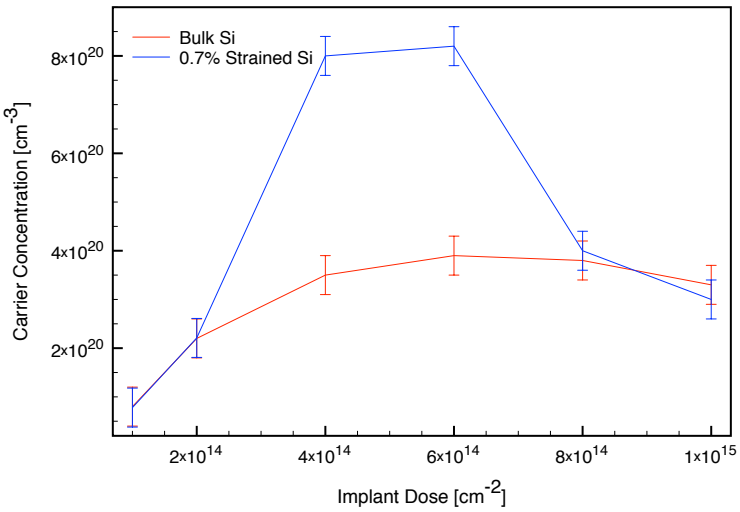

Figure 2.6: Carrier concentration as a function of implant dose for ε-Si samples having a $Si_{0.83}Ge_{0.17}$ virtual substrate. All samples were annealed for 10 seconds at 700°C

Figure 2.6 reveals optimal activation in the mid dose region with the 6×10^{14} cm^{-2} antimony implant demonstrating the highest carrier density levels. Bennett *et al.* attributes the fall-off in activation at higher implant doses to the formation of antimony clusters or precipitates [24]. Although these samples demonstrate diminished carrier mobility in the same mid-dose range (resulting from increased ionized dopant scattering) the net result is a reduction in the sheet resistance [25], as shown in figure 2.7.

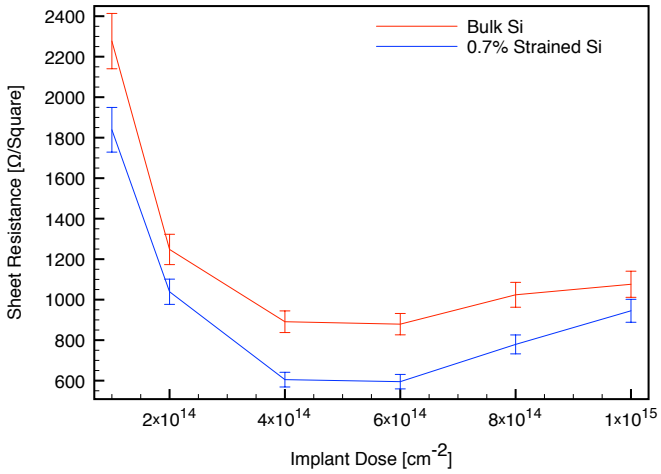

Figure 2.7: Sheet resistance as a function of implant dose for ε-Si samples having a $Si_{0.83}Ge_{0.17}$ virtual substrate. All samples were annealed for 10 seconds at 700°C

The diffusion assertions of chapter 1.1 were borne out by SIMS measurements. Figure 2.8 shows the dopant profiles resulting from 2 keV, 4×10^{14} cm^{-2} arsenic and antimony implants in 0.7% strain ε-Si. The figure demonstrates the retardation of antimony penetration with respect to arsenic due to its increased atomic size.

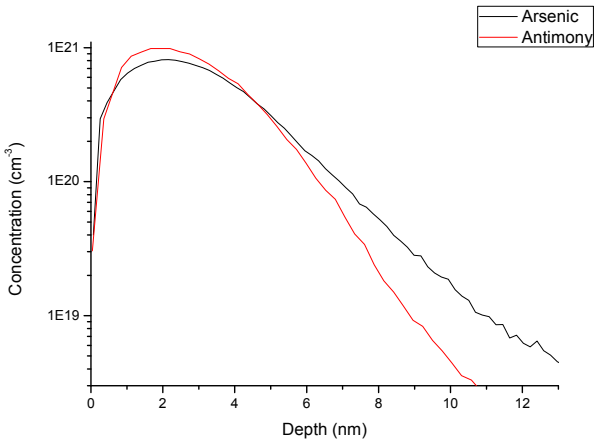

Figure 2.8: SIMS measured as-implanted dopant profiles for antimony and arsenic (2 keV, 6×10^{14} cm^{-2}), data taken from [65].

Figure 2.8 shows antimony's shallower junction depth of 10 nm as opposed to arsenic's 13 nm (defined at a concentration of $5 \times 10^{18}\ cm^{-3}$) and improved abruptness, with a tail demonstrating a descent of 2 nm/decade compared to arsenic's 3 nm/decade.

Antimony's superiority as an implant capable of producing ultra shallow abrupt junctions is underscored when its post-anneal profiles are considered. Figure 2.9 compares the as-implant and post anneal (800°C) profiles of the 2 keV, $4 \times 10^{14}\ cm^{-2}$ antimony implant in 0.7% strain ε-Si.

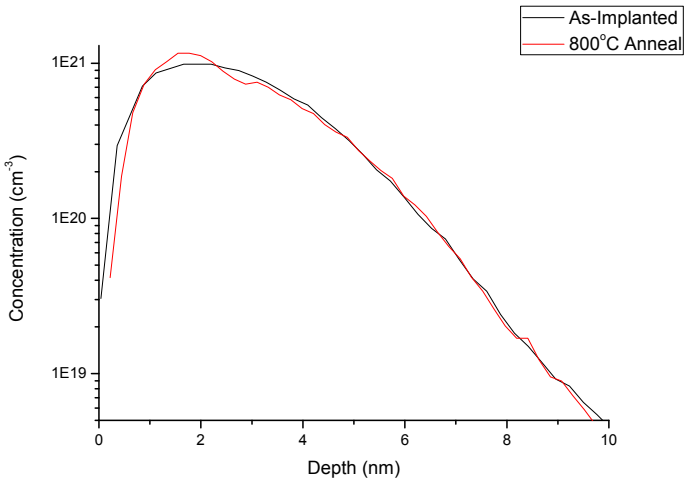

Figure 2.9: SIMS measured dopant distribution for Sb implants pre and post anneal. Data taken from [65].

Figure 2.9 demonstrates little deviation from the as-implant profile, resulting from the suppression of vacancy production in ε-Si and concomitantly the suppression of antimony's vacancy mediated diffusion.

It should be noted that the absolute peak depths of figures 2.8 and 2.9 are not in agreement with the SRIM simulations previously presented. Discussions with the authors of ref [65] revealed the possibility of systematic errors in the recording of the data, however, the relative

trends are in agreement with data obtained subsequently.

2.5 Conclusions

The data presented here demonstrates the advantages of antimony as a dopant over arsenic in εSi. It shows the increased activation of antimony with respect to arsenic but also reveals the sensitivity of the activation levels to the anneal temperature and implant dose. These dependences raise the question of strain level consistency within these samples, as strain relaxation is a possible precursor to antimony deactivation. Subsequent chapters aim to investigate this possibility.

Chapter 3

High Resolution X-Ray Diffraction

Within this project, large emphasis is placed on the strain levels within the active ε-Si layer and their response to surface modification through ion-implantation and annealing processes. In order to monitor these strain levels high resolution x-ray diffraction (HR-XRD) is used. The titular "high resolution" refers to the $\sim$5 arcsec angular resolution provided by the particular experimental configuration used. This angular resolution allows the separation of strain, composition and tilt effects through the recording of reciprocal space maps (RSMs).

3.1 Historical Background

X-Ray Diffraction (XRD) was introduced as an analytical tool in 1911 by von Laue, Friedrich and Knipping's work on rock salt [73]. A theoretical framework was proposed the following year by W.L.Bragg [74] in his Nobel prize winning paper. XRD can be broadly broken down into two general processes: powder diffraction and single crystal diffraction. In the current context we concentrate on single crystal diffraction which is a non-destructive means of investigating the crystalline properties of a sample. Due to its sensitivity to inter-planar

spacing in the crystal lattice, XRD presents a means of determining a range of material characteristics investigable through measurement of this property, including sample crystallinity and strain.

3.2 Introduction & Bragg's Law

Light scattering results in diffraction, as opposed to common reflection, when the spacing between scattering centers is greater than the radiation wavelength [75]. Under this condition, superposition of scattered wavefields results in the production of interference patterns with angular dependent intensity distributions.

For crystalline diffraction, the concept of lattice planes within the crystal is crucial. Within these planes, the concatenation of spherical waves, within a very short distance, reduces to a plane wave, with wavefronts parallel to, and a propagation vectors perpendicular to, the originating planes. The consideration of lattice plane scattering thus allows a great simplification of crystalline diffraction processes. In his theoretical framework, Bragg made use of this structural simplification and considered each set of lattice planes in isolation. This lead to Bragg's Law which relates the diffraction peak angle to the pathlength difference between beams scattered from successive lattice planes within a set,

$$n\lambda = 2d_{hkl}\sin\theta_B \tag{3.1}$$

where λ is the wavelength of light, d_{hkl} is the inter-planar spacing and θ is the Bragg angle. Figure 3.1 depicts the principle schematically.

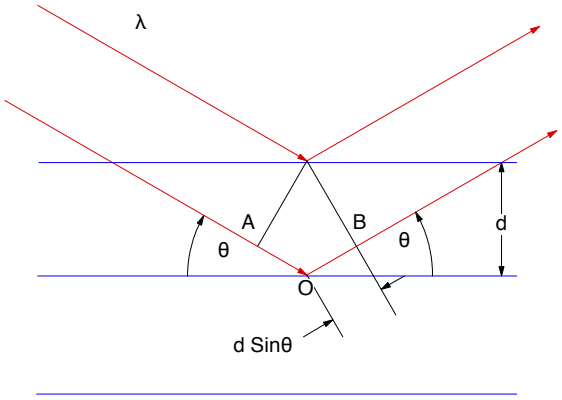

Figure 3.1: Schematic representation of Bragg's law. Large diffraction signals are recorded at angles which result in the pathlength difference AOB being an integer number of wavelengths, allowing constructive interference to ensue.

Bragg's law provides a simple and intuitive means of relating experimentally observed angular peak positions with the average spacing between lattice planes of interest. For three-dimensional applications however, and calculations of diffracted intensities, more elegant and powerful treatments are required. These treatments come in the form the kinematical and dynamical theories of diffraction. These theories can be shown to have the same underlying principles and differ only in their levels of approximation. As such, the more complete dynamical theory builds upon fundamentals laid out by the simpler and more intuitive kinematical theory.

3.3 X-Ray Diffraction

The applicability of a given theory (kinematical or dynamical) lies in the emphasis given to scattered wave interaction. For thin samples (where $\mu_0 t < 1$, μ_0 and t are the optical absorption coefficient and thickness of the sample respectively) or weakly scattering materials,

the diffracted intensity can be considered insignificant with respect to the incident intensity. These criteria can be approximated by considering the sample as an amalgamation of misoriented regions, thus allowing incoherent scattering and minimal diffracted wave interference. This is kinematical diffraction and the total diffracted intensity is the summation of that from individual scatters. This theory's strength lies in its simplicity and intuitive geometrical origins, however it founders in the regard of diffracted intensity predictions in all but a few situations.

Diffraction from strongly scattering materials (of which single crystals are an example) or from thick samples, results in diffracted waves of significant intensity, whose interaction should not be ignored. Dynamical theory incorporates these interactions by considering solutions to Maxwell's equations for all waves within the crystal (consistent with the crystal periodicity and continuity of electric field across the crystal/vacuum interface). Dynamical theory thus identifies sensibly co-existing waves [75] and also allows consideration of multiply scattered beams, loss of incident intensity and interference effects. Although technically more correct, the additional information provided by the dynamical treatment, which for the most part deals with diffracted intensities, is largely redundant in the current data interpretations. As such, the current considerations are confined to the kinematical theory of diffraction. An account of both the dynamical theory of diffraction can be found in appendix A.

3.4 Kinematical Theory of X-Ray Diffraction

Kinematical theory describes the crystal under test as an amalgamation of smaller crystallites (ideally imperfect) and assumes that the diffracted intensity from each of these crystallites simply add together, i.e. regions are incoherent [76]. The result of this incoherence is that the intensity of the scattered light, when added with consideration to phase, is small with respect to the incident light. This allows both the loss of incident intensity and the interference

between the incident and scattered light to be neglected. In addition to this, kinematical theory considers only a single scattering event per photon.

The result of these approximations, is that the theory's ability to accurately predict diffracted intensities is severely limited, the theory does however predict reasonably accurate diffraction angles and allows the expansion of Bragg's Law to 3-dimensions. The major revelation of the kinematical theory is the concept of the reciprocal lattice, which reveals the intimate relationship between the lattice periodicity and the angles of peak diffraction.

Reciprocal Lattice

Light scattering results from the formation of an oscillating dipole moment between the nucleus and electrons of an atom (this concept is dealt with in more detail in chapter 5), initiated by an oscillating electromagnetic (EM) excitation. Of importance in the current context, is how these scattered waves add with regard to phase, and how this gives rise to angular dependent intensity distributions.

The 3-dimensional periodicity of a crystal lattice allows a concise description in terms of three translational vectors **a**, **b** and **c**, whose enclosed volume defines the unit cell, figure 3.2 demonstrates this. Within this construct, the lattice points are defined by the vectors,

$$\mathbf{r} = u\mathbf{a} + v\mathbf{b} + w\mathbf{c} \tag{3.2}$$

where u, v and w are integers. Planes of lattice points can easily be envisioned within this construct (demonstrated in figure 3.2). These planes are of immense importance to crystallographic diffraction considerations and the reciprocal lattice is concerned with their frequency.

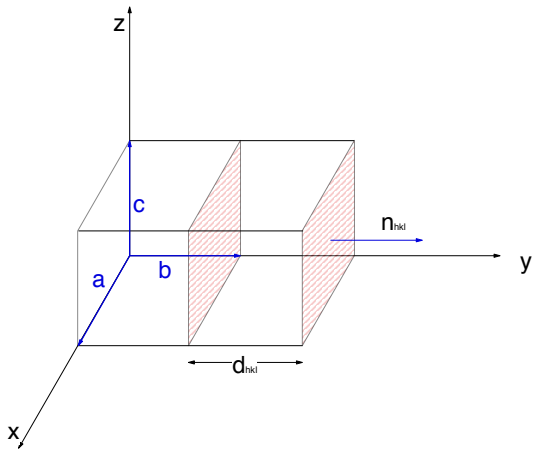

Figure 3.2: Real space lattice indicating the unit cell (defined by vectors **a**, **b** and **c**), inter-planar spacing for the (010) lattice planes and the lattice plane normal of same.

Crystalline planes (hkl) are characterised by their normal vector, $\hat{\mathbf{n}}_{hkl}$ and their inter-planar spacing d_{hkl}. These two properties are sufficient to assign each set of lattice planes a point in reciprocal space, defined by the vector $\mathbf{G}_{hkl}$, extending from the reciprocal space origin (arbitrary for an infinite crystal such as that currently considered) to the reciprocal-lattice point [77],

$$\mathbf{G}_{hkl} = \frac{2\pi\hat{\mathbf{n}}_{hkl}}{d_{hkl}} \tag{3.3}$$

This vector is parallel to the real space [hkl] direction but has a magnitude of $2\pi/d_{hkl}$ i.e. reciprocal distance. The reciprocal lattice comprises of the points laid out by the $\mathbf{G}_{hkl}$ vectors for all lattice plane sets, figure 3.3 demonstrates the production of a 2-dimensional section of the silicon reciprocal lattice.

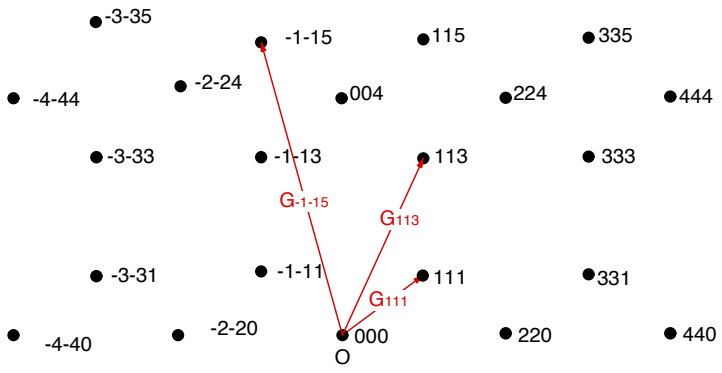

Figure 3.3: 2-dimensional section of Si reciprocal lattice. Reciprocal lattice points are defined by the extremities of the $\mathbf{G}_{hkl}$ vectors [78].

Similarly to the real space lattice, the reciprocal lattice is defined using translational vectors, namely $\mathbf{a}^*$, $\mathbf{b}^*$ and $\mathbf{c}^*$ which are defined as [77],

$$\mathbf{a*} \equiv \frac{2\pi \mathbf{b} \times \mathbf{c}}{\mathbf{a} \cdot (\mathbf{b} \times \mathbf{c})}; \mathbf{b*} \equiv \frac{2\pi \mathbf{c} \times \mathbf{a}}{\mathbf{a} \cdot (\mathbf{b} \times \mathbf{c})}; \mathbf{c*} \equiv \frac{2\pi \mathbf{a} \times \mathbf{b}}{\mathbf{a} \cdot (\mathbf{b} \times \mathbf{c})} \tag{3.4}$$

and conform to the following dot product relations with the direct lattice translational vectors,

$$\begin{aligned} &\mathbf{a*} \cdot \mathbf{a} = \mathbf{b*} \cdot \mathbf{b} = \mathbf{c*} \cdot \mathbf{c} = 2\pi \\ &\mathbf{a*} \cdot \mathbf{b} = \mathbf{a*} \cdot \mathbf{c} = \mathbf{b*} \cdot \mathbf{c} = \mathbf{b*} \cdot \mathbf{a} = \mathbf{c*} \cdot \mathbf{b} = 0 \end{aligned} \tag{3.5}$$

Now defining $\mathbf{G}_{hkl}$ in terms of these reciprocal lattice base vectors gives,

$$\mathbf{G}_{hkl} = h\mathbf{a*} + k\mathbf{b*} + l\mathbf{c*} \tag{3.6}$$

Diffraction

If one considers an sinusoidally oscillating incident wave travelling through the crystal with wave-vector $\mathbf{k}_i$, the oscillation of a dipole at the origin O is proportional to,

$$e^{-j\omega t} \tag{3.7}$$

A dipole situated at a point A defined by the vector $\mathbf{r}$ is thus proportional to [78],

$$e^{-j\omega t}e^{2\pi j\mathbf{k}_i\cdot\mathbf{r}} \tag{3.8}$$

The dipole oscillation described by (3.8) is not unique, the form of (3.8) can be replicated by the substitution of $(\mathbf{k}_i + \mathbf{G}_{hkl})$ for $\mathbf{k}_i$ as,

$$(\mathbf{k}_i + \mathbf{G}_{hkl})\cdot\mathbf{r} = \mathbf{k}_i\cdot\mathbf{r} + \mathbf{G}_{hkl}\cdot\mathbf{r} \tag{3.9}$$

and the scalar product of a direct lattice vector with any corresponding reciprocal lattice vector always results in an integer [75]. As the exponential of $2\pi j$ times an integer is unity, the expressions are equivalant, i.e. [78],

$$e^{2\pi j\mathbf{k}_i\cdot\mathbf{r}} = e^{2\pi j(\mathbf{k}_i+\mathbf{G}_{hkl}\cdot\mathbf{r})} \tag{3.10}$$

This allows conservation of energy and wave-vector for scattering events in which,

$$\Delta\mathbf{k} = \mathbf{k}_s - \mathbf{k}_i = \mathbf{G}_{hkl} \tag{3.11}$$

where $\mathbf{k}_s$ is the scattered wavevector. The implications of (3.11) on diffraction angles are best demonstrated graphically through the construction of the Ewald sphere.

Ewald Sphere

The constraints imposed by wavevector conservation and elastic scattering result in incident and scattered wavevectors of equal magnitude, i.e.,

$$|\mathbf{k}_i| = \frac{2\pi}{\lambda} = |\mathbf{k}_s| \tag{3.12}$$

Scanning these vectors in 3-dimensions traces a sphere in reciprocal space, the surface of which represents wavevector conserved elastic scattering [77].

The requirement that $\Delta\mathbf{k} = \mathbf{G}_{hkl}$ positions and orients the sphere within reciprocal space. $\mathbf{G}_{hkl}$ is defined as the vector which lies between the origin of the reciprocal lattice and the reciprocal lattice point of the (hkl) planes; thus both of these points must lie on the surface of the Ewald sphere in order for diffraction conditions to be satisfied, as demonstrated in figure 3.4 (in the interests of clarity, a 2-dimensional section of the sphere is shown) [77].

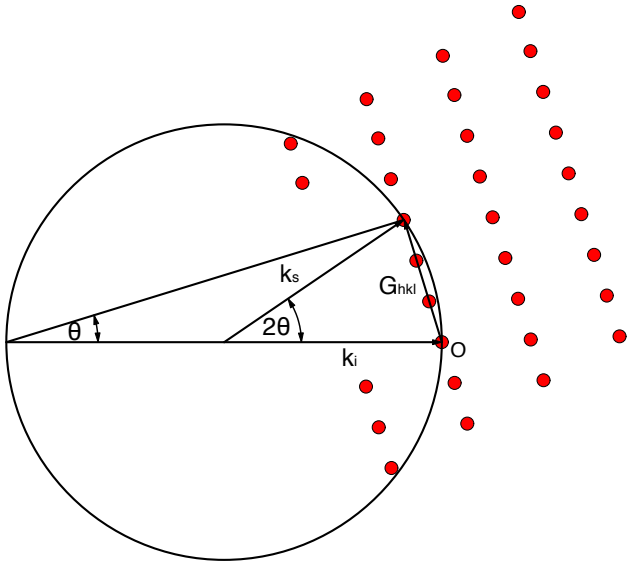

Figure 3.4: 2-dimensional section of Ewald's sphere demonstrating conditions required for diffraction [77].

Figure 3.4 demonstrates the Ewald sphere and reciprocal lattice under conditions of diffraction, these conditions are generally not satisfied however. In order to achieve the configuration of figure 3.4 one can envisage rotation of the reciprocal lattice about O or alteration of the sphere's radius. The former technique is utilized routinely in laboratory applications, exemplifying the previously stated angular dependent intensity distribution, while considerations pertaining to the latter are important when dealing with "white-light" X-ray sources e.g. synchrotron sources (introduced in chapter 4) due to the relationship between the wavelength of the light and the wavevector magnitude (3.12).

Structure Factor

The discussion thus far has concentrated on the diffraction criteria within a simplified structure, containing only a single source of scattered light per unit cell. In reality this is not the case, and there are two general deviations which must be considered: multiple atoms per unit cell, and multiple dipoles per atom. These extensions are accounted for by the crystal's structure factor.

For the multiple atom per unit cell consideration, the structure factor is calculated in a manner similar to that described previously in this section, i.e. the intensity of scattered light is proportional to [79],

$$e^{(-2\pi i \Delta \mathbf{k} \cdot \mathbf{r})} = e^{[-2\pi i (\mathbf{h}u + \mathbf{k}v + \mathbf{l}w)]} \tag{3.13}$$

where the {\textbf r} vector has been repurposed to represent the fractional position of the atoms within the unit cell. The structure factor is then calculated by summing over all atoms in the unit cell with regard to phase [79],

$$F_{hkl} = \sum_i f_i \exp\left[-2\pi i \left(hu + kv + lw\right)\right] \tag{3.14}$$

The coefficient introduced in (3.14), f_i, is the atomic scattering strength of atom i, and accounts for the presence of multiple dipoles per atom. Were it the case that all electrons within the atom were localized at a point, the atomic scattering strength would be given by simply multiplying the electronic scattering strength by Z, the atomic number. This however is not the case, as, due to X-rays' short wavelength, the inter-electron distances within the atom must be treated as non-zero entities, thus necessitating addition with regard to phase. This results in an expression similar to (3.14) with the exception that this expression must involve an integral due to the continuous nature of the electron distribution within the atom [79],

$$f_i = \int_{space} \rho\left(r\right) \exp\left(2\pi i \Delta \mathbf{k} \cdot \mathbf{r}\right) dV \tag{3.15}$$

where $\rho(\mathbf{r})$ is the electron probability density.

It should be noted that the addition with regard to phase involved in (3.14) can, for some lattice planes, result in a vanishing structure factor thus "forbidding" reflections from these planes, examples of this are (001) and (002) planes in silicon [79].

3.5 Experimental Details

Instrumentation

From Bragg's law, it can be inferred that high levels of crystallinity are required within the sample in order to satisfy equation (3.1) for only one angle; indeed peak broadening is indicative of crystallinity relaxation within the sample, as the Bragg condition is satisfied for not only one angle but a range of angles owing to, among other things, a distribution of inter-atomic spacings.

The sample is not the only source of such broadening. Major sources of error in XRD measurements are the divergence and spectral range of the radiation beam. These statistical spreads result in a distribution of incident angles ($d\theta$) and wavelengths ($d\lambda$) resulting a distribution in the exit angle. The effect of this angular distribution on exit can be to conceal the crystalline details of greatest importance, a case in point is lattice strain which manifests itself as very slight deviations in the lattice parameter.

Due to the limitations imposed by beam divergence and spectral distribution, the XRD experimental set-up has been expanded to include a beam conditioner before the sample (double axis configuration); in this configuration the experiment becomes a high resolution x-ray diffraction (HR-XRD) measurement. Diffraction calculations are based on monochro-

matic plane waves, the beam conditioner is generally a crystal of high quality whose diffracted output approaches this theoretical ideal [79].

A further extension of this set up involves the inclusion of an analyzer crystal before the detector (triple axis configuration). This crystal reduces the acceptance angle of the detector and allows the separation of the effects of strain and tilt [79], nevertheless it also reduces the detected intensity and therefore its incorporation is not universal.

The HR-XRD tool used in this project is a Jordan Valley/Bede D1 Diffractometer. This is a triple axis diffractometer capable of angular resolutions of ∼5 arcsec. This level of resolution allows distinction between lattice tilt, lattice strain and lattice composition, through the recording of reciprocal space maps (RSM). A schematic of the set up is shown in figure 3.5. A description of the main components follows.

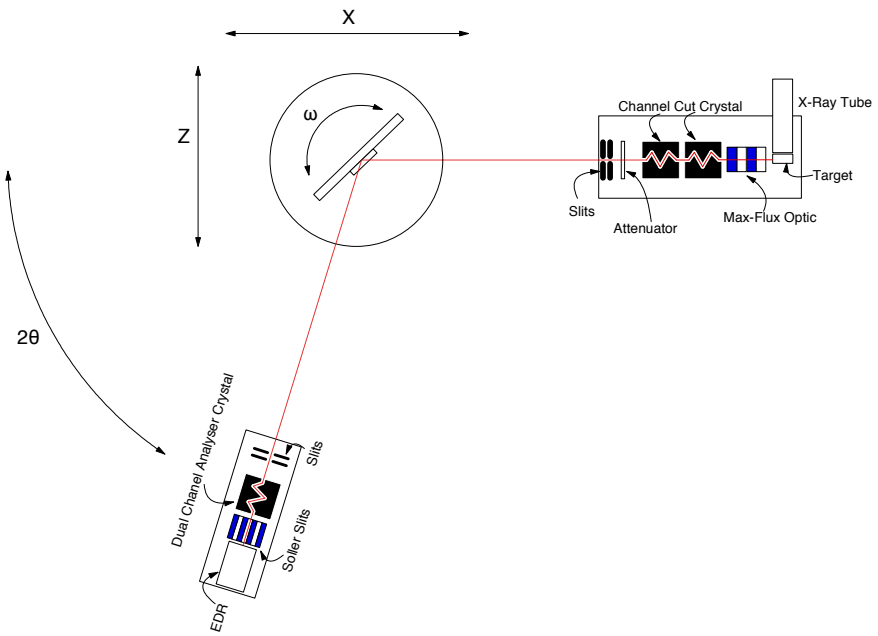

Figure 3.5: Schematic diagram of the JV/Bede D1 diffractometer. Also indicated are the major degrees of freedom associated with the plan view [79].

Source Stage

X-Ray Tube and Target: The X-ray source employed here is a Be tube with a Cu target. The CuK_α characteristic line (wavelength of 1.54056 A) is used for exposures with the CuK_β line selectively filtered.

The Max Flux^{TM}: The Max Flux^{TM} optic maximizes the usable intensity of x-rays from the source [80]. It is specifically designed for use with X-ray radiation and comprises of a series of bi-layers of high and low atomic number materials as shown in figure 3.6. The alternating atomic numbers of the layers provides an alternating electron density, making the layers analogous to crystal lattice planes. This structure invokes Bragg's law, however the increased "lattice-spacing" (in this case defined as the total width of an individual bi-layer) allows a wider selection of divergent incident x-rays to be diffracted. The structure is fabricated with a parabolic curve in order to allow beam collimation. The post Max Flux^{TM} beam divergence is $\sim 0.1°$.

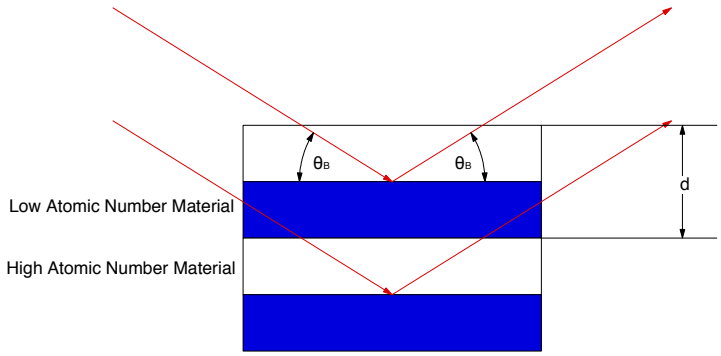

Figure 3.6: Schematic diagram of Max Flux^{TM} optic with high and low atomic number material bi-layers [79].

Channel-Cut Crystals: The channel-cut crystals (CCC) further condition the beam allowing

the system to operate in high-resolution mode. The CCCs are Si (022) crystals and operate as a pair. There are two configurations; high intensity (2 bounce asymmetric channel) and high resolution (4 bounce symmetric channel), shown in figure 3.7. In high intensity mode the output beam divergence is ~ 12 arcsec and is suitable for high resolution $\omega - 2\theta$ scans. In order to obtain RSMs, the system must be set up in high resolution mode allowing beam divergence of ~ 5 arcsec. These CCCs result in greatly reduced beam divergence, suitable for high resolution applications however they reduce the intensity of the x-ray beam reaching the sample and so, unless high-resolution measurements are required these generally are not incorporated.

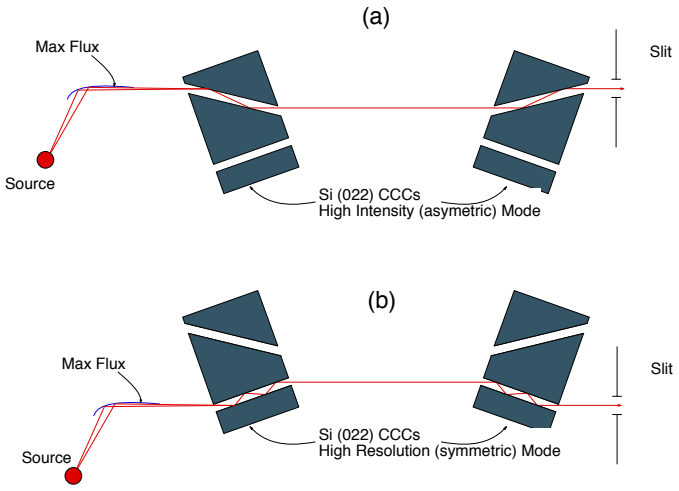

Figure 3.7: Schematic diagram of the two in-line Si (022) channel cut crystals in (a) high intensity and (b) high resolution modes [79].

Slits & Attenuators: A series of manually inserted slits and attenuators are used to define the beam for various applications, e.g. attenuators or slits are used during the sample alignment process, when the direct beam intensity measurement is required, in order to prevent damage to the detector.

Goniometer & Sample Stage

Goniometer: The goniometer provides independent rotational capabilities (about a common axis) for the sample stage and detector.

Sample Stage: In addition to the goniometer rotation, the sample stage can be moved in the traditional x, y, z dimensions as well as rotating relative to the horizontal (χ), and in-plane (φ). These degrees of freedom allow the sample to be aligned accurately in the beam and allow the selection of individual lattice plane reflections.

Detector Stage

Slits: The detector stage slits define the x-ray beam incident on the detector and are used to further collimate the detected beam.

Dual Channel Analyzer Crystal (DCA): The DCA is used to limit the acceptance angle of the detector. As the name suggests this crystal has two channels cut into it, one for high resolution measurements and one for high intensity measurements. The DCA is a crystal similar to that of the CCC shown in (3.7) The high resolution channel is a four bounce channel cut symmetrically to Si 022 planes and results in an acceptance angle of ~ 5 arc seconds. The high intensity channel is a two bounce channel cut asymmetrically to Si 022 planes and give an acceptance angle of 12 arc seconds [80]. The DCA is an optional element of the set up and moving it out of the beam path configures the system in the double axis mode as described subsequently.

Reflex Soller Slits: Soller Slits are a series of parallel channels which can be incorporated into the set-up allowing the detection of a spatially wide beam but also minimizing the acceptance angle. Soller Slits are generally used when investigating polycrystalline materials,

thus allowing a larger exposure area and therefore a higher intensity.

Enhanced Dynamic Range Detector (EDRc): The final component of the system is a 50 mm, scintillator (YAP:Ce) EDRc detector. This detector has a "dark" background level of $\sim$ 1-1.5 cps and a saturation level of $\sim$ 5 Mcps [80].

Modes of Operation

XRD experiments can be run in many modes of operation, from the coarse "rocking curve" to the comprehensive "reciprocal space map". The property to be measured, the accuracy required and time constraints will largely dictate the appropriate experimental course of action.

The most basic XRD experiment is the ω scan or "rocking curve". In this configuration the detector angle is fixed at twice the Bragg angle of the crystal planes of interest, the sample is rotated through a suitable angular range about the Bragg angle as exemplified by figure 3.8.

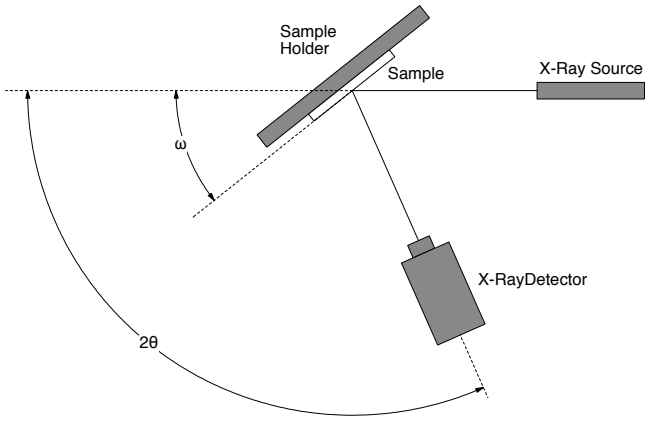

Figure 3.8: Rocking curve experimental setup and variables. Detector position is held stationary as the sample angle is scanned through a suitable range.

Rocking curves measure the inter-planar spacing of an individual set of planes selected by the detector angle and give information on a sample's crystallinity and tilt mosaic via the peak width.

An extension of this technique is the $\omega - 2\omega$ scan (figure 3.9) which scans the detector angle at a rate twice that of the sample angle and thereby records diffracted signals from multiple plane sets. $\omega - 2\omega$ scans are used to investigate lattice composition and mismatch in epilayer structures, a more general name for these scans are $\omega - 2\theta$, where θ can be taken to be equal to ω (for symmetric lattice planes).

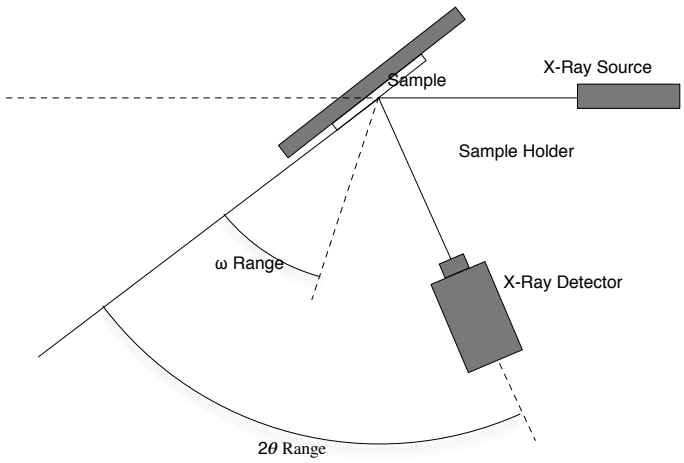

Figure 3.9: $\omega - 2\omega$ experimental set-up and variables. Sample angle is scanned through a suitable range, detector angle is driven at a rate twice that of the sample.

The most comprehensive mode of operation in HR-XRD is the "reciprocal space map" (RSM). RSMs provide information on composition, tilt and strain. An RSM is a compilation of $\omega - 2\theta$ scans in which the ω range of each scan is off-set by an amount ω_{rel}. The acquisition of RSM data takes advantage of the more general, decoupled expression of HR-XRD variables i.e. $\omega - 2\theta$ as opposed to $\omega - 2\omega$ for both symmetric and asymmetric lattice planes. In the case of the initial scan, where ω_{rel} equals zero, 2θ equals 2ω (for symmetric lattice planes) and the two expressions are equivalent, but for subsequent scans, 2θ becomes equal to $2\omega + \omega_{rel}$, this is demonstrated in figures 3.10 (a) and (b).

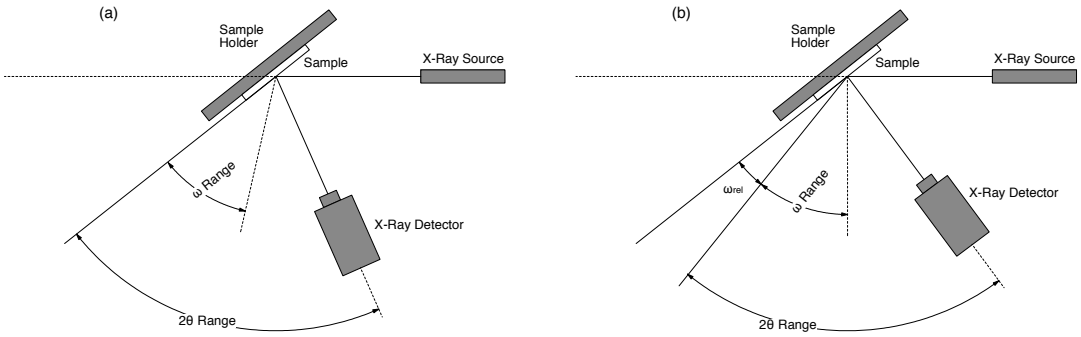

Figure 3.10: (a) Initial RSM scan: ω_{rel} equals zero, therefore this scan is simply an $\omega - 2\omega$ scan. (b) Subsequent scans in the production of an RSM introduce a non-zero and increasing ω_{rel} and therefore necessitate the use of the decoupled terminology of $\omega - 2\theta$.

By compiling a series of the off-set scans, a 2-dimensional intensity map can be built up, as exemplified in figure 3.11. In addition to inter-planar spacing, due to the fact the HR-XRD scans have been recorded over a range of sample tilts, the recorded intensities also hold information on lattice tilt (the $\omega - 2\theta$ axis is sensitive to lattice spacings and the ω_{rel} axis is sensitive lattice tilt). Four RSMs recorded at 90° azimuthal rotation intervals are required to fully define the lattice tilt.

Figure 3.11: (224) glancing incidence reciprocal space map of an unimplanted $Si_{0.70}Ge_{0.30}$ annealed at 700°C. The intensity is presented in arbitrary units.

Data Processing

In the forgoing sections, the method generating an RSM has been developed, however, in order to interpret a series of RSMs in a meaningful way further data manipulation is required.

The RSMs considered in this investigation are (224) glancing incidence reciprocal space maps. This experimental configuration provides additional sensitivity to thin surface layers through the low angle of incidence, and concomitantly increased x-ray pathlength. The asymmetric nature of the diffracting planes additionally allows simultaneous measurement of both in-plane and out-of-plane lattice constants.

The Jordan Valley D1 system initially aligns to the substrate peak and takes all measurements relative to this (figure 3.11). In order to interpret the recorded RSMs, the relative $\omega - 2\theta$ and ω_{rel}, coordinates of figure 3.11 must be transformed into absolute coordinates in reciprocal and angular space. These transformations were carried out by the Bede Contour software package, a program which comes bundled with the diffractometer. These transformations are in principle quite intuitive as they take advantage of the theoretically known Bragg angle and reciprocal lattice dimensions of silicon. To these values are added the measured relative values. Figure 3.12 shows figure 3.11 transformed into absolute reciprocal and angular space. The procedures are briefly described in Appendix B.

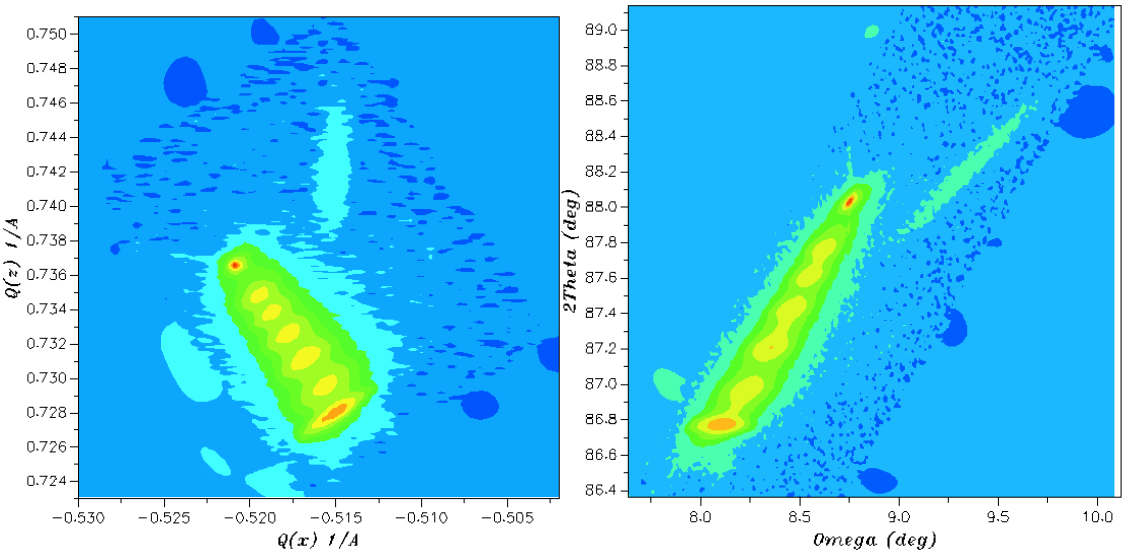

(a) Absolute Reciprocal Space (b) Absolute Angular Space

Figure 3.12: Absolute (224) glancing incidence (a) reciprocal and (b) angular space maps of an unimplanted $Si_{0.70}Ge_{0.30}$ annealed at 700°C. The intensity scale is the same as that of figure 3.11.

Lattice Constant Calculations

In order to calculate the parallel and perpendicular lattice constants corresponding to each peak recorded, the peak positions in q_x and q_y are averaged over RSMs recorded at azimuthal orientations separated by 180° (data presented is based on 0° and 180° azimuthal RSMs). This averaging compensates for any tilt which may alter the recorded angular, and therefore reciprocal space, peak positions. Using these mean values, the parallel and perpendicular lattice constants are given by [81]

$$\begin{aligned} a_{||} &= \sqrt{\frac{h^2+k^2}{q_x^2}} \\ a_{\perp} &= \sqrt{\frac{l^2}{q_z}} \end{aligned} \tag{3.16}$$

where $a_{||}$ and $a_{\perp}$ are the in-plane and out-of-plane lattice constants. For the strained silicon layer, the percentage strain can be calculated directly from these values through [81]

$$\left(\frac{\Delta a}{a}\right)_{\perp/||} = \left(\frac{a_{\perp/||x} - a_x}{a_x}\right), \tag{3.17}$$

where a_x is the lattice constant of silicon.

Determination of the strain level within the SiGe layer (top, constant compositional layer) requires the additional consideration of the variable germanium content. In order to analyze this layer, one must firstly determine the lattice constant of the layer were it entirely relaxed, this is given by [81]

$$a_r = a_{||} + \frac{1-\nu}{1+\nu}\left(a_{\perp} - a_{||}\right) \tag{3.18}$$

where ν is Poisson's ratio of the layer. Having determined the relaxed lattice constant, the germanium content is given by [81]

$$x = \frac{a_{Ge} - a_r}{a_{Ge} - a_{Si}} \tag{3.19}$$

and the degree of relaxation in the layer is given by [81],

$$R = \frac{a_{||} - a_{Si}}{a_r - a_{Si}}. \tag{3.20}$$

Lattice Tilt Calculations

During growth, unintentional miscuts in the lattice are common, resulting in the non-zero angular offset between the surface normal and the crystallographic [001] direction. Once present, as detailed in chapter 4.5, this miscut gives rise to non-zero net out-of-plane Burgers vectors and additional tilt components. Figure 3.13 demonstrates the various tilts within the

sample. α being the angle between the substrate [001] direction and the surface normal (i.e. the miscut), β being the angle between the epilayer [001] direction and the surface normal and γ being the relative tilt between the substrate and epilayer [001] directions.

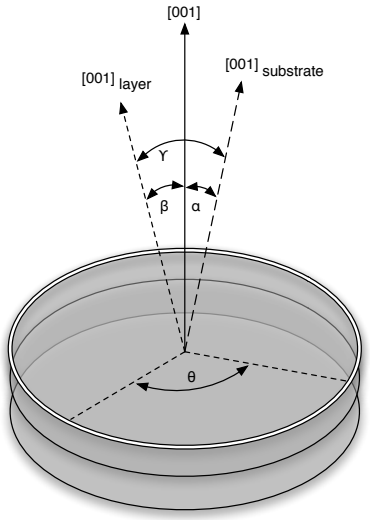

Figure 3.13: Demonstration of the various tilts encountered within a crystalline epitaxial structure. α is the angle between the substrate [001] direction and the surface normal (i.e. the miscut), β is the angle between the epilayer [001] direction and the surface normal and γ is the relative tilt between the substrate and epilayer [001] directions [81].

The tilt is measured through the analysis of four 224 reciprocal space maps recorded under 90° relative azimuthal rotation. The lattice tilt within a layer is definable through the translation of its ω peak position along the tilt direction (a line perpendicular to that joining the reciprocal lattice point to the reciprocal space origin). In the previous section, taking the average ω peak position of two scans taken with an azimuthal separation of 180° removed the effects of lattice tilt, in the current investigation, it is the magnitude of this separation which is of interest. Taking two such sets of scans, mutually perpendicular, allows the full definition of the tilt magnitude and orientation. With this in mind, the tilt magnitude of a

layer is given by [81],

$$Tilt = \frac{1}{2}\sqrt{(\omega_2 - \omega_4)^2 (\omega_1 - \omega_3)^2} \tag{3.21}$$

and the tilt orientation, relative to the [110] direction, is given by,

$$\theta = \tan^{-1}\left(\frac{\omega_2 - \omega_4}{\omega_1 - \omega_3}\right) \tag{3.22}$$

3.6 Results & Discussion

Due to reliability issues with the J.V. Semiconductor D1 used for reciprocal space map collection, and the time taken to collect a full data set (4 RSMs can take up to a week to collect depending on the chosen parameters), it was not feasible to fully characterize all samples in our matrix. The measurements undertaken on the D1 were carried out with the following goals in mind: investigation of the stability of processed ε-Si layers approaching critical thickness; investigation of the impact, if any, of strain relaxation on electrical activation; and investigation of the relative stability of the ε-Si layers grown on linear and terrace graded VS; and the provision of data complementary to that of other techniques. This complementary data is presented in subsequent chapters, while the current chapter deals with the first three investigative goals.

In order to investigate the resilience of near-critical thickness layers against processing, the $Si_{0.77}Ge_{0.23}$ and $Si_{0.70}Ge_{0.30}$ terrace graded samples, implanted with 1×10^{15} Sb cm^{-2} and annealed at 700°C (800°C anneals were not available at high strain) were investigated. The second goal above was satisfied through the investigation of the $Si_{0.83}Ge_{0.17}$ linearly graded, 6×10^{14} Sb cm^{-2} implanted samples as these demonstrated maximum electrical activation. The strain stability of these $Si_{0.83}Ge_{0.17}$ samples in conjunction with the similarly strained 1×10^{14} Sb cm^{-2} implanted samples was compared with the aforementioned terrace graded samples to allow the relative stabilities of the two structures to be determined. Each of

these investigative goals will be considered in turn, however, prior to this, the measured germanium content of the investigated samples is presented as this provides the frame of reference for all other data.

SiGe Germanium Content

The lattice constant of the ε-Si template provided by the $Si_{1-x}Ge_x$ VS is dependent on two factors: the germanium content and percentage relaxation. Figure 3.14 plots the measured germanium content in two wafers at each strain level currently considered. For comparative purposes, the nominal germanium content as specified by the manufacturers is additionally plotted. The labels of figure 3.14 indicate the percentage relaxation in the layers. Where multiple measurements of an individual wafer were taken, e.g. measurements taken after processing under various conditions, the average data is presented.

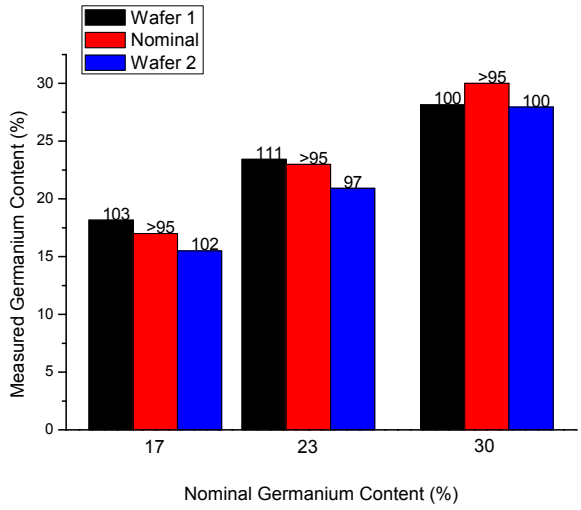

Figure 3.14: HR-XRD measured virtual substrate for three nominal germanium contents. The labels indicate the percentage relaxation in the layers. It should be noted that the $Si_{0.83}Ge_{0.17}$ Ge samples were sourced from IQE whereas the $Si_{0.77}Ge_{0.23}$ and $Si_{0.70}Ge_{0.30}$ Ge samples were sources from Advansis.

In figure 3.14, some of the wafers investigated demonstrate relaxations > 100%; in the literature, this has been attributed to thermal expansions and variations between the thermal expansion coefficient of the layer and the referenced substrate [82]. The data of figure 3.14 demonstrate large variations in the germanium content within the nominally 17% and 23% germanium samples. Although the nominally 30% germanium samples have a more consistent germanium content, this falls below the specified value. These discrepancies between specified and measured germanium contents mean the validity of any strain calculations based on specified germanium contents are called into question. Table 3.1 shows the strain variations resulting from the germanium contents of figure 3.14.

Specified Ge Content [%]	Predicted $\varepsilon - Si$ Strain Values [%]	Measured Ge Content [%]	Corrected $\varepsilon - Si$ Strain Values [%]
17	0.71	18.1	0.76
17	0.71	15.1	0.63
23	0.96	23.4	0.98
23	0.96	20.75	0.87
30	1.25	27.89	1.16
30	1.25	28.8	1.17

Table 3.1: Expected strain levels within fully strained ε-Si layer grown on VS of nominal and measured germanium content.

Strained Si Stability

Figures 3.15 (a) & (b) plot the strain levels of the linear and terrace graded sample subsets currently considered. The sample sets presented vary slightly due to the previously stated investigation goals. The $Si_{0.83}Ge_{0.17}$ linearly graded samples were chosen to extract

information on the strain levels within the optimally activated samples of chapter 2, i.e. the 6×10^{14} cm^{-2} Sb implants (the strain data of the 1×10^{14} cm^{-2} implanted samples is additionally shown). The terrace graded samples considered are those subjected to the most rigorous processing steps available within the sample set.

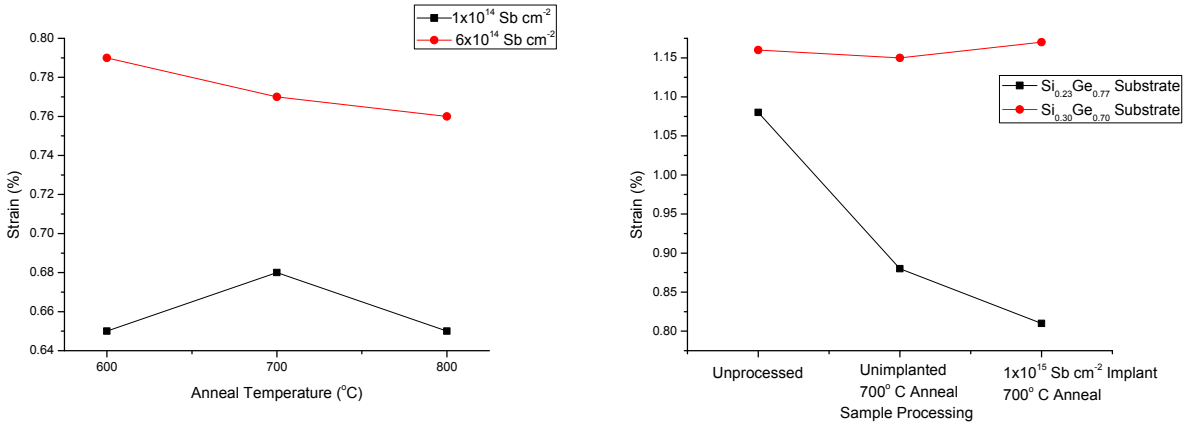

(a) Linear (b) Terrace

Figure 3.15: Measured strain within the ε-Si layers grown on (a) linearly graded and (b) terrace graded virtual substrates. The data sets in each vary in accordance with the investigative goals previously set out. The size of the error bars within these graphs are on the order of the symbol size.

The data of figure 3.15 taken in isolation, give information on the absolute strain levels within these samples but provides no insight into the stability of the layers as it takes no account of the variable lattice constant within each underlying VS. In order to identify strain relaxation within the ε-Si layers, as opposed to simply a reduced VS lattice constant, figure 3.16 plots the measured in-plane lattice constants within both the ε-Si and $Si_{1-x}Ge_x$ layers for each sample.

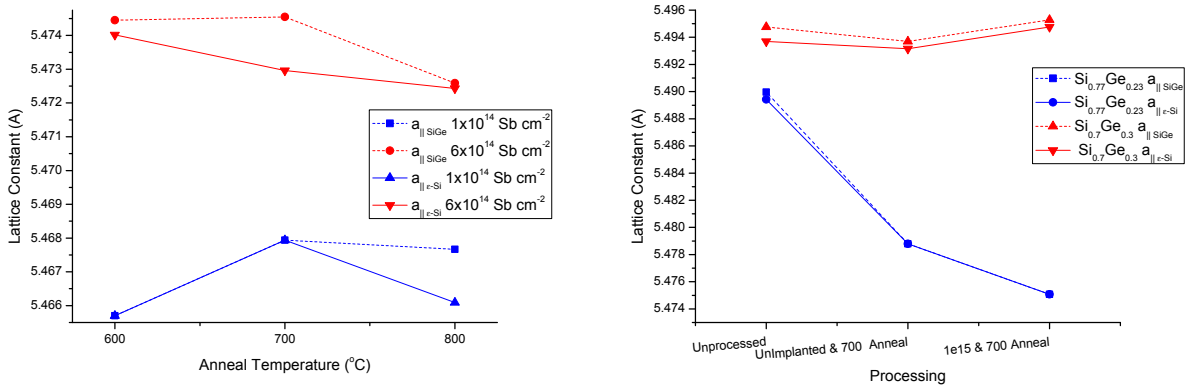

(a) Linear (b) Terrace

Figure 3.16: In-plane lattice constants of ε-Si and underlying $Si_{1-x}Ge_x$ layers. The size of the error bars within these graphs are on the order of the symbol size.

The data of figure 3.16 demonstrate extremely stable ε-Si layers on the terrace graded VS. The linearly graded VS samples show much less stability with the 1×10^{14} Sb cm^{-2}, $800°C$ sample demonstrating significant strain relaxation in the ε-Si layer. Figure 3.17 summarizes the previous graphs, plotting the in-plane lattice constant of the ε-Si layers against those of their respective $Si_{1-x}Ge_x$ VS. Also plotted is the line along which fully strained data points lie, any points below this line indicate some level of strain relaxation.

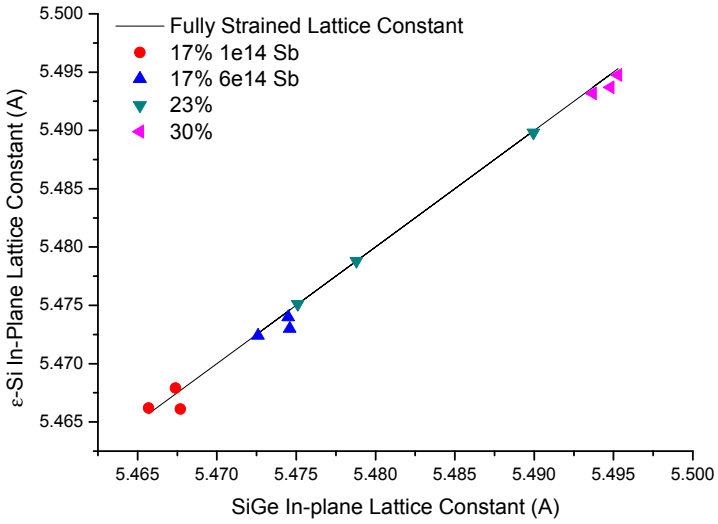

Figure 3.17: ε-Si in-plane lattice constant plotted against $Si_{1-x}Ge_x$ in-plane lattice constants. The data points represent measured data while the linear plot identifies the position of fully strained ε-Si layers.

A question remaining to be answered is whether the strain relaxation in the layers is driven by threaders originating in the $Si_{1-x}Ge_x$ VS or whether the layer thicknesses are such that misfit dislocation generation becomes permissible. In order to investigate this, figure 3.18 plots the percentage registry between the ε-Si layers and their $Si_{1-x}Ge_x$ VS against the layer thickness normalized with respect to its theoretical critical thickness.

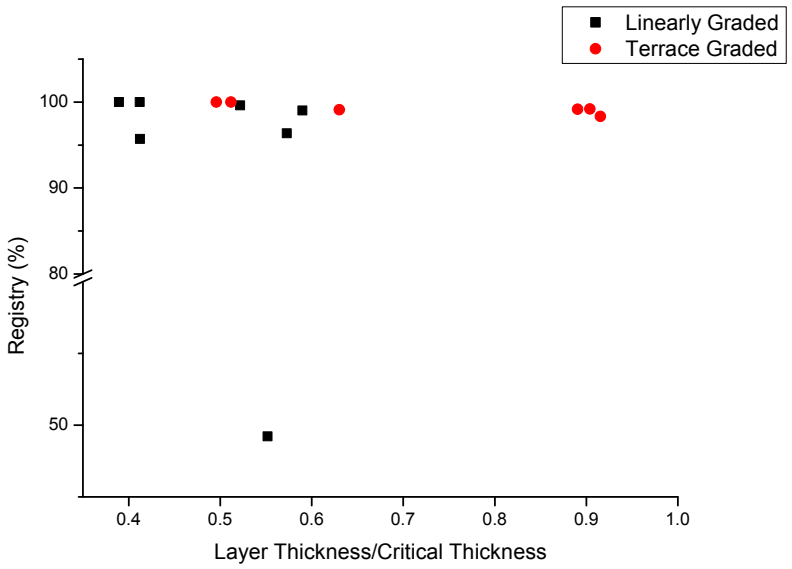

Figure 3.18: Percentage registry versus layer thickness normalized against the theoretical critical thickness of the layer. The large degree of relaxation in the outlying linearly graded sample is most likely attributable to the presence of pre-existing threading dislocations.

Figure 3.18 underscores the stability enhancement in the ε-Si layer grown on terrace graded VS. The strain relaxation in ε-Si layers grown to thicknesses as low as 40% of their critical thickness in the linearly graded samples is indicative of the presence of ingrown threading dislocations. Although not all linearly graded samples demonstrate significant strain relaxation, the relative stability of the terrace graded VS ε-Si layers with normalized critical thicknesses as high as 0.9, indicates the added stability provided by this form of VS. It should be additionally noted that all thicknesses have been taken from specifications and therefore it is possible that the $Si_{0.70}Ge_{0.30}$ samples exceed their critical thickness accounting for the slight relaxation of strain across these samples. These finding are in aggreement with those of similar investigations in the literature [83], [27].

Sb Activation and Strain

Chapter 2 demonstrates antimony deactivation subsequent to the 800°C anneal. Lai *et al.* and Bennett *et al.* have attributed this deactivation to Sb cluster formation, as opposed to effects related to strain relaxation. The strain data presented on the linearly graded samples would appear to support this supposition as the level of strain relaxation upon 800°C anneal in these samples is minimal. In order to further substantiate this supposition solid solubility calculations based on the theory of Ahn *et al.* [26] are considered,

$$\frac{C^{ss}(\varepsilon)}{C^{ss}(0)} = \exp\left(\frac{V_0 \Delta\overrightarrow{\varepsilon}_A \cdot C \cdot \overrightarrow{\varepsilon}}{kT}\right) \tag{3.23}$$

where $\Delta\overrightarrow{\varepsilon}_A$ is the change in strain resulting from a single antimony atom in an activation limiting cluster, C is the elastic stiffness tensor of silicon, V_0 is the activation volume of an antimony atom (dealt with in chapter 1.3) and $\Delta\overrightarrow{\varepsilon}$ is the strain. According to (3.23), the reduction in strain from 0.77% to 0.76% between the 700°C annealed and 800°C annealed samples should cause a reduction in antimony solid solubility of ∼1.73%, thus accounting for only a small fraction of the 34.6% deactivation observed. Due to this discrepancy the strain relaxation would appear not to be the precursor to deactivation, lending further credence to the supposition of deactivation through cluster formation.

Tilt Measurements

In order to monitor the tilt evolution within these samples, additional RSMs were measured on a selection of these. In the case of each sample, the lattice tilts of the silicon substrate, the constant compositional $Si_{1-x}Ge_x$ layer and the ε-Si layer relative to the sample surface are reported.

Figure 3.19 shows the experimental data for the lattice tilts measured in the $Si_{0.77}Ge_{0.23}$

terrace graded samples. This figure plots the lattice tilt magnitudes and orientations (relative to the [110] direction.

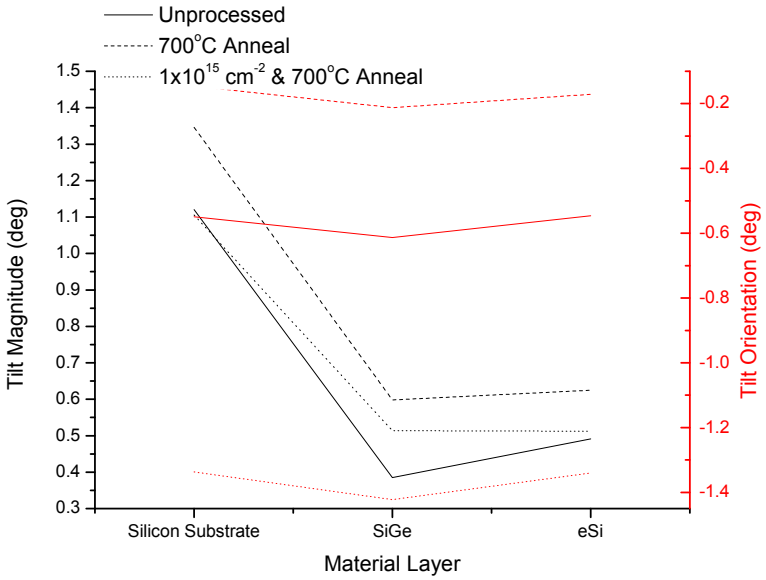

Figure 3.19: Lattice tilt magnitudes and orientations relative to the [110] direction within the $Si_{0.77}Ge_{0.23}$ terrace graded samples.

The general magnitude trends of figure 3.19 are in line with the asymmetric introduction of oppositely sensed misfit dislocations in the presence of a lattice miscut. The tilt of the silicon substrate in all samples provides the miscut in question. The large number of misfit dislocations required for relaxation of the $Si_{0.77}Ge_{0.23}$ layer then drives the reduction in the measured tilt. The minimal strain relaxation in the ε-Si layer results in very little change in the tilt magnitude across this layer.

Figure 3.20 shows the lattice tilt data for the measured $Si_{0.70}Ge_{0.30}$ samples. The trends here are largely similar to those of the $Si_{0.77}Ge_{0.23}$ samples with the same rational.

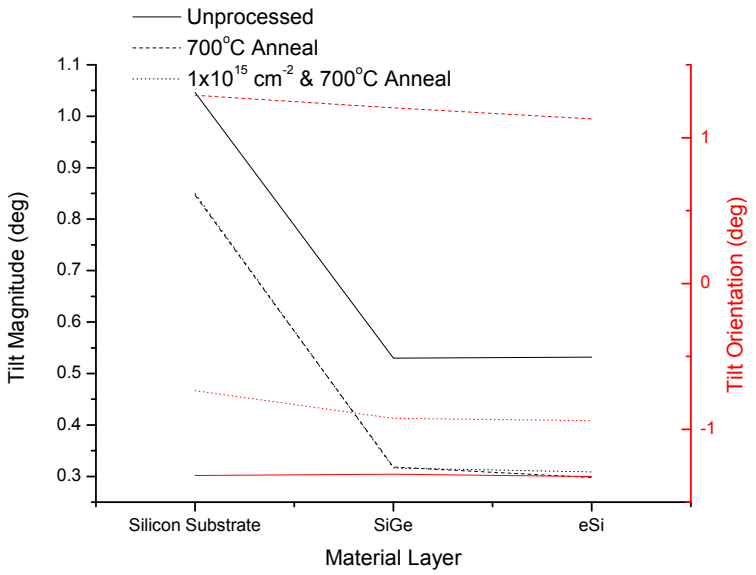

Figure 3.20: Lattice tilt magnitudes and orientations relative to the [110] direction within the $Si_{0.7}Ge_{0.30}$ terrace graded samples.

Tilt trends within the linearly graded samples differ from those measured in the terrace graded samples as shown in figure 3.21.

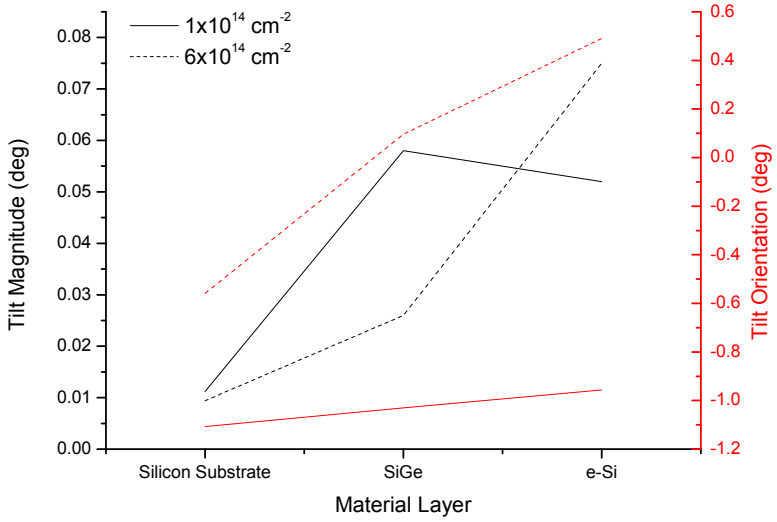

Figure 3.21: Lattice tilt magnitudes and orientations relative to the [110] direction within the $Si_{0.83}Ge_{0.17}$ linearly graded samples.

The increase in the tilt magnitude from the silicon substrate into the ε-Si layer suggests a mechanism of tilt production unrelated to the opposition of a pre-existing lattice miscut. Indeed the minimal tilt demonstrated by these silicon substrates indicates that the miscuts in these samples are negligible. A possible source of this lattice tilt is surface roughness. As opposed to the coherent tilting discussed previously, surface roughness results in locally tilted regions, mis-oriented with respect to each other. Globally these tilts generally average to zero, accounting for the small tilts measured (roughly an order of magnitude smaller than that observed in the terrace graded samples).

3.7 Conclusions

The current HR-XRD measurements, although not exhaustive, have largely achieved the investigative goals of the project relating to the impact of ion-implantation and annealing on the stability of strained silicon layers. The increased stability of layers grown on terrace graded VS as opposed to linearly graded VS has been confirmed. Little strain relaxation was observed in the terrace graded samples beyond that expected at critical thickness, while the linearly graded substrate samples, with thicknesses well below their critical thickness, have demonstrated relaxation most likely due to the presence of high threading dislocation densities.

Strain relaxation has been demonstrated not to be the major precursor to electrical deactivation within these samples, indicating the validity of previous assertions attributing this to clustering effects.

Of most concern within these samples is the variability of the germanium content in the $Si_{1-x}Ge_x$ VS. This impacts on the strain imparted to the ε-Si layers and all related properties.

Chapter 4

Synchrotron X-Ray Topography

The previous chapter quantified the strain levels and lattice tilts within a sub-set of the samples. This analysis revealed strain relaxation within the $Si_{1-x}Ge_x$ virtual substrate, and the emergence of lattice tilt owing to initial substrate miscut. In order to investigate the mechanisms of strain relaxation within the virtual substrates, and to identify other defect types within the samples, synchrotron x-ray topography was used. A survey of lattice tilt was also carrier out.

4.1 Introduction

X-ray topography is concerned with the intensity distributions over what would, in diffractometry, be considered a diffraction peak. During passage through the crystal, the x-ray beam interacts with both defects within the crystal and other propagating waves. These interactions result in intensity fluctuations detectable through the use of x-ray film or CCD devices. X-ray topographic techniques allow imaging of local tilt and strain effects associated with various crystalline defects.

4.2 Historical Background

The first x-ray topographic experiment followed roughly 20 years after that of x-ray diffraction. In 1931, Berg revealed lattice perturbations in cleaved edges of sodium chloride [84]. This experiment was performed in the Bragg (back reflection) configuration. The first Laue (transmission) configuration experiment was performed by Barth and Hosemann in 1958 [85]. The practice of synchrotron x-ray topography (SXRT) was initiated by Tuomi *et al.* [86] who showed in 1974 that topographs could be taken within seconds using these high intensity, low divergence radiation sources.

4.3 Theory

SXRT shares much of its theoretical underpinnings with HR-XRD. The two techniques are differentiated in essence only by the resolution of their detection (x-ray diffraction integrates the incident intensity over the detector area, whereas x-ray topography images the local intensity distribution over the detector area). As a result, the theoretical considerations of the previous chapter hold true in the current context, however, additional considerations are required to interpret the intra-exposure intensity distributions. These considerations can be broken down into three categories; orientational contrast, extinction contrast and anomalous transmission. As all topographs presented currently were recorded in the back reflection configuration, only orientation contrast and beam extinction will be dealt with in the body of the thesis; however a description of anomalous transmission can be found in Appendix C.

Orientational Contrast

Lattice mis-orientation is the most intuitive source of XRT contrast and can be understood through purely geometrical considerations.

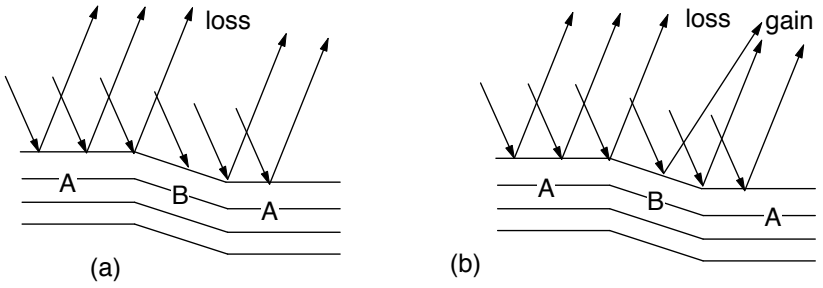

Figure 4.1: Demonstration of orientational contrast; (a) depicts the monochromatic case in which the misoriented region results in a loss of diffracted intensity. The white-beam situation (b) results in selection of a different x-ray wavelength and an offset diffraction angle, therefore while one detection region experiences loss of intensity, another region experiences gain [85].

Consider a crystal incorporating a region which is misoriented with respect to the otherwise perfect crystal (as depicted in figure 4.1). If a monochromatic x-ray beam is incident on the crystal, such that region A of figure 4.1 satisfies Bragg's law, the misorientation will result in no diffracted intensity originating from region B (depicted in figure 4.1 a) [85]. If alternatively, the incident x-ray is polychromatic (as in the case of white-light synchrotron radiation) one can envision a second wavelength being incident for which the angle of incidence on the lattice planes of region B does satisfy Bragg's Law. Under these conditions, the diffracted beams from region B will be offset, as shown in figure 4.1 b resulting in areas

of the topograph demonstrating loss and gain [85]. If the misorientation and area of the region are large enough, orientation contrast can result in entirely shifted topographs.

Beam Extinction

When investigating a thick crystalline sample in the Bragg (back-reflection) configuration, the provisions of dynamical theory require account be taken of both superposition of waves and multiple reflections. The result of these considerations, as explained below, is a penetration depth which is greatly reduced relative to that dictated by optoelectronic absorption alone. This reduced depth is called the "extinction depth".

Figure 4.2 depicts a situation in which a monochromatic, parallel light beam is incident on a perfect crystal. The beam 'Incident 2' is a superposition of the 'Incident 1' minus 'Reflected 1' (assuming no absorption) and the double reflected 'Reflected 3'. As each reflection introduces a $\frac{\pi}{2}$ radian phase shift, the double reflected 'Reflected 3' is π radians out of phase with respect to the incident beam [76]. As a result of this, destructive interference ensues between these two beams. The amplitude of the incident beam is thus attenuated beyond the effects of simple reflection and absorption and the diffracted intensity reaching the surface is similarly reduced.

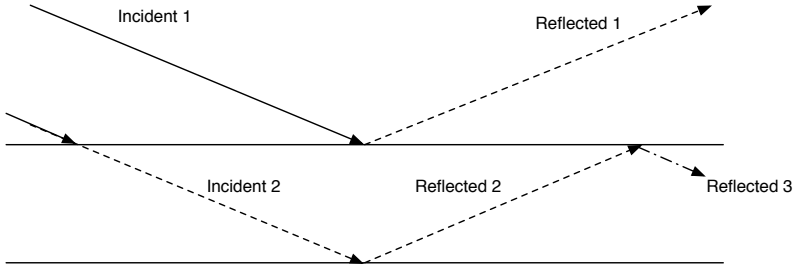

Figure 4.2: Schematic diagram depicting incident and reflected monochromatic, parallel beams in a perfect crystal. Due to coherent reflection and subsequent interference, the incident beam becomes quickly attenuated resulting in beam extinction [76].

This additional attenuation results in a much shallower penetration depth than would otherwise be expected, resulting in 'extinction' of the beam. In the presence of a defect, the extent of coherently scattered light is reduced, the extinction effect is thus diminished, resulting in additional intensity in both the incident and diffracted beams.

The intensity of x-ray scattered form a defect region is further increased through an increased scattering power. For a perfectly crystalline region the x-ray diffraction peak is characterized by an extremely small FWHM and maximum intensity. When considering a region surrounding a defect the relaxation of crystallinity results in an increased FWHM and a greatly reduced intensity. These peak shapes result in the integrated diffracted intensity being proportional to the magnitude of the material structure factor $|F|$ for the crystalline case and the square of the structure factor $|F|^2$ for the non-crystalline case [84]. Therefore, similar to above, increased diffraction intensities result from regions surrounding defects.

4.4 Experimental Details

Instrumentation

The images displayed in this work were taken at the ANKA (Angstroemquelle Karlsruhe) Synchrotron in Germany. This synchrotron light source consists of a 500 MeV injector and a 2.5 GeV electron storage ring and operates at a maximum current of 200 mA [87].

Figure 4.3 shows a schematic set up of the topography beam-line (TopoTomo). The source for this beam-line is a 1.5 T bending magnet constituting a white light synchrotron radiation source with horizontal and vertical divergences of 2 mrad and 0.5 mrad, respectively. The beam-line up to the experimental hutch is kept under high vacuum. In order that the experimental hutch itself does not need to be similarly evacuated, the beam-line is terminated with a berilium window. The beam size at the sample is defined by two sets of slits which have a maximum opening of $8mm \times 8mm$. The sample is mounted on a two-circle-goniometer allowing translation and rotation in 3 dimensions. The x-ray film used for the images shown was Slavich Geola VRP-M Holographic Film, with a grain size ∼35 nm.

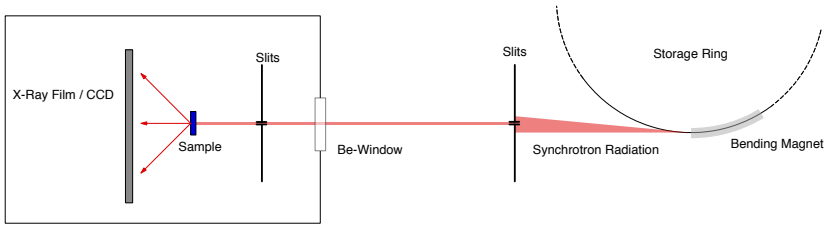

Figure 4.3: Schematic diagram of ANKA TopoTomo beam line showing synchrotron radiation originating at bending magnet.

Experimental Configuration

SXRT experiments can be carried out in 1 of 4 modes of operation: large area back reflection or transmission and section back reflection or transmission. A description of all four set ups can be found in Appendix C. The orientation of the experimental set-up used depends on the location of the defects of interest and the type of contrast most likely to reveal them. All topographs presented currently were recorded in the large area back reflection configuration and this currently described.

In the large area back reflection (LABRT) set-up, the dimensions of the incident x-ray beam are extended to a few millimeters in each direction. As described in figure 4.4 the LABRT configuration involves white beam synchrotron radiation passing through a central hole in the detection film. This is followed by Bragg reflection at the sample's surface and finally detection by high resolution x-ray film. This configuration investigates the surface region of the sample only and the depth which is investigated is determined by the penetration depth of the x-ray wavelength associated with the chosen reflection.

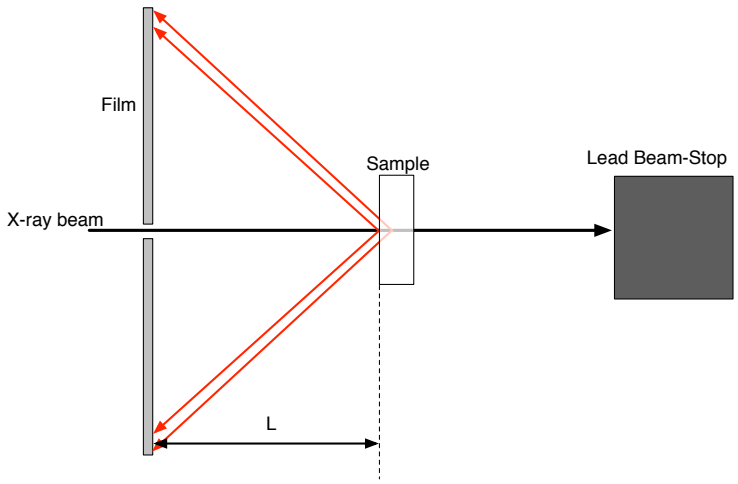

Figure 4.4: Experimental configuration for large area back reflection SXRT.

Data Processing

Due to the white light nature of the synchrotron radiation and the presence of multiple lattice plane sets, a single SXRT exposure results multiple exposed regions on the detection film. The pattern of these regions is imitative of the reciprocal lattice of the crystalline structure exposed (demonstrated in figure 4.5).

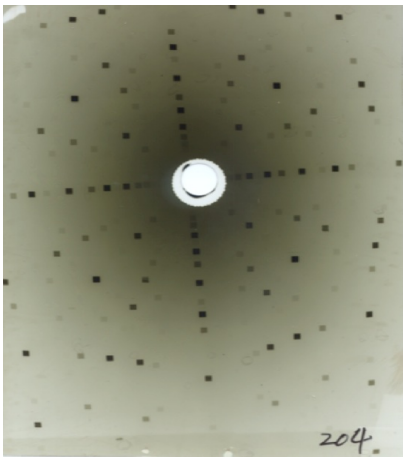

Figure 4.5: Back reflection Laue pattern of silicon, sample-to-film distance was 80 mm.

Each exposed region results from a satisfaction of Bragg's law and the intensity distribution within the region constitutes the topograph. The possibility exists that multiple wavelength/inter-planar spacing combinations may result in overlapping exposures. The fact that an exposure originates from more than one set of lattice planes, however, has little impact on the data interpretation beyond that fact that the penetration depth becomes a function of multiple wavelengths. The indexing convention adopted in the case of overlapping topographs, is that the exposure takes the index of the most intense reflection, otherwise known as the base reflection.

Once a topograph of interest has been identified, its lattice plane set and penetration depth must be determined.

Reflection Indexing

In order to determine the lattice planes responsible for a given reflection, the diffraction simulation software "Laue PT" [88] was used. This software generates a theoretical Laue pattern for a given material and experimental conditions (e.g. sample-to-film distance and any relative tilt between the two). A direct comparison with the simulated pattern allows a given experimental reflection to be indexed, the software then identifies the contributing fundamental and harmonic wavelengths in addition to their theoretical relative intensities.

Penetration Depth Calculation

Having indexed the reflection and identified the contributing wavelengths, it remains to determine the penetration depth of the wavelengths involved. The radiation penetration depth is given by [89],

$$t_p = \frac{1}{(\mu(\lambda))\left(1 + {}^{1}\!/_{\sin\alpha_f}\right)} \tag{4.1}$$

In (4.1) α_f is given by $\alpha_f = \alpha_i - Tan^{-1}\left({}^{H}\!/_{L}\right)$, where H is the distance on the film between center (direct beam) and the reflection of interest and L is the sample-to-film distance (as depicted for back-reflection configuration in figure (4.6). $\mu(\lambda)$ is the wavelength dependent absorption coefficient of the material [90]. Table 4.1 shows the calculated penetration depths of the reflections presented subsequently.

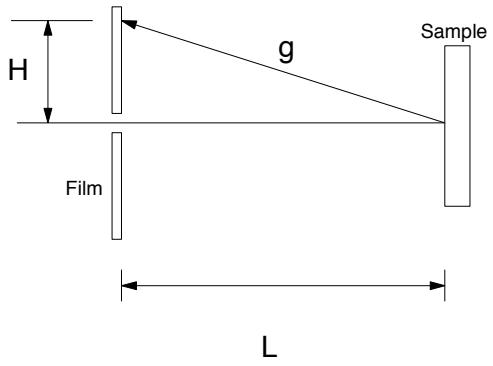

Figure 4.6: Back reflection configuration indicating H and L within (4.1), additionally, the diffraction vector **g** is indicated.

Reflection	Intensity [%]	L [mm]	H [mm]	λ [A]	d [A]	Penetration Depth [μm]
1 $\overline{1}$ 7*	100	80	33.66	1.491	0.76	37.41
2 0 6*	63.97	80	59.96	1.6292	0.8586	26.7
4 0 12	36.03	80	59.96	0.8149	0.4293	205.72

Table 4.1: Wavelengths and penetration depths of referenced reflections in silicon. * identifies fundamental reflections.

4.5 Results & Discussion

Misfit Dislocations

Within all virtual substrates the majority of strain relaxation occurs within the linearly graded regions. The strain relaxation proceeds by production and expansion of modified Frank-Read sources, which produce misfit dislocations lying in the orthogonal ⟨110⟩ directions.

Figure 4.7a is a large area back reflection topograph demonstrating these strain relieving misfit dislocations through the relaxed SiGe virtual substrate of a 10% Ge sample. This topograph is a $1\bar{1}7$ reflection with a penetration depth of 37.41 μm .

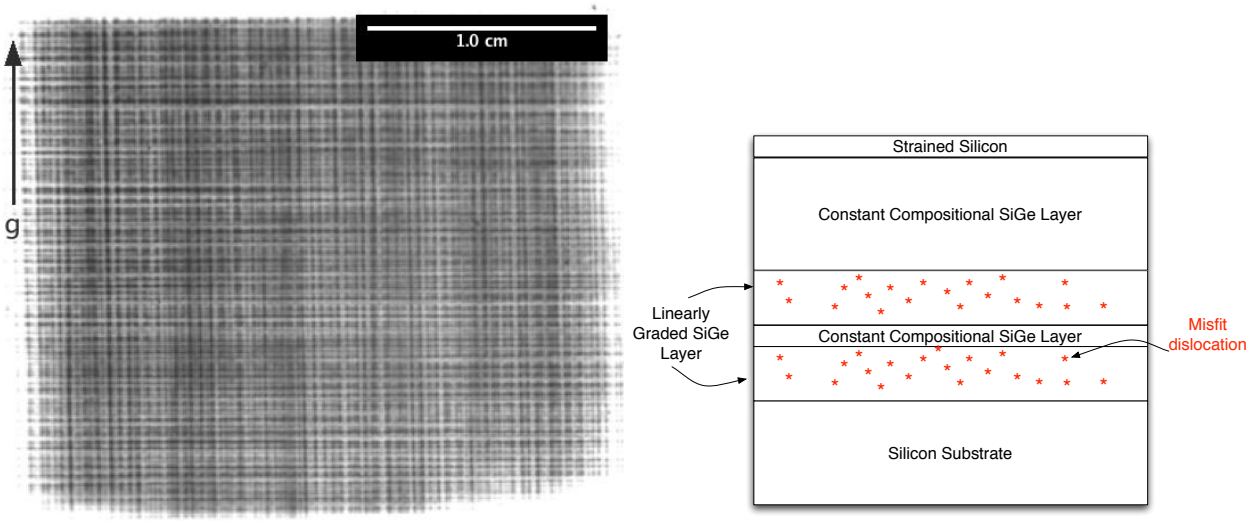

(a) Topograph (b) Schematic

Figure 4.7: a. 10 % Ge virtual substrate; $1\bar{1}7$ back reflection topograph demonstrating misfit dislocations lying in orthogonal ⟨110⟩ directions. Penetration depth of this topograph is 37.41 μm. b. Schematic indicating the location of the MDs within the sample structure.

The increased intensity in the vicinity of the orthogonal dislocations is consistent with the

breakdown of beam extinction in back-reflection configuration.

These strain relieving dislocations were observed in all strained samples imaged, with figure 4.7a being representative of the recorded images.

Lattice Tilt

Chapter 3 indicates the presence of lattice tilt within the $Si_{0.77}Ge_{0.23}$ and $Si_{0.70}Ge_{0.30}$ samples. Within the linearly graded, $Si_{0.83}Ge_{0.17}$ samples no appreciable tilts were found via HR-XRD measurements. Due to the extended measurement time required for full HR-XRD tilt analysis, this avenue of investigation was not feasible. Under the correct conditions, however, SXRT is capable of revealing lattice tilt and, with exposure times on the order of seconds, a full survey of all samples was possible.

Figure 4.8a demonstrates the presence of lattice tilt in the 23% Ge virtual substrate sample. This is evidenced by the presence of a well defined second topograph image, visibly displaced on the detection film. The clarity of the image indicates a large region of the lattice is coherently tilted with respect to the substrate. Figure 4.8b demostrates the origin of this off-set image, owing to lattice misorientation.

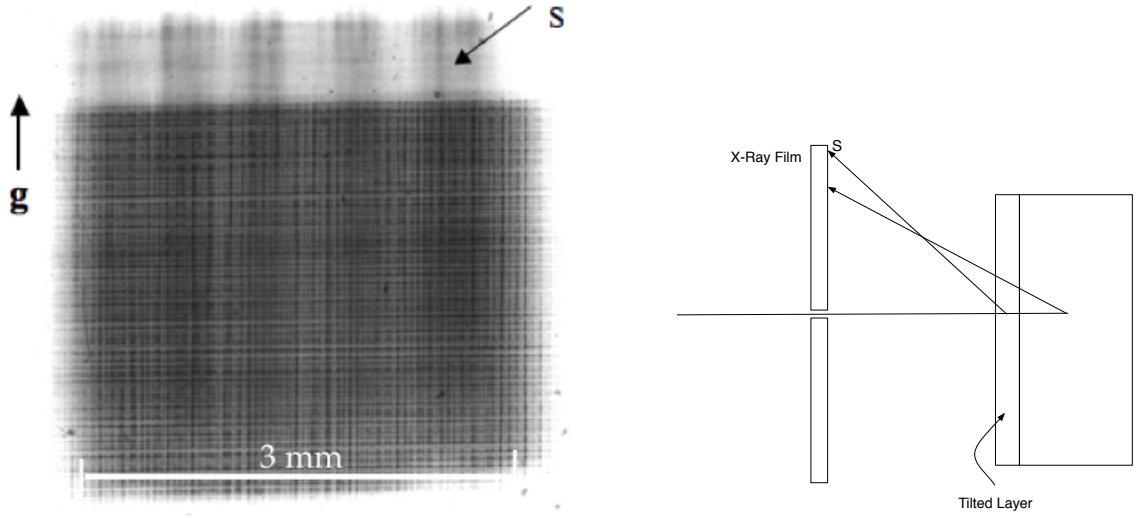

(a) Topograph (b) Schematic

Figure 4.8: a. 23% Ge Virtual Substrate, $1\bar{1}7$ Large area back reflection demonstrating lattice tilt in the SiGe virtual substrate (penetration depth of 37.41 μm). b. Schematic indicating the origin of the off-set image (S).

In addition to this, the topographs of the $Si_{0.70}Ge_{0.30}$ samples revealed evidence of lattice tilt, demonstrated by the presence of "wisps" in the direction of the diffraction vector in figure 4.9.

Topographs of all other samples showed no obvious evidence of lattice tilt (exemplified by figure 4.7a), suggesting tilt levels in all other samples are on the order of those measured in the $Si_{0.83}Ge_{0.17}$ samples. In order to test this hypothesis, lattice tilts of the silicon substrate and $Si_{1-x}Ge_x$ layers were measured in a $Si_{0.90}Ge_{0.10}$ and a $Si_{0.85}Ge_{0.15}$ sample. In the $Si_{0.90}Ge_{0.10}$ sample, the silicon substrate and $Si_{1-x}Ge_x$ layer demonstrated tilts of 0.0064° and 0.009°, respectively. Within the $Si_{0.85}Ge_{0.15}$ sample the tilts were 0.0085° and 0.004°. These minimal tilt magnitudes support the lack of observable tilt effects in the topographs.

Stacking Faults

Figure 4.9 shows a large area 206 back reflection topograph of the $Si_{0.7}Ge_{0.3}$ virtual substrate sample with a 12 nm ε-Si epilayer. This topograph demonstrates box-like structures which are indicative of stacking faults, bounded by 60° mixed misfit dislocations. These structures were also observed in the 9 nm ε-Si sample grown on a similar VS. As pointed out in chapter 1.1, extended stacking faults occur in tensile strained material, i.e. these stacking faults exist in the ε-Si layer rather than the SiGe buffer.

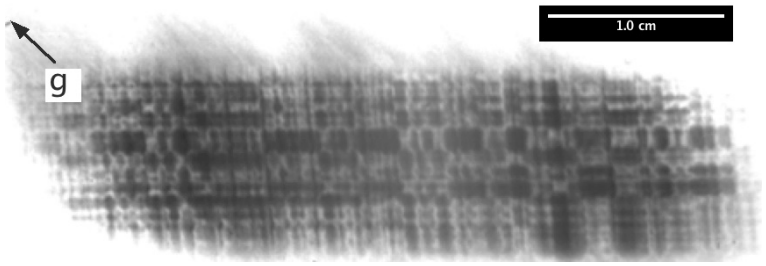

Figure 4.9: Large area 206 back reflection topograph of the $Si_{0.7}Ge_{0.3}$ virtual substrate with a 12 nm strained silicon epilayer. The projection of the diffraction vector **g** onto the plane of the recording film is also indicated.

Within the 1.26% ($Si_{0.70}Ge_{0.30}$) strained $\varepsilon - Si$ layer, the theoretical critical thickness is 13.37 nm. This value is based on an initial absence of in-grown threading dislocations, and the activation energy of the 60° mixed misfit dislocation. As pointed out in chapter 1.1 the activation energy of a misfit dislocation is reduced if it dissociates into a leading 90° partial dislocation and a trailing 30° annihilating partial dislocation. The observation of the stacking faults in this sample indicates the activation of at least the 90° partial dislocation, however it is unclear whether the critical thickness of the 30° counterpart is reached.

Chapter 1.1 describes the formation of the stacking fault upon activation of the 90° partial.

Subsequent to this (but prior to the formation of the 30° partial), the stacking fault extends with the dislocation under the formative force. Upon reaching an orthogonal dislocation, assuming insufficient excess strain energy, the dislocation becomes blocked. The orthogonal misfit dislocations thus bound each stacking fault resulting in the intensity distribution of figure 4.9.

Once the 90° partial has been blocked its strain relieving potential is removed. If the layer continues to grow and build strain energy, the possibility exists for the formation of the 30° annihilating partial, however the images collected offer no conclusive evidence of this formation.

4.6 Conclusions

SXRT analysis of the ε-Si samples of this project have elucidated the nature of the strain relieving misfit dislocations, lattice tilt and stacking faults.

Although HR-XRD investigations quantified the strain in the measured samples they gave no insight into the mechanisms of strain relaxation. The synchrotron x-ray topographs presented in this chapter have revealed the strain relaxing misfit dislocations associated with the relaxed SiGe buffer in all strained samples.

The emergence of lattice tilt appears to be the result of pre-existing lattice miscuts in the substrates. While the relaxation of strain reduces the magnitude of the tilt, it appears that it is not the precursor despite the fact that the largest tilts were measured in the highest strained samples.

Within the ε-Si layer, as the critical thickness is approached, stacking faults emerge as the dislocations dissociate under the tensile stress. The box-like shape of these stacking faults

suggests blocking interactions between the orthogonal dislocations thus limiting the levels of relaxation within the layer.

Chapter 5

Raman Spectroscopy

5.1 Introduction

Light scattering is the process by which light is redirected by an inhomogeneity in its path, in the case of the current discussion the inhomogeneity is the sample under test (crystalline Si). Upon interaction with matter, the electric field of the incident electromagnetic (EM) wave periodically alters the electron orbits of the molecules. This periodic perturbation results in the production of an induced dipole moment which manifests itself as the source of an EM wave of the same frequency as the incident light (ν_0).

In situations where the scattering molecules are themselves subject to vibrations, the scattered light may emerge with a frequency other than that of the incident light. These processes are known as inelastic scattering processes and Raman scattering is one such process. In Raman scattering, internal lattice vibrations produce atomic displacements which alter the periodic potential which acts on the electrons, thus facilitating an electron-lattice interaction energy. As energy is passed from electron to lattice (or vice-versa), quanta of vibrational

energy (phonons) are created or destroyed within the material and light is scattered with frequencies equally spaced above and below ν_0; $\nu_0 + \nu_{vib}$ (anti-Stokes) and $\nu_0 - \nu_{vib}$ (Stokes), where ν_{vib} is the excitation frequency of the quantized lattice vibration.

5.2 Historical Background

Raman scattering was first hypothesized by an Austrian physicist, Adolf Smekal in 1923 [91]. In 1928 Chandrasekhara Raman, an Indian physicist made the first experimental observation of the phenomenon which now carries his name, for this he was awarded the Nobel prize in physics in 1930 [92]. Historically Raman instruments utilized a Mercury-lamp as a light source and a photographic plate as a detector. It was not until the 1960's with the advent of the laser that Raman spectroscopy found widespread acceptance as a characterisation tool [93].

Initially Raman spectroscopy was used as a complementary technique to infrared spectroscopy in the investigation of chemical composition and crystallinity [94], however in 1970 Raman scattering's sensitivity to stress was reported by Anastassakis *et al.* [95] and since then, the technique has been used increasingly as a stress sensor.

The technique is especially useful when used in the μ-Raman configuration which allows spatial resolutions of $\sim 0.6\ \mu m$ (this is important as the measured stress is averaged over the probed volume). A further advantage of μ-Raman spectroscopy is its depth profiling capability via the use of different wavelength probe laser, due to the wavelength dependence of absorption coefficient and therefore penetration depth [96].

5.3 Theory

Lattice Vibrations and Phonons

Due to the periodic nature of the crystal lattice, an array of possible vibrational modes exist, these vibrations involve the entire lattice and are thus known as lattice vibrations. A subset of these lattice vibrations are phonons, which are energy-quantized standing waves. As will be demonstrated, phonons are of particular interest in Raman spectroscopy due the effects of wave vector conservation and the nature of the dispersion curve.

In order to identify the various lattice waves, an indexing scheme was required and to this end the concept of normal modes of vibration was introduced. The normal modes of vibration are indexed in accordance with the vibration's polarization. In a cubic crystal these normal modes are the longitudinal optical, the longitudinal acoustic, the transverse optical and the transverse acoustic. The optical and acoustic notation relates to the category of excitation frequency to which the mode is sensitive, and since Raman spectroscopy is an optical process only the optical branches are of concern here (the acoustic branches contribute to Brillouin scattering). In order for these normal modes to be fully defined, the crystal surface from which they are being observed must be known, for example, for back reflection from a (001) surface, there are two transverse directions: [100] and [010], and one longitudinal direction: [001]. In general, lattice vibrations are neither purely longitudinal nor transverse, however these general vibrations resolve themselves into normal mode vibrations, and as such can be described in terms of weighted combinations of same.

Lattice vibrations are modelled as waves propagating through the lattice with angular frequency ω ($\omega = 2\pi\nu$, where ν is the frequency) and wave vector k ($k = 2\pi/\lambda$, where λ is the wavelength) [97]. The relationship between ω and k is known as the dispersion relation, and plotting this relationship across the first Brillouin zone ($k = 0 - 2\pi/a$, where a is the silicon

lattice constant) gives the dispersion curve. Figure 5.1 [98], shows an example of the dispersion curve for silicon in the equivalent ⟨001⟩ directions. Raman scattering processes can be shown to be localized to the k = 0 region of the dispersion curve through the constraints of wave vector conservation, which will be outlined in the next section.

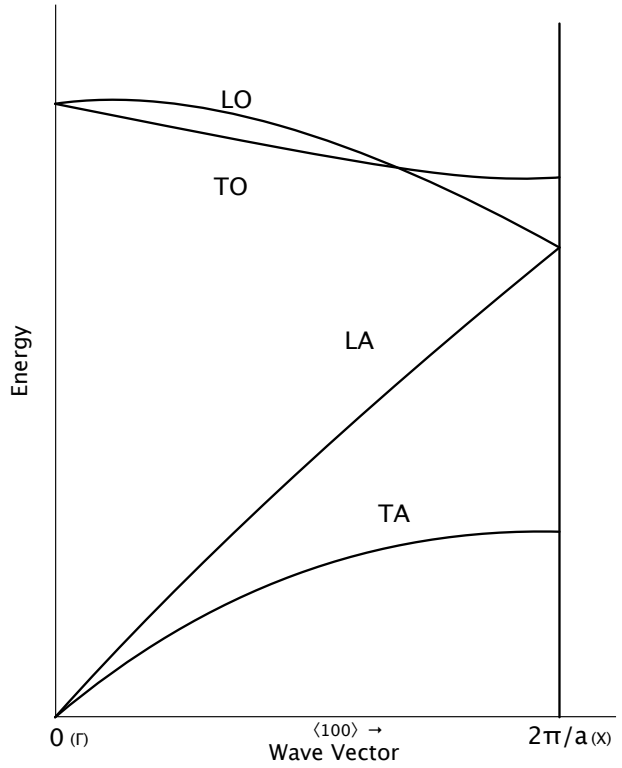

Figure 5.1: Silicon dispersion curve for the equivalent ⟨100⟩ directions [96].

Wave Vector Conservation and Breakdown

In lattice dynamics, 'wave vector conservation' is a more technically correct title for 'momentum conservation'. Lattice vibrations do not possess momentum (except at k = 0 which corresponds to a uniform displacement of the crystal) as the vibrational coordinates, in general, involve relative atomic coordinates. This not withstanding, lattice vibrations interact with particles such as electrons, neutrons and photons as though they possessed a momen-

tum $\hbar k$ ($\hbar = h/2\pi$, where $h = 6.626068 \times 10^{-34}\ m^2kg/s$, Planck's constant), sometimes called the crystal momentum [77]. In a phonon excitation in which the wave vector is conserved, there will be a transfer of momentum equal to $\hbar k$ from the exciting radiation to the crystal, where $k = k_i - k_s$, (k_i is the wave vector of the incident radiation and k_s is that of the scattered radiation) [99]. In order to fully determine the magnitude and direction of k, the experimental configuration must be taken into account. As can be seen from figure 5.2, the maximum k magnitude occurs at $\theta = 180°$ (back reflection) and this corresponds to a scattering wave vector given by,

$$|k_{\max}| = \left[\eta\left(\omega_i\right)\omega_i + \eta\left(\omega_s\right)\omega_s\right]\left(1/c\right) \tag{5.1}$$

where $\eta\left(\omega_i\right)$ and $\eta\left(\omega_s\right)$ are the refractive indices at the incident and scattered frequencies. For a typical Raman experimental set up, this value is of the order of $10^{-6}\ cm^{-1}$ [99]. This value is orders of magnitude smaller than the Bruillouin zone magnitude for typical crystals ($1.1 \times 10^8\ cm^{-1}$ for silicon) and as such Raman investigations are limited to excitations where $k \approx 0$ if wave vector conservation is to be upheld [99].

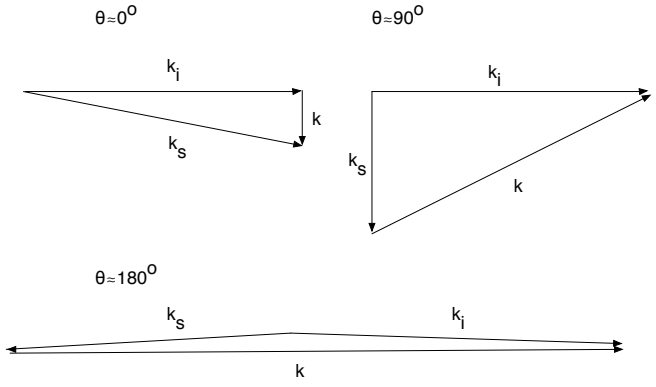

Figure 5.2: Demonstration of the wave vector magnitudes for different experimental configurations [99].

In the absence of translational symmetry, wave vectors are not good quantum numbers for labelling modes [77]. This implies that wave vector conservation will break down locally in the vicinity of a defect as this represents a disruption in the translational symmetry of the lattice. The validity of (5.1) therefore breaks down and excitations with a range of wave vectors, Δk contribute to the Raman scattering. Δk under these conditions is defined by the phonon correlation length (average crystallite size) L, and is given by $\Delta k = 2\pi L$.

Wave vector conservation also breaks down in the presence of high optical absorption. This is due to the fact that in absorbing media, the refractive index of the medium becomes complex, i.e. $\eta(\omega_i)$ and $\eta(\omega_s)$ become complex. This results in complex wave vectors k_i and k_s where the imaginary parts are given by $Im(k_{i,s}) = \omega_{i,s} K(\omega_{i,s})/c$ and $K(\omega_i)$, and $K(\omega_s)$ are the extinction coefficients at the incident and scattered frequencies. In materials with translational symmetry, the scattering wave vector is a continuous, real variable, therefore in the presence of high levels of optical absorption, equation \eqref{eqnRamanScatteringWavevectorMax} cannot be fully satisfied. The range of wave vectors allowable through conservation breakdown of this type is given by $\Delta k = Im(k_i) + Im(k_s)$ [99].

Classical Theory of Raman Spectroscopy

The classical origins of Raman scattered light are most easily demonstrated through the mathematical superposition of the sinusoidally varying dipole moment and lattice vibration. Light incident on matter induces a dipole moment between the positive and negative charge centers in the molecule given by,

$$\mu_{ind} = \alpha E \tag{5.2}$$

where α is the molecule's polarizability and E is the electric field of the incident radiation. As

the incident electric field is sinusoidally varying, the induced dipole moment varies similarly,

$$\mu_{ind} = \alpha E_0 cos\left(2\pi\nu_0 t\right) \tag{5.3}$$

where E_0 is the amplitude of the incident electric field, ν_0 is the frequency of the incident electric field and t is time. Oscillating dipole moments manifest themselves as sources of radiation of similar frequency, and so originates the elastic scattered (Rayleigh scattered) component of the Raman spectrum [94].

Raman scattered light arises if the scattering material is subject to internal vibrations. These internal vibrations change the size and shape of the molecule and therefore may change the crystal's polarizability. This change in polarizability is due to the fact that the ability of the incident electric field to perturbate the charge centers is dependent on the relative position of the atoms within the molecule. The relative displacement of the atoms due to a sinusoidal lattice vibration is given by,

$$dQ = Q_0 cos\left(2\pi\nu_{vib} t\right) \tag{5.4}$$

where Q_0 is the maximum atomic displacement along the normal co-ordinate relative to the equilibrium position, and ν_{vib} is the lattice vibration frequency. Under the assumption that $|\delta Q| << |Q|$ the polarizability of the molecule can be expressed as a truncated Taylor series expansion,

$$\alpha = \alpha_0 + \left({}^{\delta\alpha}/_{\delta Q}\right) dQ \tag{5.5}$$

where α_0 is the polarizability at equilibrium. Substituting the expression for the vibrational displacement from (5.4) gives,

$$\alpha = \alpha_0 + \left({}^{\delta\alpha}/_{\delta Q}\right) Q_0 cos\left(2\pi\nu_{vib} t\right) \tag{5.6}$$

Substituting this expression for α into (5.3) gives an expression for the induced dipole mo-

ment in a scattering material subject to internal vibrations,

$$\mu_{ind} = \alpha_0 E_0 cos\left(2\pi\nu_0 t\right) + \left({}^{\delta\alpha}/_{\delta Q}\right)_0 Q_0 E_0 cos\left(2\pi\nu_0 t\right) cos\left(2\pi\nu_{vib} t\right) \tag{5.7}$$

Using the trigonometric identity, $\cos(\alpha)\cos(\beta) = \frac{1}{2}(\cos(\alpha+\beta) + \cos(\alpha-\beta))$, this equation becomes,

$$\mu_{ind} = \alpha_0 E_0 cos\left(2\pi\nu_0 t\right) + \frac{1}{2}\left({}^{\delta\alpha}/_{\delta Q}\right)_0 Q_0 E_0 \left\{cos\left[2\pi\left(\nu_0 - \nu_{vib}\right)t\right] + cos\left[2\pi\left(\nu_0 + \nu_{vib}\right)t\right]\right\} \tag{5.8}$$

Inspection of this expression reveals the possibility of scattered light at three different frequencies. The additional spectral components are referred to as the Stoke's line $(\nu_0 - \nu_{vib})$ and anit-Stokes line $(\nu_0 + \nu_{vib})$, the elastically scattered light is generally called Rayleigh scattering. Equation (5.8) has further significance in that it reveals the necessity for a non-zero $\left({}^{\delta\alpha_{i,j}}/_{\delta Q}\right)_0$ term in order to facilitate Raman scattering. This implies that only lattice vibrations which cause a change in the molecule's polarizability are Raman active.

Quantum Theory of Raman Spectroscopy

The arguments presented thus far provide a classical understanding of the origin of Raman scattered light, however, the classical framework by definition, takes no account of the quantization of vibrational energy bands within the lattice. As this quantization has far reaching implications for the interpretation of Raman data, it is also necessary to have a quantum mechanical understanding of the process.

Figure 5.3 exemplifies a typical Morse curve for a ground electronic state of a molecule, relating the interatomic separation to the energy of the molecule. Within the envelope of this electronic state, only energy bands manifesting the quantized vibrational (vibronic) and rotational energy levels are allowed (in the current discussion only the vibronic energies are

considered). The energy separations between these vibrational bands are key to interpreting Raman data.

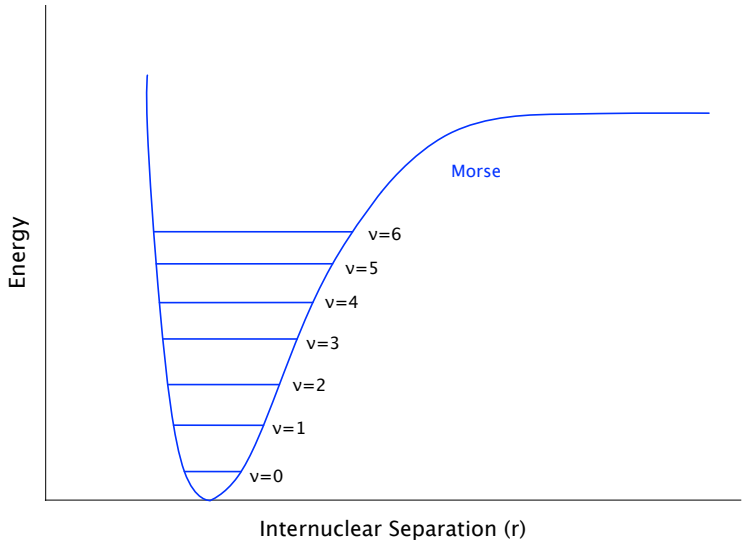

Figure 5.3: Typical Morse curve of a ground electronic state relating interatomic separation to molecular energy. Also shown are the quantized vibrational states within this energy band.

The shape of the Morse curve introduces complexity to the system. As the interatomic separation in this hypothetical molecule increases towards infinity, the energy of the molecule essentially levels out due to decreasing (and ultimately negligible) interatomic influence. This decreasing influence introduces increasing anharmonicity into the higher energy vibrational states making the analysis of vibronic levels within the Morse curve difficult. However appropriate simplification is possible.

At a given temperature, for a collection of molecules, the relative population of each vibrational energy level is determined by Boltzmann's equation [77],

$$\frac{N_n}{N_m} = \frac{g_n}{g_m} \exp\left[\frac{-(E_n - E_m)}{kT}\right] \tag{5.9}$$

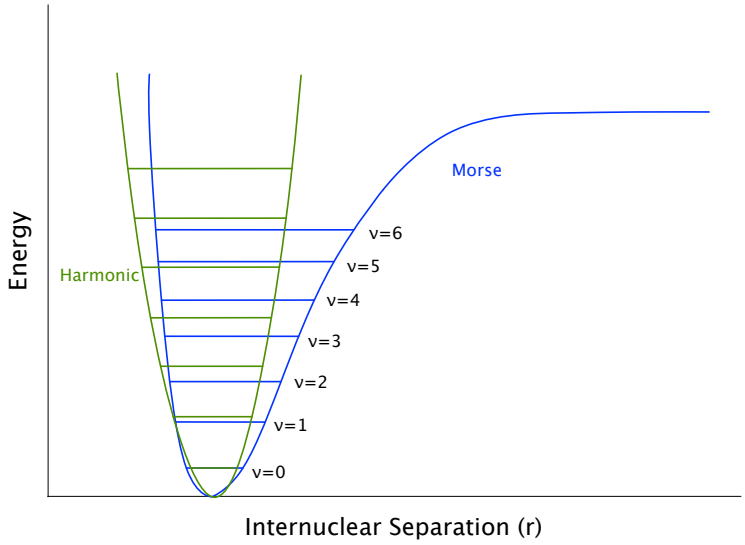

Figure 5.4: Typical Morse curve and harmonic approximation of a ground electronic state relating interatomic separation to molecular energy.

where N_n and N_m are the number of molecules in the excited state (n) and in the ground state (m) respectively, g is the degeneracy of the respective levels, $E_n - E_m$ is the energy difference between the vibrational energy levels and k is Boltzmann's constant ($1.3807 \times 10^{-23} JK^{-1}$). At low to moderate temperatures the ground state dominates this distribution. Due to the fact that in a Raman scattering event, a change of more than one quantum occurs only in very rare circumstances [100], the region of most interest within the Morse curve is that closest to the bond length, i.e. low energy. In this region the shape of the Morse curve is least effected by anharmonicity and as such, the energy distribution of the system can be approximated to resemble that of a simple harmonic oscillator (SHO) shown in figure 5.4.

Under the assumption of harmonic oscillation the quantized energy levels are given by,

$$E_n = \left(n + \frac{1}{2}\right) h\nu_{vib} \tag{5.10}$$

where n is the vibrational quantum number ($n = 0, 1, 2, \dots$) and h and ν_{vib} are as previously defined. Under the SHO model the frequency of vibration for all energy levels remains constant, although the wavefunction ($\Psi_n(x)$) and therefore the probability of finding an

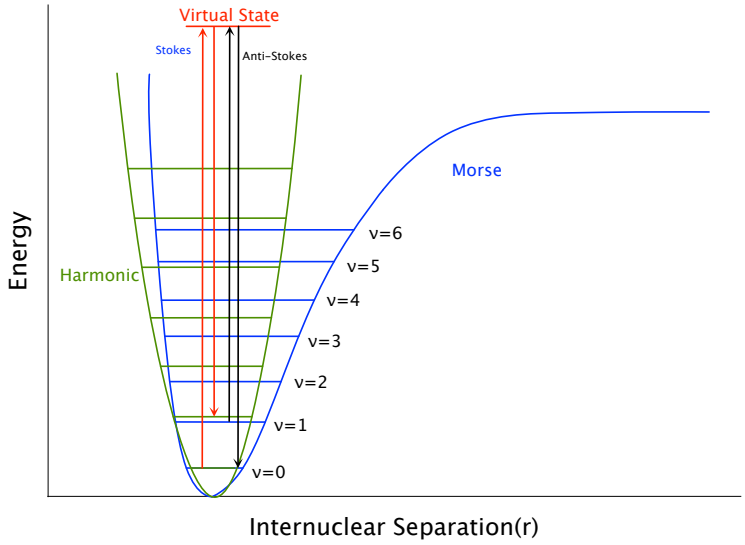

Figure 5.5: Typical Morse curve and harmonic approximation of a ground electronic state relating interatomic separation to molecular energy. Also shown are the mechanisms of Stokes and anti-Stokes scattering.

atom at a given distance from the equilibrium position $(|\Psi_n(x)|^2)$changes with n.

The perturbation of the charge centers by EM radiation excites the molecule into a short-lived virtual state. The energy of this state is, in general (depending on the energy of the incident radiation), much larger than that of the molecule's vibrational energy quantum. Upon photon emission, the system relaxes to one of three states; it returns to its initial state or it relaxes to a state vibrationally excited or relaxed relative to its initial state. In the Stokes scattering process described in figure 5.5 the scattered light energy is given by, $E = h(\nu_0 - \nu_{vib})$. Anti-Stokes scattering can be explained in a similar fashion with the initial molecular vibrational energy being ν_1 and the final energy being ν_0, i.e. the lattice relaxes to the ground vibrational state and in the process of doing so, donates a quantum of energy to the interacting EM radiation, resulting in scattered light with energy $E = h(\nu_0 + \nu_{vib})$. The relative population of the initial states dictate that Stokes scattering is the more common Raman event.

Raman Sensitivity to Stress

The frequency of the Raman shift is a function of the elastic constants of the material in question. As stress alters these constants, this implies a Raman strain sensitivity. One of the first theoretical treatments of this sensitivity was put forward by Ganesan *et al.* [101]. This work showed that for stresses in the crystal frame of reference i.e. {100} for silicon, the frequencies of the three optical modes in the presence of stress are given by

$$\Delta\omega_j = \omega_j - \omega_{j0} \approx \frac{\lambda_j}{2\omega_{j0}} \tag{5.11}$$

where ω_{j0} is the Raman frequency shift is the absence of stress and λ_j (j = 1,2,3) are the eigenvalues of the characteristic equation,

$$\begin{vmatrix} p\varepsilon_{11} + q\left(\varepsilon_{22}+\varepsilon_{33}\right) - \lambda & 2r\varepsilon_{12} & 2r\varepsilon_{13} \\ 2r\varepsilon_{12} & p\varepsilon_{22} + q\left(\varepsilon_{33}+\varepsilon_{11}\right) - \lambda & 2r\varepsilon_{23} \\ 2r\varepsilon_{13} & 2r\varepsilon_{23} & p\varepsilon_{33} + q\left(\varepsilon_{11}+\varepsilon_{22}\right) - \lambda \end{vmatrix} = 0 \tag{5.12}$$

where p, q, r are the phonon deformation potentials, $\varepsilon_{i,j}$ are the strain tensor components.

The strain tensor components are calculated by applying Hooke's Law, e.g. for a uniaxial stress in the [100] direction,

$$\begin{aligned} \varepsilon_{11} &= S_{11}\sigma \\ \varepsilon_{22} &= S_{12}\sigma \\ \varepsilon_{33} &= S_{12}\sigma \end{aligned} \tag{5.13}$$

$$\tag{5.14}$$

The Raman tensors for the three active optical modes in silicon are thus given by [102],

$$R_x = \begin{pmatrix} 0 & 0 & 0 \\ 0 & 0 & a \\ 0 & a & 0 \end{pmatrix}, R_y = \begin{pmatrix} 0 & 0 & a \\ 0 & 0 & 0 \\ a & 0 & 0 \end{pmatrix}, R_z = \begin{pmatrix} 0 & a & 0 \\ a & 0 & 0 \\ 0 & 0 & 0 \end{pmatrix} \tag{5.15}$$

Thus polarization selection (through (5.16) [102] results in observation of only $\Delta\omega_3$ in back scattering configuration from a (001) surface.

$$I_k = \Xi \left| p'^T \Delta_k p \right|^2 I_0 \tag{5.16}$$

where I_k and I_0 are the scattered and incident intensities, p' and p are the scattered and incident polarization vectors, R_j is the Raman tensor of the j^{th} mode and Ξ is a constant related to the Raman scattering cross-section.

Thereby the observed Raman shift due to a biaxial strain in the in-plane $\langle 100 \rangle$ directions is given by,

$$\Delta\omega_3 = \frac{1}{2\omega_0} \left[pS_{12} + q \left(S_{11} + S_{12} \right) \right] \left(\sigma_{xx} + \sigma_{yy} \right) \tag{5.17}$$

Inserting the experimental values, $S_{11} = 7.68 \times 10^{-2} Pa^{-1}$, $S_{12} = -2.14 \times 10^{-12} Pa^{-1}$, $S_{44} = 12.7 \times 10^{-12} Pa^{-1}$, p = -1.43 ω_0^2, q = -1.89 ω_0^2 and r = -0.59 ω_0^2, the numerical value for $\Delta\omega_3$ in the presence of biaxial stress becomes [102],

$$\Delta\omega_3 \left(cm^{-1} \right) = -4 \times 10^{-9} \left(\frac{\sigma_{xx} + \sigma_{yy}}{2} \right) [Pa] \tag{5.18}$$

Raman Sensitivity to Carrier Density

Raman spectroscopy's sensitivity to carrier density, and more specifically in this case, to electron density, is rooted in the carrier contribution to the free energy of the crystal. In chapter 1.1 it was demonstrated that the energy of carriers is a function of strain. In 1961 Keyes argued that this implies a relationship between the strain energy (and therefore the elastic constants (ultimately the C_{44} elastic constant) of the crystal and the energy of carriers [103]. The full demonstration of this dependence can be found in [103] however, in essence, this work put forward that the strain induced reduction in the carrier energy resulted in a

concomitant reduction in the free energy of the crystal which is reflected in the C_{44} elastic constant.

Cerdeira *et al.* [104] applied Keyes's rationale to the interpretation of experimentally observed carrier density related Raman shifts in degenerately doped germanium and silicon. In order to account for the uniaxial strain of Keyes's theory, Cerdeira proposed that an optical phonon of sufficiently long wavelength would act in a manner similar to a shear applied stress. The uniaxial stress envisioned by Cerdeira thus resulted from the long wavelength [100] Raman active modes, which, when combined, have the symmetry of a [111] uniaxial stress. The oscillatory nature of this stress makes the process respondent to carrier relaxation times (carriers must relax to thermal equilibrium within one period of the oscillation for the effect to be observable). In the case of silicon, incomplete relaxation manifests itself as a peak-broadening term in the Raman spectrum, whereas the longer electron relaxation times in n-germanium, result in an elimination of the effect entirely [104].

Figure 5.6 compares the orientation of the [111] uniaxial stress and the silicon conduction band minima. An inspection of this figure reveals that all valleys are equivalent with respect to the [111] stress. This means that unlike the case of biaxial tensile strain considered elsewhere in this work, none of the [100] valleys are preferentially occupied.

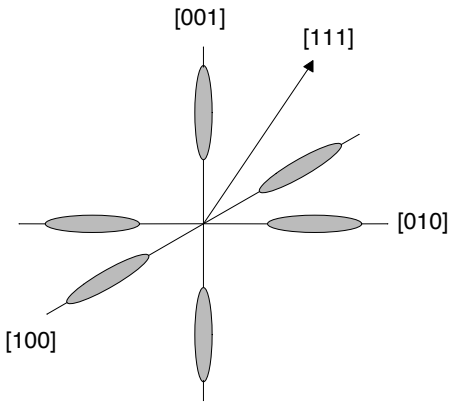

Figure 5.6: Schematic diagram of silicon conduction band minima and [111] orientated uniaxial strain. The strain affects all minima equally and causes no preferential occupation of out-of-plane valleys.

The reduction in the chemical potential in this case results from a splitting of the two-fold sub-band degeneracy at the X point in the Brillouin zone [105], demonstrated in figure 5.7 [106] brought on by the shear [111] uniaxial strain.

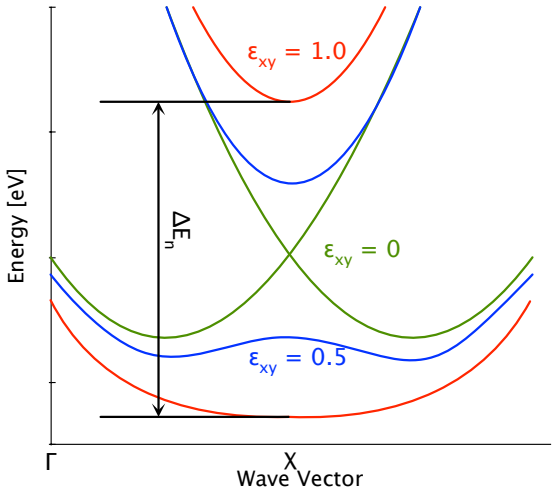

Figure 5.7: Reproduction of two-band k.p data showing an increasing energy gap at the X-point Brillouin zone edge for increasing shear strain (ε_{xy}) [106].

This splitting results in a uniform reduction of the energy of all conduction band valleys given by [106],

$$\Delta E_n\left(\varepsilon_{xy}\right) = -\frac{\pi^2 n^2}{2m_l t^2}\frac{\left(D\varepsilon_{xy}m_l\right)^2}{\hbar^2 k_0^4\left|1-\left(\pi n/k_0 t\right)^2\right|} \tag{5.19}$$

where D is the shear strain deformation potential, k_0 is the position of the valley minimum relative to the X-point in unstrained Si and all other terms are as previously defined. Figure 5.7 demonstrates the effects of increasing shear strain on the sub-band structure at the [001] X-point in the Brillouin zone.

In the previous section, the solution to equation (5.12) is used to define the Raman shift as a function of the phonon deformation potentials, elastic stiffness tensor elements and the strain tensor elements. The strain tensor elements of equation (5.12) are defined along the major axes of the crystal, thus allowing investigation of strains in these directions. In order for a similar equation to be derived for a [111] strain, equation (5.12) must be rotated to a new frame of reference in which the strain tensor elements lie in the $\langle 111\rangle$ directions [107]. Performing this rotation results in the following expression for $\Delta\omega_3$ [108],

$$\begin{aligned}
\Delta\omega_3 &= \frac{\lambda_3}{2\omega_0} = \frac{1}{2\omega_0}\left[\left(p+2q\right)\varepsilon_{xx} + 4r\varepsilon_{xy}\right] \qquad (5.20)\\
\text{where, } \varepsilon_{xx} &= \left[4\varepsilon_{||} + 2\left(-2\varepsilon_{||}\left[\frac{C_{11}+2C_{12}-2C_{44}}{C_{11}+2C_{12}+4C_{44}}\right]\right)\right]/6\\
\varepsilon_{xy} &= \left[-\varepsilon_{||} + 2\left(-2\varepsilon_{||}\left[\frac{C_{11}+2C_{12}-2C_{44}}{C_{11}+2C_{12}+4C_{44}}\right]\right)\right]/3
\end{aligned}$$

This is a much more complicated relationship, however in the present context, the important outcome is the introduction of a C_{44} dependence in $\Delta\omega_3$. Thus the measurement of the Raman shift in the absence of an applied stress, incorporates this internal oscillating [111] stress, the result of which is a sensitivity to free carrier density. This is due to the C_{44} dependence on carrier density, specified subsequently in (5.29). The oscillating stress remains present after the application of an external stress, and so at sufficiently high carriers density,

additional shifts are expected in the spectra of both nominally unstrained and strained materials.

The discussion to this point has related carrier densities to changes in the elastic constants. Further details on the mechanism of electron-phonon interaction are given in the context of the experimental data to follow.

5.4 Raman Experimental Details

Raman Instrumentation

Raman measurements for this project were carried out on a LabRAM HR 800 system manufactured by Horiba Jobin Yvon. This is a dispersive Raman system allowing the use of multiple excitation wavelengths and a confocal microscope (thereby providing $\sim 1 \quad \mu m$ spatial resolution). The exciting radiation is provided by a 325 nm wavelength He-Cd laser, this allows the observation of Raman activity in the top $\sim$ 10 nm of the sample due to silicon's high absorption coefficient in this spectral region. Figure 5.8 is a schematic of the set up used here and explanations of the salient elements follow subsequently.

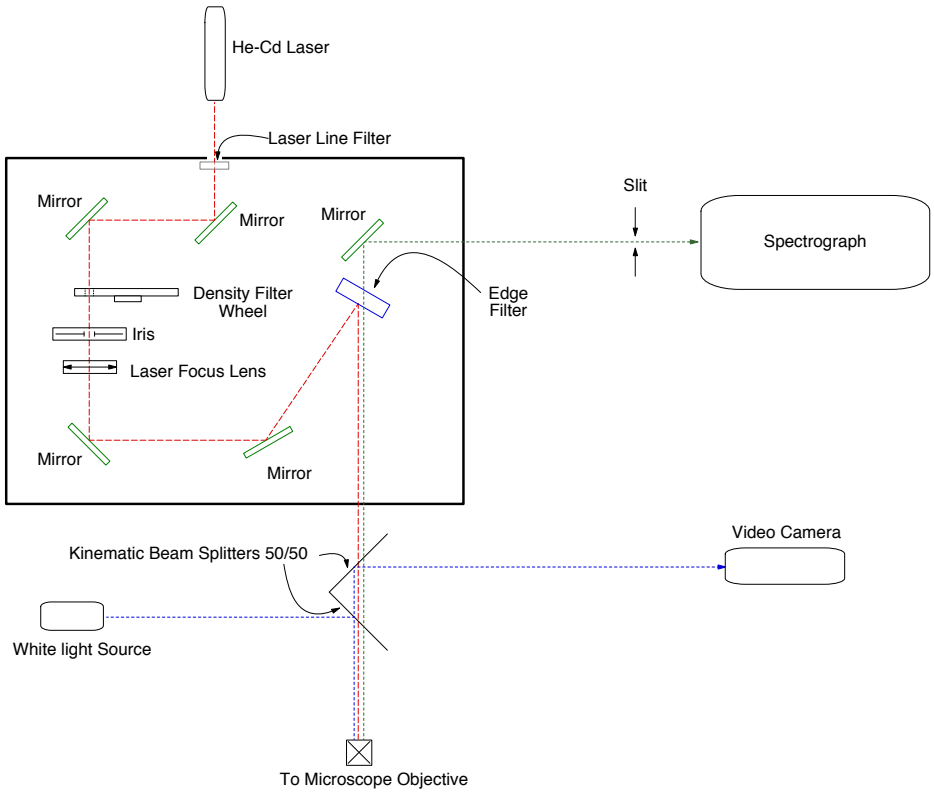

Figure 5.8: Schematic of the Horiba Jobin Yvon HR 800 system.

He-Cd Laser

A major advantage of Raman spectroscopy is its ability to provide depth profiles via variation of the excitation wavelength. The strained silicon layer, and implant depth in the samples under investigation in this project are on the order of $\sim$ 10 nm. In order to simplify the analysis of the results, the contribution from regions beyond this depth should be minimized, as such, the penetration depth of the laser to be used becomes a major consideration in the experimental design process. The laser employed is a 325 nm wavelength He-Cd laser. In order to establish the penetration depth of light at this wavelength, the practices of DeWolf are followed [107].

The total intensity of light scattered between the surface and a depth d within the sample is defined as,

$$I_s = I_0 R \int_0^d e^{-2\alpha x} dx = \frac{I_0 R}{2\alpha} \left(1 - e^{-2\alpha d}\right) \tag{5.21}$$

where I_0, R and α are the incident intensity, the Raman scattering cross section and the photo-absorption coefficient of silicon respectively. The penetration depth d_p is defined as the depth which satisfies the relationship,

$$I_d/(I_s + I_d) = 0.1 \tag{5.22}$$

With these definitions in place, the penetration depth is given by,

$$d_p = \frac{-\ln 0.1}{2\alpha} = \frac{2.3}{2\alpha} \tag{5.23}$$

Using this expression, and a silicon absorption coefficient of $1.225 \times 10^6\ cm^{-1}$ [109] the penetration depth of the 325 nm He-Cd laser is silicon is 9.3 nm.

Laser Line Filter

Although the output of the laser is considered to the monochromatic, characterized by a single sharp spectral peak, there can also be present, lower level transitions and plasma lines. Additionally the laser wavelength can shift due to power, temperature or pressure fluctuations. In order to account for these shifts and spectral contaminants a laser line filter is inserted in the beam path.

A laser line filter is a narrow band-pass filter. In the present work an Omega Optical 325 NB2 filter is used. This filter as a central wavelength of 325 +0.3/-0.2 nm, typical transmission of $\leq 25\%$ and a transmission FWHM of 2 ± 0.4 nm [110].

The inclusion of this filter is optional as the recording of plasma line positions and spectral shifts can be advantageous during the interpretation of Raman data, this is discussed in chapter 5.4.

Edge Filter

Incident on the detector are both the Rayleigh and Raman scattered light, with the Raman scattered component orders of magnitude smaller than that of the Rayleigh scatter. In order to analyze the Raman scattered light, the Rayleigh scattering must be rejected. To this end an edge filter is used. Edge filters, as the name suggests, are characterized by a steep drop-off in their transmission at the cut-on/cut-off wavelength. In their rejection spectral region they have extremely high reflectivity, allowing the incorporation of the edge filter as a "mirror" for the laser line in figure 5.8.

The edge filter used presently is the short-pass Omega Optical XE 325. This filter has a cut-on/cut-off wavelength of 227.5 nm. Wavelengths greater than this experience $> 85\%$ transmission while wavelengths less than this are subjected to attenuations of OD >5 [110].

Confocal Objective

The use of confocal objectives in Raman spectroscopy has become standard practice as they allow greater level of spatial resolution than typical wide-field applications. Confocal microscopy achieves this greater spatial resolution through the use of spatial filtering, thus selectively removing out-of-focus light. Figure 5.9 demonstrates this principle. This filtering of out-of-focus light provides control over the depth of field and eliminates information originating away from the focal plane. The objective lens used for the current experiments is an OFM® Near Ultraviolet (NUV) 40× lens and the confocal hole diameter is set to 200

μm.

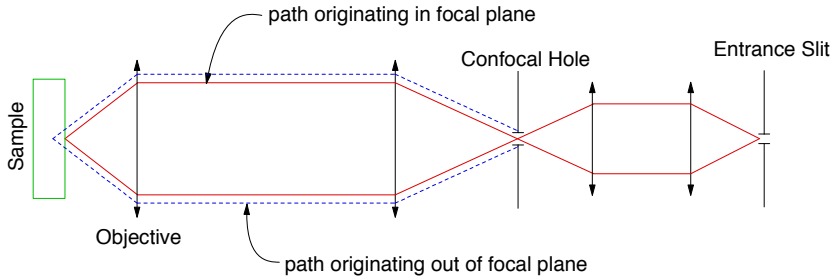

Figure 5.9: Schematic diagram illustrating the principle of confocal microscopy.

Spectrograph

Analysis of the Raman scattered light is carried out within the HR800 spectrograph (schematic of which is shown is figure 5.10). Divergent light incident through the entrance slits is collimated upon reflection from a spherical mirror with a focal length of 800 mm. This collimated light is then incident on a grating (in the current experiments an 2400 g/mm grating is used), which spatially separates the spectral components of the light. Detection is performed using a 1024×256 pixel CCD detector with a pixel width of 26 μm.

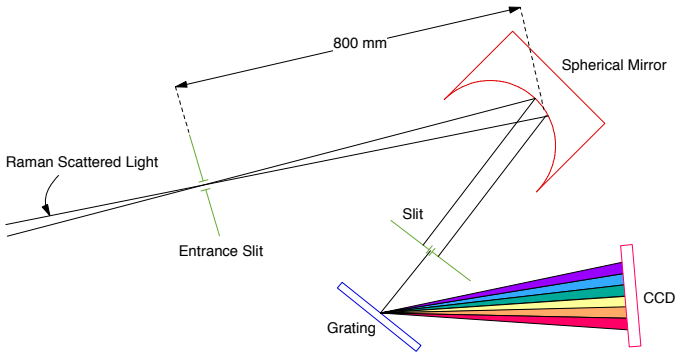

Figure 5.10: Schematic diagram of the HR800 spectrograph.

Due to the calibration process preceding each experimental session, and the relative nature of the measurements, the repeatability of measurements is more important than absolute accuracy. Under normal temperature conditions ($\pm 1°C$) the repeatability of measurements is defined by the dispersion of the system i.e. the wavenumber increment per CCD pixel. This value is a function of the wavelength of the incident light, the slit width, and the density of grooves and angles of incidence and diffraction on the grating. Figure 5.11 shows the dispersion as a function of wavelength for the 2400 g/mm grating, from this figure the dispersion can be seen to be $\sim 0.6\ cm^{-1}/pixel$ [111].

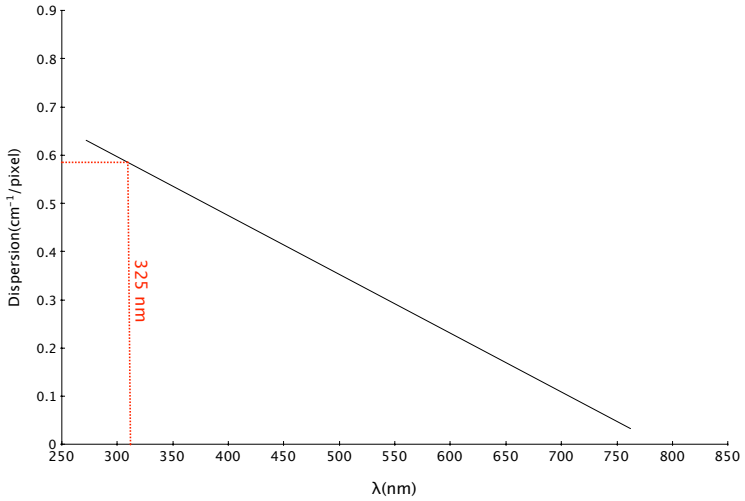

Figure 5.11: Dispersion as a function of wavelength for the 2400 g/mm grating.

Raman Data Processing

The results presented in the following section demonstrate μ-Raman's sensitivity to carrier density in addition to stress effects. The small magnitude of the shifts resulting from variation of the carrier concentration required additional procedural steps to be taken in order for them to be resolved.

Prior to measurement, the silicon Raman peak amplitude was normalized to that of the calibration peak by means of accumulation-time scaling. This minimized the impact of curve-fitting anomalies. Post-measurement, the peak positions were adjusted in accordance with the shifts of a reference spectral line, initially the 332-nm emission line from an external source was used [112], however, subsequent to a system upgrade, observation of inherent plasma lines became possible, allowing real-time observation of thermal drift effects.

These additional experimental steps resulted in a measurement repeatability on the order of 0.1 cm^1 [112].

5.5 Raman Results & Discussion

Initial μ-Raman measurements carried out during this project were aimed at characterizing the effects of sample processing on strain within the ε-Si layer. Anomalous Raman shifts subsequent to ion-implantation and annealing however, indicated that standard Raman interpretations would be insufficient for these samples. Figure 5.12 exemplifies these deficiencies, plotting the Raman and HR-XRD determined stresses across a sample set including a control (unprocessed) sample, an as-implanted sample and three annealed samples. The implant dose in this sample set was 6×10^{14} Sb cm^{-2} and the samples were of nominally $Si_{0.83}Ge_{0.17}$ VS. Much of the analysis to follow focuses on this data set as it demonstrates the highest levels of activation, however it is also representative of the other data set.

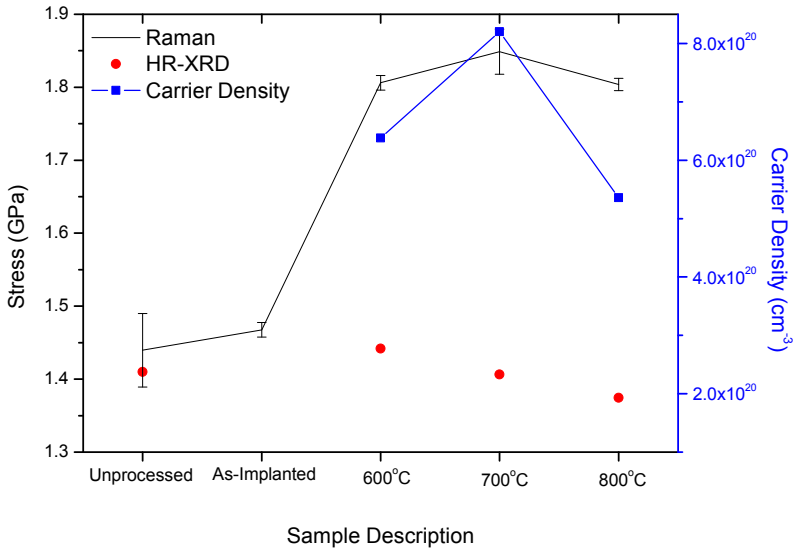

Figure 5.12: μ-Raman and HR-XRD determined stresses across the 6×10^{14} Sb cm^{-2} implanted $Si_{0.83}Ge_{0.17}$ samples.

Under traditional Raman interpretations figure 5.12 reveals additional stress components in all processed samples. Within the as-implanted sample the additional stress is relatively

small, $\sim$ 0.06 GPa, however upon subsequent anneal, the apparent increase in stress is significant, reaching $\sim$ 0.5 GPa at its peak. These data points however belie the true stress levels within the annealed samples, a fact indicated by their disparity with stresses calculated from HR-XRD measured strains. The trend similarity between the Raman shifts and the carrier concentrations (plotted on the secondary axis of figure 5.12) in the annealed samples is also significant.

The data set of figure 5.12 reveals the need for care and additional interpretive tools when dealing with Raman shifts originating in both as-implanted and degenerately doped samples. Following these observations, a survey of Raman response to these industrial processes was undertaken. The current section presents this survey and provides the additional theoretical considerations required for the interpretation of this data.

Strain Effects

Historically μ-Raman spectroscopy's stress sensitivity has been well documented [95], [102], [107]. In order authenticate this stress sensitivity, the μ-Raman measured stresses in the unprocessed samples are compared to stress levels calculated from pseudomorphic growth theory and HR-XRD strain data. Figure 5.13 shows the comparative plot.

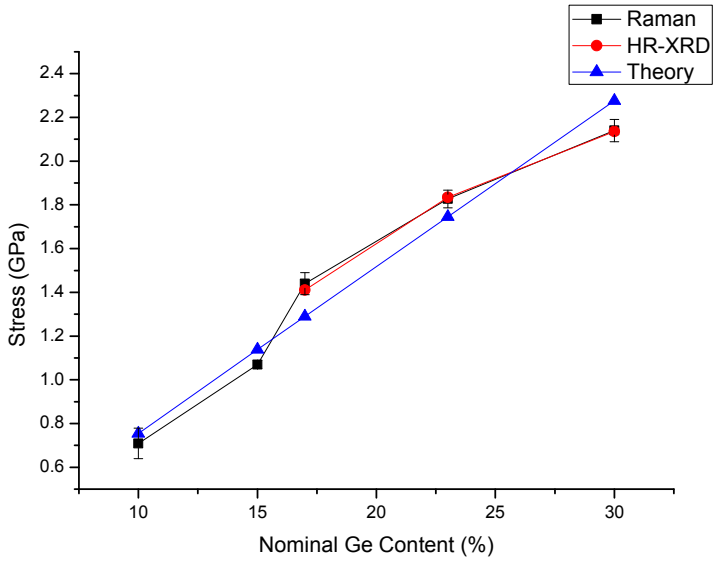

Figure 5.13: Measured stress (μ-Raman and HR-XRD) and theoretical maximum stress as a function of Ge virtual substrate content.

The Raman determined stresses of figure 5.13 were calculated using the equation [107]

$$\sigma_{xx} = \sigma_{yy} = \frac{-\Delta\omega_{Si_{UV}}}{4}[GPa] \tag{5.24}$$

where σ_{xx} and σ_{yy} are the stresses in the [100] and [010] directions, respectively and $\Delta\omega_{Si_{UV}}$ is the stress induced shift in the Raman peak position in cm^{-1}. The theoretical and HR-XRD stresses were calculated on the basis of the in-plane strains using the equation [113],

$$\sigma_{Si} = \frac{E_f m}{1-\nu}[GPa], \tag{5.25}$$

where E_f and ν are the Young's modulus and Poisson's ratio of the film, respectively and m is the in-plane strain. The theoretical calculations presume a fully relaxed virtual substrate and a fully strained ε-Si layer, as such, m represents the misfit between the SiGe lattice constant and that of bulk Si. The HR-XRD determined stress compares the measured in-plane lattice constant of the ε-Si layer to that of bulk Si.

As expected the data of figure 5.13 shows a high degree of correlation between the in-plane stresses determined by HR-XRD and Raman techniques thus confirming μ-Raman's suitability as a strain sensor capable of rapid investigations. The discrepancies between the measured and theoretical stresses in figure 5.13 can be explained through the variability of $Si_{1-x}Ge_x$ germanium content, as described in chapter 3.

Phonon Confinement and Residual Stress Effects

As μ-Raman spectroscopy is sensitive to the vibrational frequencies of molecules and phonons rather than the strain of crystalline materials, it can investigate materials and phases inaccessible to HR-XRD. The versatility of the technique is exemplified in the investigation of amorphous or radiation damaged materials. Raman spectroscopy has been shown to be a sensor for material crystallinity through observations of the Raman peak shape which is sensitive to the phonon coherence length.

The phonon coherence length (PCL) concept was introduced by Richter *et al.* [114] and was built upon by Campbell and Fauchet [115]. The phonon coherence model (PCM) is an expression of Heisenberg's uncertainty principle, stating that under conditions of spatial confinement, additional momentum components become accessible to optical scattering events. The Raman spectrum of a material demonstrating such confinement effects is thus characterized by the presence of a range of frequencies (each related through the dispersion curve to a particular scattering momentum) defined by the coherence length of the phonon, L. Due to the fall-off of the phonon dispersion curve in the vicinity of $k = 0$, the additional frequency components lie on the low energy side of the peak, thus giving rise to asymmetrical peak broadening. Additional to this is the introduction of peak position shifts due to residual stress introduced by the implantation process. The introduction of lattice damage also causes a reduction in the peak scattered intensity. Figure 5.14 demonstrates these effects,

comparing the Raman peak of a crystalline sample with that of an as-implanted sample.

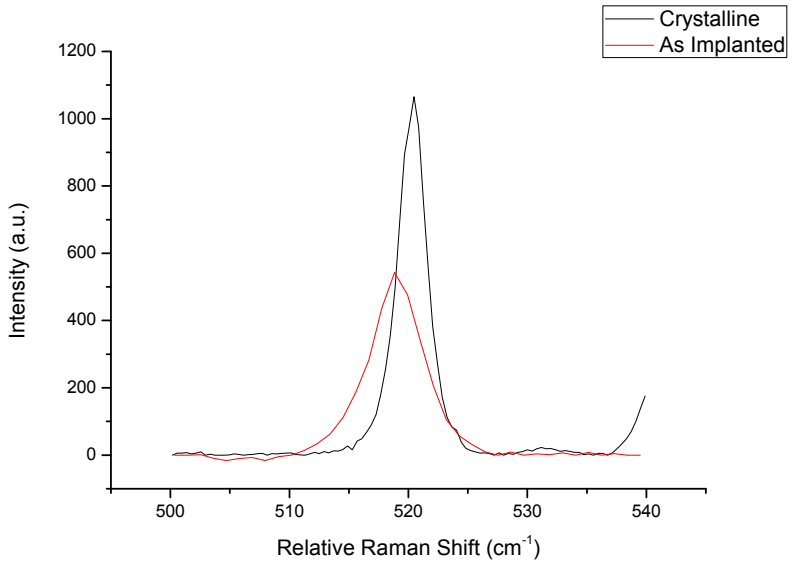

Figure 5.14: Expamles of μ-Raman spectra of crystalline and as-implanted silicon.

In order to analyze the as-implanted samples, the Raman peak shapes were fitted to Macia *et al.*'s reformulation of Richter, Campbell and Fauchet's model [116],

$$I(\omega) \propto \int_0^{q_0} \frac{\exp\left(-q^2L^2/8\right) 4\pi q^2 dq}{\left(\omega - \omega(q)\right)^2 + \left(\Gamma_0/2\right)^2} \tag{5.26}$$

where $q_0 = 2\pi/a$ (a is the silicon lattice constant), ω is the energy in wavenumbers, $\Delta\omega$ is the Raman shift originating from the residual stress and Γ_0 is the natural line width of the peak. $\omega(q)$ is the phonon dispersion curve expression approximated currently as [116],

$$\omega(q) = \omega_p - 120\left(\frac{q}{q_0}\right)^2 \tag{5.27}$$

The precise choice of numerator exponential in (5.26) is rather arbitrary, with Richter *et al.* originally using a value of e^{-1} and Campbell and Fauchet investigating a range of values. Of importance is that the choice is such that the amplitude of the phonon is zero at the extremities of the crystallite, as per Campbell and Fauchet's findings [115].

Equation 5.26 was used to estimate the phonon coherence lengths within the as-implanted samples by fitting it to scaled experimental data using L as the fitting constant and $\Delta\omega$ as a variable off-set for peak alignment. Figure 5.15 shows the resulting fits for as-implanted samples of varying implant dose.

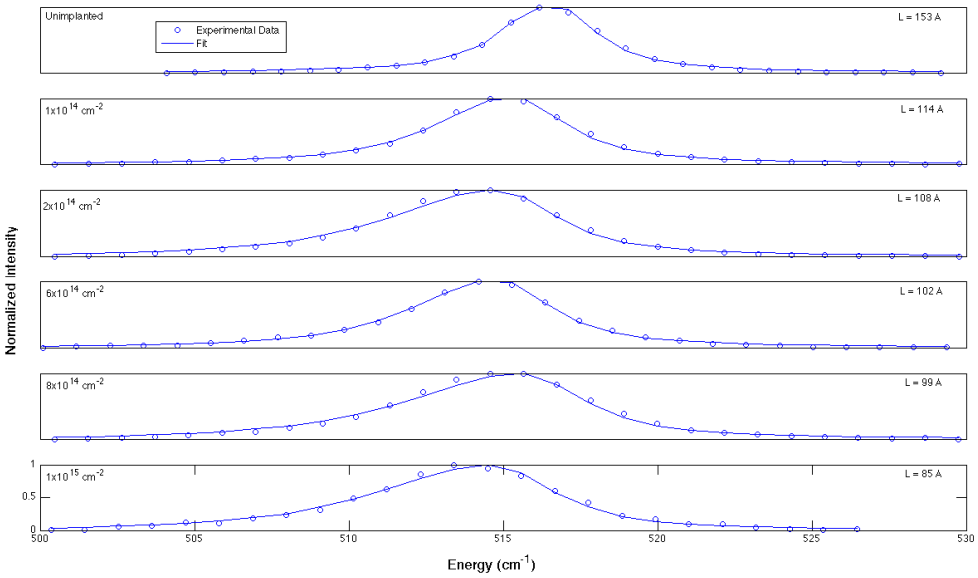

Figure 5.15: Experimental and fitted Raman peaks for as-implanted samples with varying implant dose. The samples were strained silicon on nominally $Si_{0.83}Ge_{0.17}$, however the variability in the substrate germanium content means the changes in $\Delta\omega$ cannot be entirely attributed to phonon confinement.

The plots of figure 5.15 again demonstrate the effects of variable $Si_{1-x}Ge_x$ content in the nominal $Si_{0.83}Ge_{0.17}$ samples with the first three peaks showing the predicted increasing red shift with implant dose only for the $6 \times 10^{14}\ cm^{-2}$ peak to shift in the opposite direction. This break in trend is due to a transition from $x = 0.15$ to $x = 0.181$. Setting aside the trends in Raman shift, the peak shape trends are in good agreement with those of the PCM, i.e. the asymmetric broadening concomitant with phonon spatial confinement increases with implant dose. Of additional note is the asymmetry of the unimplanted peak likely due to

phonon confinement at the ε-Si/ $Si_{0.83}Ge_{0.17}$ interface. Figure 5.16 quantifies the phonon coherence lengths extracted from these fits.

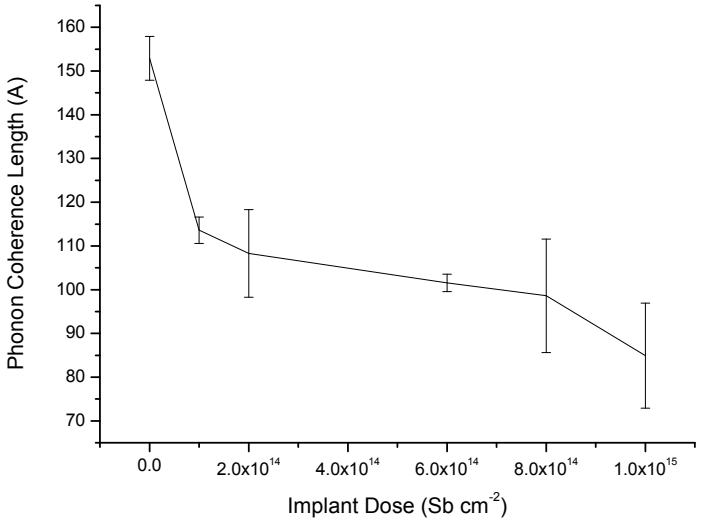

Figure 5.16: Phonon coherence lengths within as-implanted samples as a function Sb implant dose.

In the case of the unimplanted sample, the extracted coherence length aligns well with the thickness of the ε-Si layer (17.5 nm) however the interpretation of the subsequently implanted samples requires consideration of the implant damage profile. Figure **??** plots the point defect density as calculated by the Monte Carlo simulation package SRIM [62] for a 2 keV Sb implant into silicon. The phonon coherence length has been shown to be insensitive to isolated point defects [117], this being largely due to their limited disruptive potential. This criterion introduces a minimum point defect density which is likely to impact on the PCL. The transition between isolated point defects and extended "amorphous pockets" has been estimated to occur at a point defect to lattice site ratio of 1:3 [118]. Above this ratio the emergence to extended regions of heavily damaged silicon becomes widespread and the spatial confinement of phonons becomes probable. Figure **??** replots figure **??**, indicating,

as a example, the phonon coherence length of the 1×10^{14} Sb cm^{-2} sample. The PCL is the distance between the critical point-defect density for the implant dose considered and the ε-Si/$Si_{1-x}Ge_x$ interface.

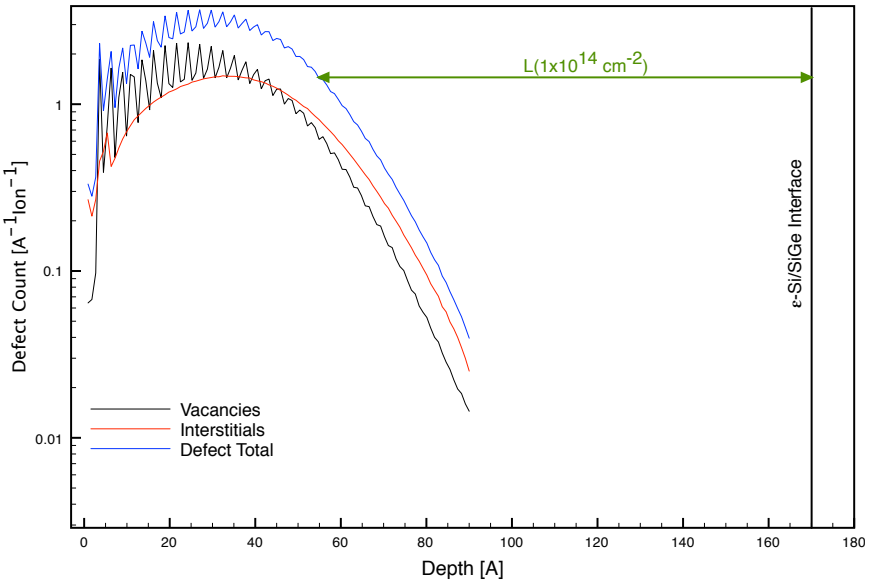

Figure 5.17: Normalized oint defect densities for a Sb implant inot silicon. Also indicated is the PCL of the 1×10^{14} Sb cm^{-2} implant

Taking the distance between the "amorphous pocket"/point-defect transition and the ε-Si/$Si_{1-x}Ge_x$ interface as an estimate of the PCL, figure 5.18 shows the comparative plot between the measured and estimated PCL.

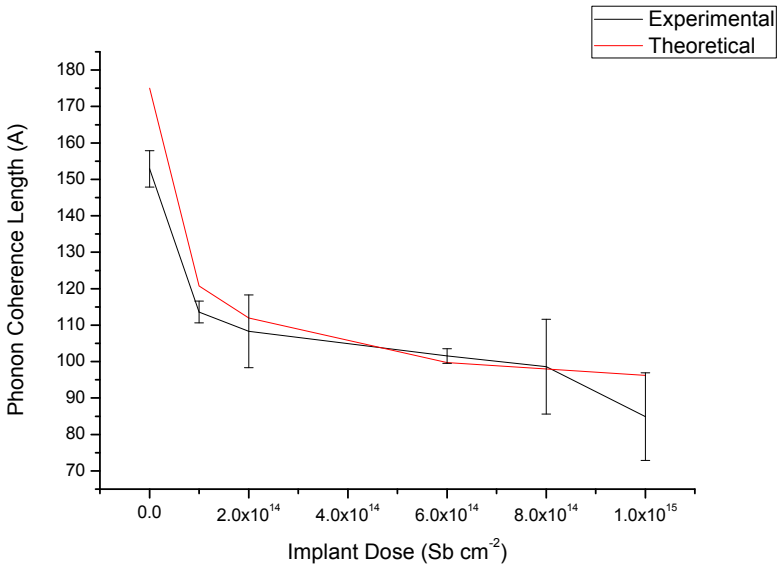

Figure 5.18: Comparison between experimental and theoretical phonon coherence lengths as a function of implant dose.

Although contributions from the native oxide layer, variations in the layer thickness and additional breakdown of momentum conservation due to the high absorption levels at the excitation wavelength have not been taken into account, figure 5.18 shows good agreement between the experimental and theoretical data. The fact that SRIM simulations tend to overestimate the density of point defects (due to their lack of consideration of dynamic annealing effects [118]) may compensate for these additional considerations.

As it was not possible to measure all $Si_{0.83}Ge_{0.17}$ samples on the HR-XRD, extraction of accurate implant induced residual stress was not possible for all doses. In the case of the 6×10^{14} Sb cm^{-2} as-implanted sample, comparing the in-plane lattice constant of the virtual substrate to the Raman calculated stress indicates a residual stress of 0.06125 GPa.

Electronic Effects

The interpretation of the Raman data becomes more complex subsequent to electrical activation. In degenerately doped silicon, the persistent presence of electrons in the conduction band enables transitions between the Δ_1 and $\Delta_{2'}$ conduction sub-bands. These transitions are infrared forbidden but Raman active. At increased electron densities, the energy continuum associated with these transitions overlaps the discrete Raman active optical-phonon transition, giving rise to a Fano type interference (discrete-continuum energy interaction). The resulting interference gives rise to Raman peak broadenings and shifts.

Chandrasekhar *et al.* [119] modified the Fano theory for application to the silicon conduction band by considering a continuum with finite bounds. The interaction scheme envisioned by Chandrasekhar *et al.* is depicted in figure 5.19.

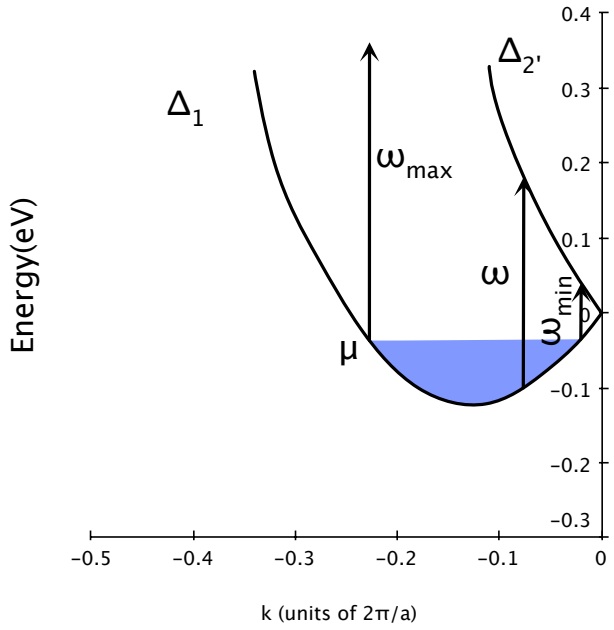

Figure 5.19: The persistent presence of electrons in the conduction band of degenerately doped silicon enables Raman active electronic excitations between the Δ_1 and $\Delta_{2'}$ bands [119].

As shown in figure 5.19, the range of available Raman active electronic energies is determined by the chemical potential and the silicon conduction band structure. Under these conditions, the electron density related Raman shift is given by [119]

$$\Delta\omega_0 = 2\frac{D_0^2}{a^2}\frac{\hbar}{MN\omega_0} \times P\int_{\omega_{\min}}^{\omega_{\max}} D(\omega)\left(\frac{1}{\omega_0-\omega}+\frac{1}{-\omega_0-\omega}\right)d\omega \tag{5.28}$$

where D_0 is the phonon deformation potential, M is the silicon atomic mass, N is the number of unit cells per volume and $D(\omega)$ is the density of states per unit volume.

Although conceptually beneficial, the framework of Chandrasekhar *et al.* is difficult to implement as it necessitates the quantitative modeling of the Δ_1 and $\Delta_{2'}$ silicon conduction sub-bands. An alternative approach adopted by Cerdeira *et al.* is to treat the integral of (5.28) as an empirically determined average transition energy $E_G(0)$. This concession to simplicity leads to the following expression for the carrier density dependent Raman shift in *n*-type silicon [104],

$$\frac{\delta C_{44}^*}{C_{44}^*} = \frac{2\delta\omega_0}{\omega_0} = \frac{1}{C_{44}^*}\frac{2}{3E_G(0)}\left(\frac{D_0}{4}\right)^2 N_d\left(1+\frac{\mu}{E_G(0)}\right) \tag{5.29}$$

where $C_{44}^* = M\omega_0^2/8a$ and N_d is the carrier concentration.

In order to determine this average transition energy, the theoretical shifts in the Raman peak position determined by (5.29) were fitted to the experimentally observed shifts via the variation of $E_G(0)$. Figure 5.20 plots the fitted $E_G(0)$ values for a sub-set of the bulk annealed samples (in order to isolate the effects of carrier density, samples demonstrating deactivation, and thus clustering, were removed from the set).

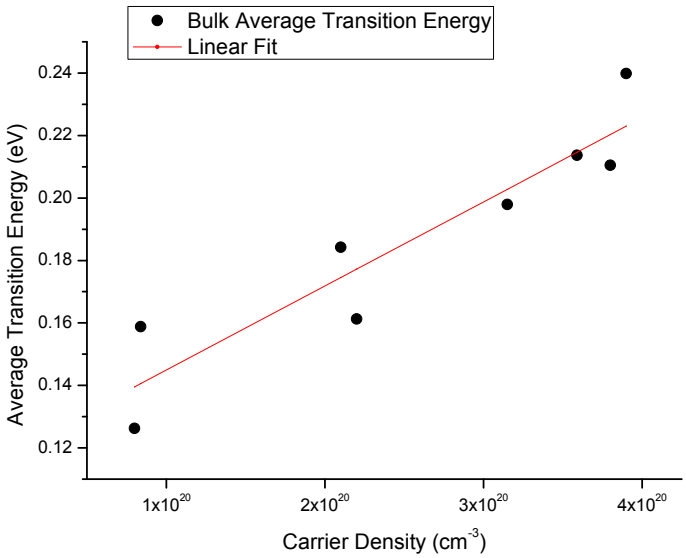

Figure 5.20: Average transition energy extracted from experimental data using (5.29) for bulk activated samples plotted against carrier density, also shown is the linear fit to the data.

Consideration of figure 5.19 indicates that $E_G(0)$ should demonstrate a carrier concentration dependence, this is borne out in figure 5.20. Moreover, assuming the electronic masses in the two sub-bands are equivalent, this dependence should be linear, and to this end figure 5.20 additionally plots the linear fit to the data points. This linear fit allows the extraction of an expression for the average transition energy as function of carrier concentration in bulk silicon,

$$E_G(0) = 2.692 \times 10^{-22} N_d + 0.118 \ (eV) \tag{5.30}$$

Chandrasekhar *et al.* quotes an average transition energy value of ∼0.4 eV for a carrier density of $1.5 \times 10^{20}\ cm^{-3}$, although the current calculations appear to underestimate $E_G(0)$ relative to this, without knowing the full experimental details behind the data, the agreement is reasonable.

Band structure deformation within the strained material is expected to introduce variations in the average transition energy. The preferential population of the two in-plane valleys results in an increase of the chemical potential within the occupied valleys. This redistribution of carriers has been shown to be complete at strains above $\sim 0.8\%$, although the current samples fall slightly short of this strain level (1×10^{14} Sb cm^{-2} samples demonstrate strains in the range 0.65 - 0.69, whereas the 4×10^{14} Sb cm^{-2} and 6×10^{14} Sb cm^{-2} samples have strains of between 0.73 and 0.79), for the current calculations, the redistribution of electrons is assumed to be complete. This assumption should introduce minimal errors as the literature indicates that at strains of $\sim$0.7% the proportion of electrons redistributed has already reached $\sim$90% [11], [61]. This redistribution of electrons implies an off-set between the bulk and strained transition energies. A second implication of the redistribution of electrons is the change in the average conductivity effective mass. As this impacts on the average curvature of the contributing conduction band valleys, the slope of the linear fit is expected to also change. Figure 5.21 plots the average transition energies for 1×10^{14} Sb cm^{-2}, 4×10^{14} Sb cm^{-2} and 6×10^{14} Sb cm^{-2} implanted and annealed samples, again samples demonstrating deactivation have not been included.

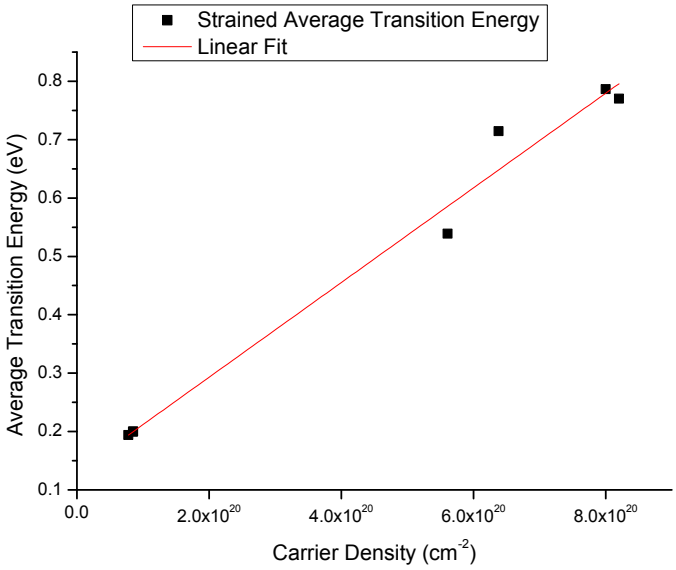

Figure 5.21: Average transition energy extracted from experimental data using (5.29) for strained activated samples plotted against carrier concentration, also shown is the linear fit to the data.

The linear fit to the data of figure 5.21 results in an expression for the average transition energy for strained samples expressed as a function of carrier concentration,

$$E_G(0) = 8.10846 \times 10^{-22} N_d + 0.13088 \ (eV) \tag{5.31}$$

Figure 5.22 translates these average transition energies into carrier density driven Raman shifts and compares these to the experimental data.

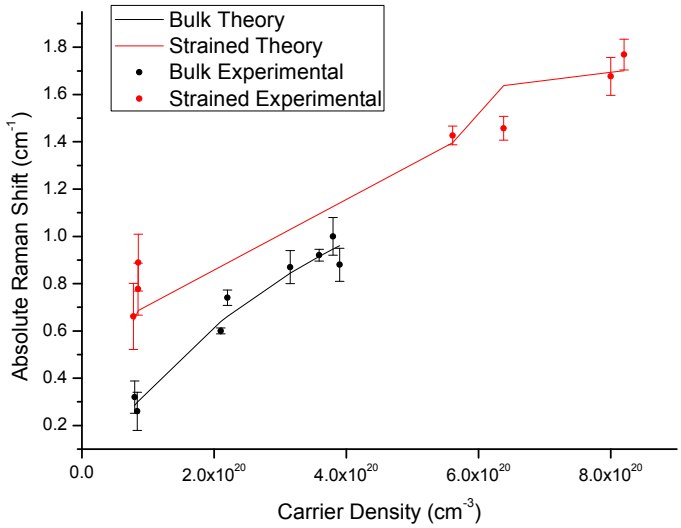

Figure 5.22: Theoretical and experimental carrier density driven Raman shifts.

Conclusions

The characterisation of material stress requires great care when one is dealing with heavily doped silicon. The foregoing arguments demonstrate large Raman shifts with no basis in material strain and highlight some of the potential pitfalls awaiting the unwary experimenter. The continued reference to μ-Raman spectroscopy for future strain metrology within the ITRS [28] demonstrates no awareness of the currently discussed influences and as such may herald problems to come when dealing with degenerately doped device regions.

In closing, figure 5.23 sets forth the data set presented at the beginning of this discussion in the context of the previously detailed Raman shift contributions. The data shows good agreement for most samples. The discrepancy between the theory and experimental data of the 600°C sample is most likely due to an error in the HR-XRD measured strain, however as this tool was out of order at the time of writing it was not possible to confirm this. The

disparity in the 800°C annealed sample data is most likely due to an additional phonon confinement effect resulting from the clustering of deactivated dopant atoms not currently accounted for.

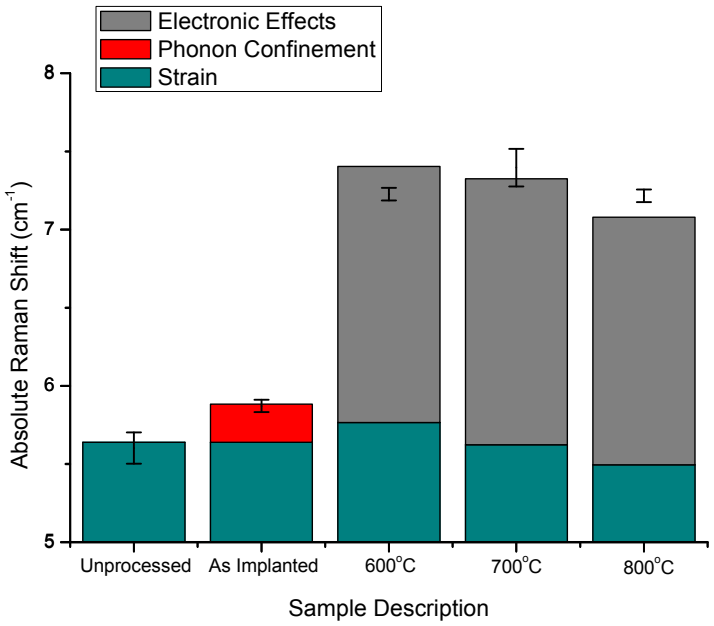

Figure 5.23: Experimental Raman shifts presented in conjunction with the relative contributions of strain, phonon confinement and electronic effects for 6×10^{14} Sb cm^{-2} implanted ε-Si samples.

Chapter 6

Photoacoustic Spectroscopy

In the wider context of the thesis the current chapter may be viewed as somewhat of an outlier. Although the data and theoretical considerations presented here do not necessarily tie in with those of previous chapters directly, the physical attributes investigated certainly do. Throughout this thesis the discussion has at some level been concerned with the impact of lattice damage and/or the transport of thermal energy within the crystal lattice, that being intimately related to the annealing process. The current chapter investigates the mutual dependence of these two properties.

Within this chapter, Photoacoustic (PA) techniques are advanced as being capable of extremely sensitive, fast and non-destructive characterisation of the crystallinity in an ultra-shallow ion-implanted region. The data presented here is uniquely sensitive for a gas microphone configuration, demonstrating sensitivity to radiation damaged regions an order of magnitude shallower than those previously reported.

This work not only demonstrates the possibility of cheaply implemented damage detection, but also provides a method of investigating the processes of thermal energy transfer within

ion-implanted structures, critical to well controlled annealing processes.

6.1 Introduction

PA techniques are sensitive to a sample's geometric, thermal and optical properties. They can provide data analogous to absorption spectroscopy in addition to characterising a sample's thermal production and transfer attributes. The current application concerns itself with the investigation of surface modified solid-state samples, however PA techniques lend themselves equally to the investigation of gases and liquids.

The sequence of events in the PA process begins with the absorption of light within the solid. This, if followed by non-radiative decay, results in the generation of heat. Upon reaching the sample surface, this heat transfers to an enclosed gas which expands. In the situation of constant illumination, one observes an increase in pressure. If however, the illumination is periodically interrupted, an oscillating pressure ensues, otherwise interpreted as a sound wave. Detection of this sound wave, by sensitive microphones, thus allows analysis of heat production and transfer within the absorbing material. In order to perform a PA Spectroscopy (PAS) measurement one measures this acoustic response as a function of incident radiation energy. While in microscopy (PAM) mode one varies either the position or chopping frequency of the light spot, thus either producing a 2-D map of the sample or a depth profile at a point.

Over the course of the current work, PAS measurements demonstrated sensitivity to the ion modified layer, including an apparent dependence on the activation levels within this region. At the experimental chopping frequencies, the investigated sample depth was 5 to 6 orders of magnitude greater than the ion-implanted layer thickness, thereby making this sensitivity somewhat of a curiosity. This chapter presents experimental data demonstrating this

sensitivity and aims to present a theoretical framework to account for the ion-implantation sensitivity.

6.2 Historical Background

In 1880 Alexander Graham Bell discovered that a sound could be heard from a solid sample within a sealed cell illuminated by periodically interrupted sunlight. This curiosity became known as the opto-thermal effect (later to be renamed the Photoacoustic effect to avoid confusion with the thermo-optic effect) [120]. Soon after this discovery Tyndall demonstrated a similar effect in gaseous samples [121].

During the years following its initial discovery, theoretical interpretations of the effect in solids were in flux. Bell initially surmised that the effect was due to the expulsion and re-adsorption of gases from the sample surface [122]. A year later Rayleigh put forward that, in fact, the effect was due to the thermal expansion of the sample. Finally Preece [123] and Mercedier [121] independently hypothesized that the sound generation was actually the result of gas expansion within the cell, with Mercedier stating that the sound was due to the "vibratory movement determined by the alternate heating and cooling produced by the intermittent radiations, principally in the gaseous layer adhering to the solid surface hit by these radiations" [121].

At this point, interest in the PA effect died down as no practical application revealed itself. It became an academic pursuit and remained largely dormant for roughly 50 years. The PA effect made a return in the 1930's in the context of gaseous analyses, in which the effect was relatively easily explained. An understanding of the effect in solids remained elusive.

In the 1960s, the PA investigation of solids experienced a renaissance on the back of advances

in laser technology. As a result, Rosencwaig and Gersho [124] built upon the "thermal piston" model of Preece and Mercedier, publishing in 1975, a theory elucidating the effect and its correlation to absorption spectroscopy (referred to subsequently as the RG theory). This publication, which expounded a 1-dimensional model based on thermal diffusion waves, provided the foundation for the modern understanding of the effect.

Since the 1970s additional theories of the PA effect in solids have been proposed. Some of these have been expansions, with their bases solidly set in the RG theory, e.g. the introduction of thermally thin samples [125] (the concept of thermal thickness is introduced in Appendix D). Others have involved quite radical conceptual departures from the RG theory, such as the work of F.A. McDonald and collaborators in their "composite model" theory [126], and their expansions of this theory to 3-dimensions [127].

6.3 Theory

Thermal Diffusion Waves

PA techniques initially found applications in gas analysis due to the relative simplicity of the data interpretation. Within a gas, absorbed radiation is converted into kinetic energy resulting in an increase of the gas pressure within a closed cell. In the analysis of solids, before pressure oscillations can ensue, the thermal energy must reach the sample surface. This heat propagation within the solid-phase occurs via thermal diffusion waves.

A diffusion wave is a periodically driven oscillation of diffusing particles or energy [128]. In order to derive a mathematical expression for a diffusion wave one couples the classical diffusion equation with an oscillatory force function,

$$\nabla^2 \Psi(\mathbf{r}, t) - \frac{1}{\alpha} \frac{\delta}{\delta t} \Psi(\mathbf{r}, t) = q(\mathbf{r}) e^{j\omega t} \tag{6.1}$$

where Ψ is the thermal energy, $q(\mathbf{r})\, e^{j\omega t}$ in this case represents an oscillatory heat source and α is the material's thermal diffusivity (the transient counterpart of the material's thermal conductivity).

In the case of the thermal diffusion wave, the wave vector is given by $\sigma = (1+j)/\mu$, where μ is the material thermal diffusion length (e^{-1} attenuation length). The equivalence of the real and imaginary parts of this entity results in the diffusion waves demonstrating wave-like behavior even at low frequencies, and introduces a minimum $-45°$ phase shift into measurements (a point which will be revisited in later sections).

Rosencwaig & Gersho Theory

The RG theory considers 1-dimensional heat flow only, this approximation is acceptable in cases where the thermal diffusion length within the sample is much smaller than the illuminated spot size and thus the lateral diffusion of heat is suppressed. Due to the inverse square-root proportionality to chopping frequency demonstrated by the thermal diffusion length, this theory finds many applications in PA studies at high chopping frequencies.

The RG theory is in principle a 1-dimensional "thermal piston" theory, building on the work of Preece and Mercedier; heat generated in the sample travels to the sample/gas interface where it heats a thin layer of gas, this thin layer then acts as a piston on the rest of the gas in the cell. The system is demonstrated in figure 6.1 which has been reproduced from Rosencwaig's 1976 publication [121].

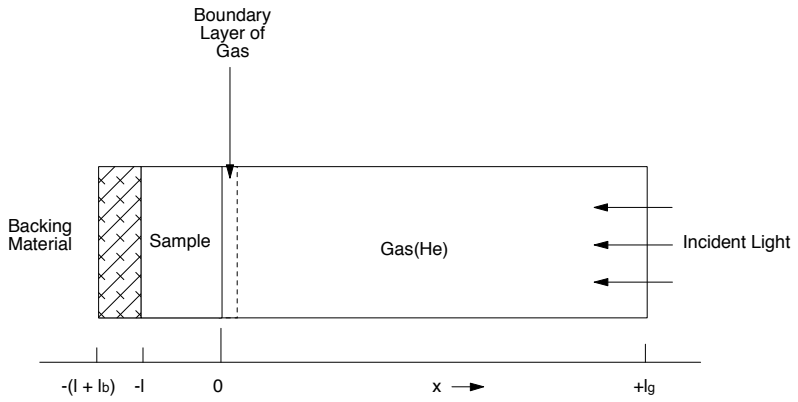

Figure 6.1: Schematic diagram of 1-dimensional photoacoustic system [119].

In the system of figure 6.1, all thermal energy is assumed to originate in the monolayer sample. This is in contact on the top side with an intermediary gas whose pressure oscillations are detected by the microphones (not shown). On the back side, the sample is assumed to be in contact with a backing material of low thermal conductivity.

Before defining the thermal diffusion equation for this system, the thermal properties of the materials should be defined, these are as follows: κ, the thermal conductivity; ρ, the density; C_p, the specific heat capacity (at constant pressure); α, the thermal diffusivity ($\alpha = {}^{\kappa}/_{\rho C_p}$); a, the thermal diffusion coefficient ($a = \sqrt{\omega/2\alpha}$); and μ, the thermal diffusion length ($\mu = \sqrt{2\alpha/\omega}$).

Thermal Energy Distributions

Considerations of the PA effect begin with a chopped light source. For simplicity, this is assumed to be a sinusoidally varying monochromatic source, the intensity of which is given

by

$$I = \frac{1}{2} I_0 \left(1 + \cos \omega t\right) \tag{6.2}$$

where I_0 is the amplitude and ω is the angular chopping frequency ($\omega \equiv 2\pi f$). If β is the wavelength dependent absorption coefficient of the specimen under test, then the thermal energy density generated at a depth x within the solid due to optical absorption is given by,

$$\frac{1}{2} \beta I_0 \exp\left(\beta x\right) \left(1 + \cos \omega t\right) \tag{6.3}$$

where, as in figure 6.1, x takes negative values. Referring back to (6.1) and using this distributed heat source, the thermal diffusion equation within the sample can be written as,

$$\frac{\partial^2 T}{\partial x^2} = \frac{1}{\alpha_s} \frac{\delta T}{\delta t} - A \exp\left(\beta x\right) \left[1 + \exp\left(j\omega t\right)\right] \tag{6.4}$$

with $A = {}^{\beta I_0 \eta}/_{2k_s}$. In the backing and gas this equation becomes,

$$\frac{\partial^2 T}{\partial x^2} = \frac{1}{\alpha_i} \frac{\delta T}{\delta t} \tag{6.5}$$

where i takes the values b and g for the backing and gas respectively.

In order to fully define the thermal distribution within the system, boundary conditions of temperature and heat-flux continuity at the interfaces and the requirement that the cell walls are at ambient temperature are applied. Solving 6.4 and 6.5 consistently with these conditions results in the temperature distribution at the sample surface given by [121],

$$\theta = \frac{\beta I_0}{2\kappa_s(\beta^2 - \sigma_s^2)} \times \left(\frac{(\gamma-1)(b+1)\exp(\sigma_s l) - (\gamma+1)(b-1)\exp(-\sigma_s l) + 2(b-\gamma)\exp(-\beta l)}{(g+1)(b+1)\exp(\sigma_s l) - (g-1)(b-1)\exp(-\sigma_s l)} \right) \tag{6.6}$$

where $b = \frac{\kappa_b a_b}{k_s a_s}$, $g = \frac{\kappa_g a_g}{k_s a_s}$, $\gamma = (1-j)\,\frac{\beta}{2a_s}$ and $\sigma_s = (1+j)\,a_s$.

Production of the PA Signal

The arguments thus far provide a mechanism through which thermal energy generated within the sample is converted into a temperature distribution at the sample surface. PA techniques however do not measure this thermal distribution directly, rather they measure the pressure oscillations within the experimental cell, thus a further means of converting this thermal energy at the sample surface into kinetic energy at the microphone is required.

In their initial postulation Rosencwaig and Gersho hypothesized that this mechanism was provided through the heating of a thin film of gas which subsequently acted as a "thermal piston" on the remainder of the gas. Assuming an ideal gas law relationship within the contact region and an adiabatic response in the remainder of the gas column, the complex envelope of the sinusoidally varying pressure is given by [121],

$$Q = \frac{\beta I_0 \gamma P_0}{2\sqrt{2}\kappa_s l_g a_g T_0(\beta^2-\sigma^2)} \times \left(\frac{(\gamma-1)(b+1)\exp(\sigma_s l)-(\gamma+1)(b-1)\exp(-\sigma_s l)+2(b-\gamma)\exp(-\beta l)}{(g+1)(b+1)\exp(\sigma_s l)-(g-1)(b-1)\exp(-\sigma_s l)}\right) \tag{6.7}$$

where T_0 and P_0 are the ambient temperature and pressure, respectively.

The wave vector of the thermal diffusion wave (under conditions of semi-infinite sample and gas layer thicknesses) has been defined as $\sigma = (1+j)/\mu$. The equality of the real and imaginary parts of this wave vector dictates that thermal energy originating at the sample surface demonstrates a phase shift of $-45°$.

This phase lag can seem counter intuitive until the mechanism of detection is considered. The pressure oscillations detected by the microphones are the result of expansion and contraction of a thin layer of gas in contact with the sample surface. Although thin, this layer has a finite thickness and as such the heat in the gas requires a finite diffusion time to reach its

ultimate extent. Figure 6.2 depicts the thermal amplitude within this gas layer at different time intervals (replicated from the original Rosencwaig & Gersho paper [124]).

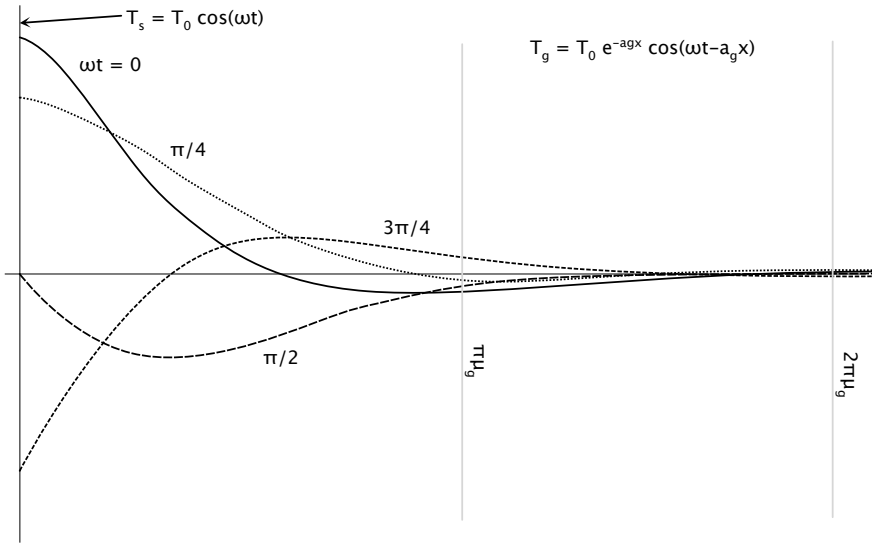

Figure 6.2: Thermal distribution within intermediary gas [122].

In figure 6.2 all thermal oscillations are shown to decay to negligible amplitudes after a distance equal to $2\pi\mu_g$. Within this layer, the periodic thermal profile is given by [124],

$$\varphi_{ac}(x,t) = \theta \exp(-\sigma_g x + j\omega t) \tag{6.8}$$

where $\theta = Q\sqrt{2}l_g a_g T_0/\gamma P_0$, Q is given by (6.7) and all other parameters as previously defined.

The average temperature within this region is thus calculated by integrating the thermal profile within the gas between 0 and $2\pi\mu_g$ and dividing by $2\pi\mu_g$,

$$\overline{\varphi}(t) = \left(1/2\pi\mu_g\right) \int_0^{2\pi\mu_g} \varphi_{ac}(x,t)dx \tag{6.9}$$

giving,

$$\overline{\varphi}(t) \cong \left(1\Big/2\sqrt{2}\pi\right) \theta \exp\left[j\left(\omega t - \frac{1}{4}\pi\right)\right], \tag{6.10}$$

thus invoking a -45° phase shift.

Validity and Limitations of the RG Theory

Rosencwaig and Gersho, by solving the thermal diffusion equation in the presence of a modulated heat source, provided the basis required for Photoacoustic analysis of solids. However, due to the approximations involved, the applicability of their theory to general PA experiments must be verified as they may not reflect the reality of the experimental or sample geometries.

The limitations of the RG theory include the requirements of: monolayer samples; thermally thick backing and gas layers; uniform gas pressure; insignificant sample expansion and insignificant lateral thermal diffusion.

Work carried out by Pavin and Patel [129] allowed the expansion of the RG theory to account for multilayered structures, whereas McDonald's [130] coupled temperature and pressure system allowed the investigation of the theory's validity on the basis of the other counts.

Multilayered Structures

The most immediate deficiency of the RG theory in semiconductor analysis is its inability to examine multilayered structures. The extensions required to introduce layered structures are relatively simple as they allow continued analysis in 1-dimension. Within a layered structure, the contributions to the surface temperature profile can have two origins: a thermally thin surface layer ($L/\mu > 1$) and buried layers.

Before either of these cases can be contemplated however, the indexing scheme of the RG theory must expanded, thus the structure of figure 6.1 becomes that shown in figure 6.3.

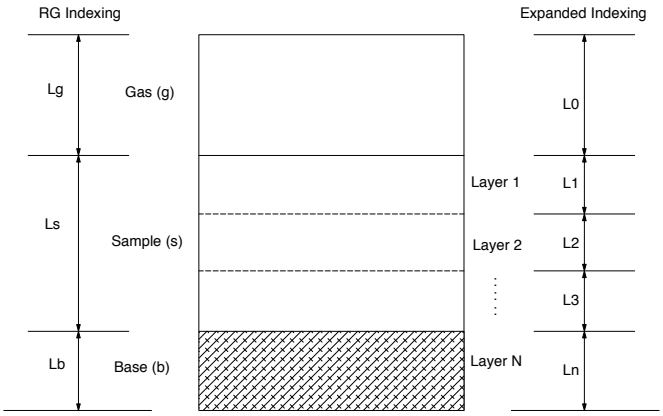

Figure 6.3: Schematic diagram showing both the layer referencing scheme of the RG theory and that of the layered structure referenced subsequently.

Thin Surface Layers

When considering thin surface layers, interface thermal reflection must be accounted for. Within the confines of a 1-dimensional diffusion model, upward and downward propagating waves are generated at the point of absorption. If the heat is generated in a thermally thin top layer, a fraction of the downward propagating wave, through thermal reflection at an interface, may contribute to the PA signal detected.

The calculation of diffusion wave reflectivities differs from those of optical reflectivities. Diffusion wave processes approximate those of traditional waves largely allowing their treatment as such, however, a more accurate description is couched in terms of accumulation and depletion processes [131]. Heat arriving at an interface accumulates and then diffuses away in both directions. For a given interface, the fraction of heat propagating in each direction (transmitted or 'reflected') is determined by the ratio of the thermal effusivities of the materials in contact. The thermal effusivity of a material is a measure of how easily heat can propagate within it and is given by $e = \sqrt{\kappa \rho C_p}$. Using the more general indexing scheme of

the right hand side of figure 6.3, the interface thermal reflection and transmission coefficients are given by,

$$\begin{aligned} R_{therm;i,i+1} &= \frac{1-b}{1+b} \\ T_{therm;i,i+1} &= \frac{2}{1+b} \\ \textit{where } b &= \frac{\sqrt{\kappa_i \rho_i C_{pi}}}{\sqrt{\kappa_{i+1} \rho_{i+1} C_{pi+1}}} \end{aligned} \tag{6.11}$$

Work carried out by Pavin and Patel [129] has extended the RG theory to account for these additional processes in thin layers and the resulting formula is as follows:

$$T(\omega,0) = \frac{\left[1 - R(\lambda)\,\beta_s I_0 T_{therm,g/s}\right]}{4\kappa_s\sigma_s\left(1 - R_{therm,b/s}R_{therm,g/s}\exp\left(-2\sigma_s L_s\right)\right)} \times \left(\frac{1-\exp\left(-\left(\beta_s+\sigma_s\right)L_s\right)}{\beta_s+\sigma_s} + R_{therm,b/s}\exp\left(-2\sigma_s L_s\right)\frac{1-\exp\left(-\left(\beta_s+\sigma_s\right)L_s\right)}{\beta_s-\sigma_s}\right) \tag{6.12}$$

where $T(\omega,0)$ is the chopping frequency dependent surface temperature, $R(\lambda)$ is the wavelength dependent optical reflectivity at the sample surface, $T_{therm,g/s}$ is the thermal transmission coefficient between the sample and the gas above, $R_{therm,b/s}$ and $R_{therm,g/s}$ are the thermal reflectivities at the interfaces with the base and gas, respectively.

Buried Layers

Consideration of interface thermal reflectivities allows good account to be taken of the thermal profile originating within thermally thin surface layers. The extent of the thermal diffusion beyond the surface layer provides however the additional possibility of detection of heat originating in buried layers.

When considering the contribution from subsurface layers, the major additional considerations are light attenuation in the layers previous to the one under consideration, the effects of heat dissipation during propagation from the layer surface to the sample surface and optical and thermal reflectivities at any interfaces encountered.

Light attenuation in previous layers can be accounted for by introducing an exponential term of the form,

$$\exp\left(-\sum_{i=1}^{n-1}\beta_i l_i\right) \tag{6.13}$$

where n represents the index of the layer under consideration. The heat attenuation on return to the sample surface is accounted for using a similar term,

$$\exp\left(-\sum_{i=1}^{n-1}\sigma_i l_i\right) \tag{6.14}$$

The optical reflectivities and thermal transmissions at interfaces can be accounted for by using the terms,

$$\prod_{i=1}^{n-1}\left(1-R_{opt;i/i+1}\right) \tag{6.15}$$

$$\prod_{i=1}^{n-1}\left(T_{therm;i+1/i}\right) \tag{6.16}$$

where $R_{opt;i/i+1}$ is the optical reflection coefficient at the interface between layer i and $i+1$ and $T_{therm;i/i+1}$ is the thermal transmission coefficient between layers i and $i+1$.

The result of these extensions to the RG theory is a general 1-dimensional theory capable of dealing with multilayer structures,

$$\begin{aligned}(\omega,0)=\sum_{n=1}^{N}\Bigg\{&\frac{\exp\left(-\sum_{i=1}^{n-1}\left(\beta_i l_i+\sigma_i l_i\right)\right)\left[1-R\left(\lambda\right)\right]\beta_n I_0 T_{0/1}}{4\kappa_n\sigma_n\left(1-R_{n+1/n}R_{n-1/n}e^{-2\sigma_n L_n}\right)}\times\\ &\prod_{i=1}^{n-1}\left[\left(1-R_{opt,i/i+1}\right)\left(T_{therm,i/i+1}\right)\right]\times\\ &\left(\frac{1-e^{-(\beta_n+\sigma_n)L_n}}{\beta_n+\sigma_n}+R_{n+1/n}e^{-2\sigma_n L_n}\frac{1-e^{-(\beta_n-\sigma_n)L_n}}{\beta_n-\sigma_n}\right)e^{j\omega t}\Bigg\}\end{aligned} \tag{6.17}$$

Coupled Temperature and Pressure

Over a series of papers between 1978 and 1980, F.A. McDonald and colleagues developed a theoretical framework which accounted for most of the short comings of the RG theory. They did so by solving not only the thermal diffusion equation, but by solving the coupled linear equations for temperature and pressure [126],

$$\begin{aligned} \nabla^2 p - \frac{\rho_0}{B}\frac{\partial^2 p}{\partial t^2} &= -\rho_0 \beta_T \frac{\partial^2 \tau}{\partial t^2} \\ \kappa \nabla^2 \tau - \frac{\kappa}{\alpha}\frac{\partial \tau}{\partial t} + S &= -T_0 \beta_T \frac{\partial p}{\partial t} \end{aligned} \quad (6.18)$$

where ρ_0 and T_0 are the ambient gas density and temperature, B is the isothermal bulk modulus, β_T is the thermal expansion coefficient, S represents the thermal-energy source and τ and p are temperature and pressure respectively. Without presenting the derivation, the solution for the variation of gas pressure in this system is given by,

$$p_g \approx -\frac{j}{\omega}\frac{\gamma P_0}{l_g}\frac{I_0}{2\rho_s C_{ps}}\left(\frac{\beta}{\sigma_g T_0 (g+1)(\gamma+1)} + \beta_T \left[1 - \exp\left(-\beta l_s\right)\right]\right), \quad (6.19)$$

where γ is the ratio of the specific heats C_p/C_v and all other variables are as previously defined. The full derivation of this equation can be found in [126].

Using (6.19) McDonald *et al.* investigated the validity of the RG theory and the approximations involved therein. Their conclusions were that, for the majority of experimental set-ups, the simpler RG theory provided a reasonable representation of the data [132]. In particular, the effects of thermal thickness of the gas and backing were found to be negligible at chopping frequencies greater than ∼10 Hz; when operating in the audio frequency range, the wavelength of the pressure oscillations were sufficiently long to ensure insignificant deviation from uniform gas pressure; and at all but the highest frequencies, the thermal expansion of the sample was shown to be inconsequential with respect to the gas expansion.

McDonald *et al.* followed these investigations by expanding their composite piston model to account for lateral thermal diffusion (a full 3-dimensional composite piston model can be found in [133]). The conclusion reached as a result of these investigations was that in cases where the thermal variations were unhindered by the cell walls, the thermal flux resulting from 3-dimensional diffusion is identical to that of 1-dimensional diffusion [127].

These results justify the use of the RG theory in many but not *all* applications. Specifically refuted is the applicability of the RG theory in cases where the thermal diffusion length is comparable to, or larger than, the illumination spot-size and appreciable signal reaches the cell walls [130]. As will be demonstrated, these conditions arise during the course of the investigations to follow and as such, a 3-dimensional model must be considered.

6.4 Experimental Details

Instrumentation

The PA system used in the current work was developed in-house. It was designed to have both spectroscopy and microscopy capabilities. In spectroscopy configuration the tool operates over a spectral range incorporating the bandgap of some of the more commonly used semiconductors e.g. Si, Ge, GaAs, i.e. $\sim$ 0.6 eV - 1.5 eV. In microscopy mode the tool has the capability of X-Y mapping in addition to depth profiling (made possible through the thermal diffusion length's dependence on chopping frequency).

The system operates by illuminating the specimen under test with chopped light of varying energy and measuring the acoustic response within a small volume ($\sim$300 mm^3). Figure 6.4 shows a schematic of the system.

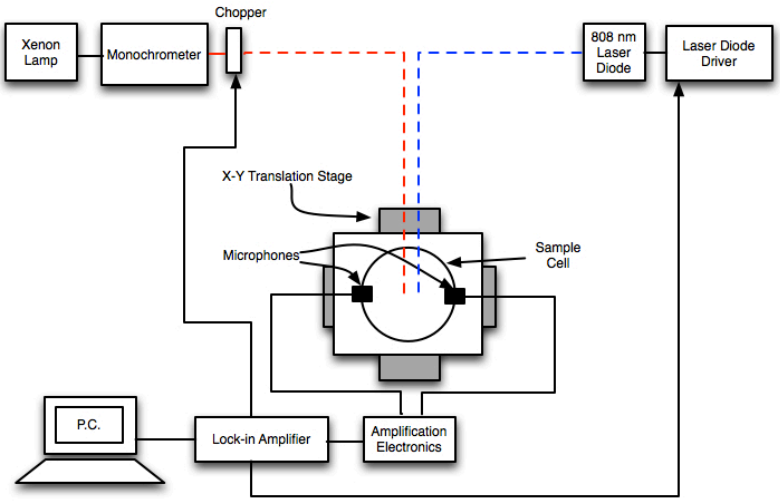

Figure 6.4: Schematic diagram of photoacoustic system used.

Light Source & Chopper

The light source used in the PAS system is a 300 W Short Arc Xenon lamp (Oriel model 6258) with a usable wavelength spectrum of between 200 nm and 1600 nm. The lamp is contained in a lamp housing (Oriel model number, 66902). Prior to monochromatization the light is modulated at 70 Hz by an Oriel 6195 chopper controlled by an Oriel chopper controller (model number 75160). The reference signal for the chopper controller is taken from the TTL-sync-out of the lock-in amplifier.

In PAM mode the light source is a TTL modulated 3W, 808 nm laser diode. The measurements were taken at a average optical power density of $\sim$25 Wcm^2 assuming a 0.5 mm spot diameter.

Monochromator & Filter

On the Photoacoustic Spectroscopy side, the chopped light is selectively monochromatized through the combination of a $^1/_4$ m 'Corner Stone' monochromator and the accompanying filter wheel (Oriel model number 74010). Within the monochromator are three gratings which between them provide the a wavelength selection range of ∼180 - 2800 nm (schematic shown in figure 6.5). Upon exiting the monochromator, the light is incident on a band-pass filter, which removes any harmonic contamination. The spectral resolution of the system is determined by the width of the exit slit. As solid-state PAS signals are generally very weak, higher intensity is of more benefit than spectral resolution, therefore, the slit is set almost completely open (∼5 mm). The output power from the monochromator at a wavelength of 1000 nm (an average intensity in the spectrum) was measured to be ∼9 mW, this being in line with previously reported intensities on the system (12 mW).

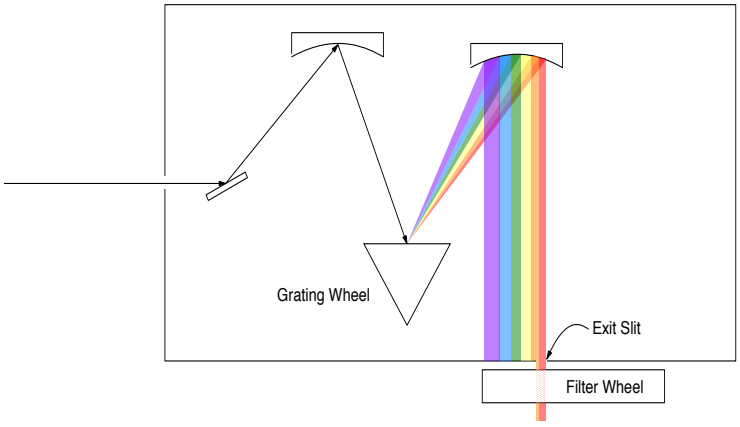

Figure 6.5: Schematic diagram of 1/4 m 'Corner Stone' monochromator used in PAS experiments.

Mirrors & Cell

In the PAS (PAM) system a series of mirrors (lenses) is used to focus the modulated, monochromatized radiation on the sample within the photoacoustic cell. The cell itself is constructed out of aluminium and the active volume is designed to be as small as possible while still being able to accommodate the sample and a gas inlet and outlet system. The experimental spot size was approximately $4mm \times 2mm$ (0.5 mm diameter) for the PAS (PAM) and the radius and height of the cell were 7.5 mm and 5 mm, respectively. Prior to measurements, the cell was filled with helium because of its increased thermal conductivity. The seal on the cell is achieved via a Spectrosil® window which allows transmission over the entirety of the operational spectrum of the lamp.

Electronics

The PA cell is fitted with four Knowles FG-3629-P16 microphones each of which is connected through preamplifier and summing amplifier circuits, to a Stanford Research Systems SRS830 DSP lock-in amplifier which extracts the frequency component of interest and passes this on to the PC. Along with the amplitude, the phase shift of the acoustic signal relative to the incident radiation is measured.

Data Processing

PAS measurements taken by this system are a convolution of the sample signal of interest and contributions attributable to the cell, the microphones and the amplification electronics in addition to the spectral intensity variations of the light source. In order to extract meaningful data, some processing is required.

In order to compensate somewhat for the low signal-to-noise ratio of the measurements, the data presented are the average of 5 scans each.

In order to take account of phase shifts and amplitude variations originating outside the sample the data is normalized with respect to a standard sample, namely either carbon black [134], or a crystalline silicon sample [135].

The final step in the data processing was to apply a 5 point Savitzky-Golay filter to further suppress the effect of noise.

6.5 Results & Analysis

During the course of this project, PA techniques presented themselves as possible means to nondestructively characterise both implant damage and electrical activation. Figure 6.6 shows the PAS amplitude and phase data taken on bulk silicon samples implanted with an antimony fluence of $2 \times 10^{14}\ cm^{-2}$ at an energy of 2 keV and subsequently annealed at $600°C$, $700°C$ and $800°C$; also shown is the data of a control p-Si sample (Reference Silicon). This data was taken in the spectroscopy mode of operation, i.e. chopping frequency was held constant and wavelength of the incident light was varied.

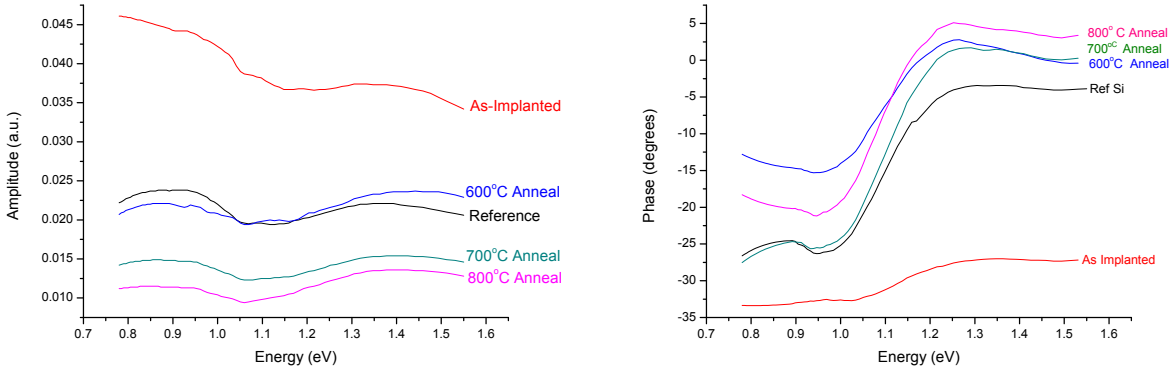

(a) Amplitude (b) Phase

Figure 6.6: Normalized PAS amplitude and absolute phase data measured on bulk silicon samples: control sample, as-implanted sample (2×10^{14} Sb cm^{-2} at an energy of 2 keV) and three implanted and subsequently annealed samples.

The trends of the spectra presented (which are representative of other data collected) show large increases in both amplitude and phase lag upon implantation. After annealing at 600°C there is a large return in both shape and offset of the spectra, this being especially evident in the amplitude data where there is an almost complete overlap with the control data. The phase data demonstrates this retunt at the higher temperature of 700°C and finally the 800°C annealed sample, for both amplitude and phase demonstrates a departure from the crystalline silicon data. This post implant anneal trend appears imitative of the electrical and Raman data previously presented, especially so for the phase data, as demonstrated in figure 6.7.

Due to the convolution of optical, thermal and geometric properties present in these spectra, a full analysis of the data set is beyond the scope of the current work. Rather, an attempt is made to account theoretically for the impact of ion-implantation on the photoacoustic response, the similarities shared with electrical activation data are currently merely noted.

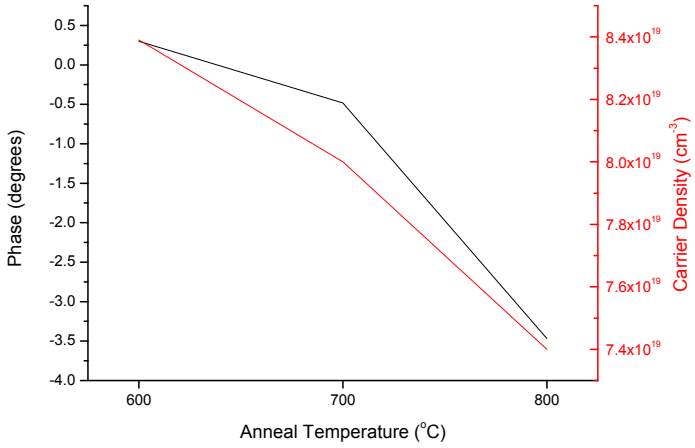

Figure 6.7: Comparison between the high PA energy phase shift and the carrier density within the anneal 2×10^{14} Sb cm^{-2} samples.

Due to the additional dependencies of the PA amplitude on light-to-heat conversion efficiencies and optical reflections, the majority of the following analysis is carried out on the phase data.

Both the amplitude and phase spectra demonstrate most activity in the spectral region of the silicon band-gap. Increases in amplitude and reductions in phase upon crossing this threshold are both attributable to reduced optical penetration depths, as heat generation becomes localized at the sample surface. The phase offset of the as-implanted spectrum however is not so easily explicable as increased absorption in the as-implanted region would, if anything, further localize heat generation to the surface region. This appears to be in conflict with the data. An additional curiosity is the fact that any effect is observed at all as the ion-implanted depth near the surface accounts for $\sim 1 \times 10^{-6}$ of the investigated thickness at the experimental chopping frequency of 70 Hz ($\mu_{Si} \approx 0.6\ cm$) .

In the following analysis, the silicon band-gap is used to separate the spectra into high and low energy regions; the high energy region isolates thermal diffusion processes through the assumption of surface heat generation, the low energy considerations then incorporate the

additional effects of extended optical absorption.

High Energy Phase Shifts

At high (i.e. above bandgap) energies, figure 6.6 demonstrates a $\sim 25^{\circ}$ phase shift between the reference and as-implanted samples. This must be accounted for by arguments unrelated to optical penetration depths as the sense of the shift is counter to that predicted by optical absorption arguments.

Within photoacoustic analysis the above band-gap spectral region of a semiconductor is a commonly considered region, so much so, it has been attributed its own name, 'the saturation region'. Within this spectral region, heat can be taken to originate at the samples surface and all effects considered to be due to thermal transport properties (assuming the experimental conditions remain in the 1-D paradigm). The phase shifts of the 'saturation region' in the PAS measurements are due in part to thermal conductivity changes upon ion-implantation, however these measurements are afforded additional sensitivity through a parameter called the 'thermal interface resistance' due to the particular experimental set-up of the measurement. This term will be treated in turn, however, firstly the thermal conductivity of the ion-implanted layer is considered.

Thermal Conductivity

The thermal interface resistance has been shown to have maximum effect on results when two conditions are adhered to: firstly, the heat source duration, or half the period of the excitation ($t_h = 1/2f$) must be greater than the characteristic diffusion time through the thin-film ($t_c = l/4\kappa$); the second condition is that the excitation spot size be large enough to suppress 3-dimensional thermal diffusion i.e. spot size diameter, a, must be much greater

than the film thickness, l [136]. In the case of the PAS experimental set-up both of these conditions are adhered to; $t_h = 0.0071$ s, $t_c = 0.004$ s, $a = 0.4$ cm, $l = 10 \times 10^{-7}$ cm.

The conditions laid out above imply that measurements are most sensitive to thermal interface resistance at low frequencies and with excitation spot sizes sufficiently large to suppress 3-dimensional thermal diffusion. It therefore follows that experiments carried out at high frequency and with small spot sizes should be negligibly respondant to this parameter. It is for this reason that measurements of the thermal conductivity of the ion-impanted layer were carried out in the photoacoustic microscopy (PAM) configuration.

The laser spot diameter for the PAM equipment is ∼0.5 mm (as opposed to the ∼4 mm diameter of the PAS system) and the fact that it uses TTL modulation allows access to much higher frequencies than the 400 Hz limit of the mechanically chopped PAS system. By performing a frequency scan, a depth profile of the sample can be generated and by normalising this to a control silicon scan, the effects of the as-implanted layer can be isolated. Figure 6.8 shows the thus normalised phase shifts of the, 4×10^{14} cm^{-2}, 8×10^{14} cm^{-2}, 10×10^{14} cm^{-2} as-implanted samples.

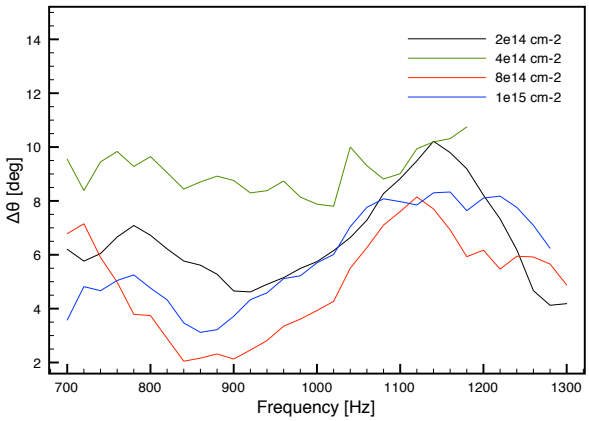

Figure 6.8: Phase shifts relative to the control sample for four of the as-implanted samples as a function of chopping frequency.

Analysis of the normalised frequency scans of figure 6.8 allow the extraction of the thermal conductivity and optical absorption coefficient of the ion-implanted layer. Figure 6.9 (a) shows a sample fit (indicative of others), while 6.9 (b) plots the extracted thermal conductivity of the four samples measured.

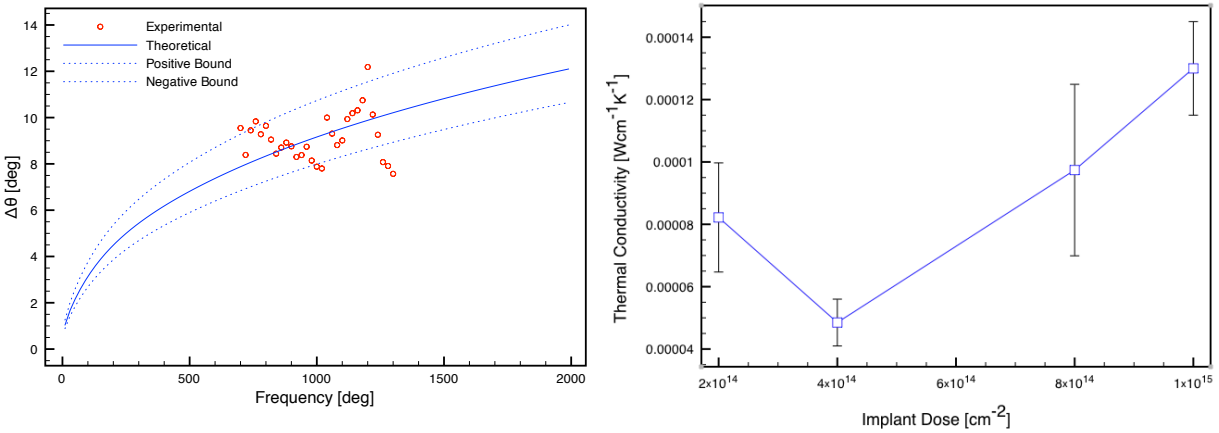

(a) (b)

Figure 6.9: (a) Representitative sample fit ($4 \times 10^{14}\ cm^{-2}$), also shown are positive and negative bounds used to estimate error bars for the extracted thermal conductivity plot. (b) Extracted thermal conductivity for the samples investigated.

There appears to be a linear trend in the thermal conductivities of the as-implanted sample with antimony dose of $4 \times 10^{14}\ cm^{-2}$ and above (the presence of onny 3 data points admitedly make this assertion rather speculative). The sense of this trend appears to be counterintuitive if one considers implant damage alone, however, the relatively small range of the increase, and the linear nature of the trend, suggest some minimal activation of dopants in the samples, possibly due to dynamic annealing during implantation. Relative to this linear trend, the $2 \times 10^{14}\ cm^{-2}$ as-implanted sample appears to have a relatively large thermal conductivity (although still far below that of crystalline silicon $\sim 1.5\ Wcm^{-1}K^{-1}$). This increase may indicate that the $2 \times 10^{14}\ cm^{-2}$ as-implanted sample is not quite fully amorphised. This is slightly at odds with the SRIM data previously presented, however may also be the result

of dynamic annealing during room temperature implantation.

The thermal conductivities extracted appear to be lower than those of the literature, e.g. in the case of Zammit *et al.* [137], by almost 2 orders of magnitude, however the variation in sample treatment and experimental conditions make direct comparisons difficult.

Using this data alone, the phase shift within the $2 \times 10^{14}\ cm^{-2}$ as-implanted sample and the crystalline sample was calculated to be, $\sim 1.8^{\circ}$ at 70 Hz. This lack of sensitivity at low frequencies implies that the effects of thermal interface resistance have largly been removed. It remains now to reintroduce and calculate this term.

Interface Thermal Resistance

The effects of layer interfaces have been discussed in previous sections in the context of applying the RG theory to multilayered structures. This describes the mechanism by which reflection of diffusion waves proceeds - thermal build up at the interface followed by back diffusion of heat. The current model, and indeed all others encountered, proceed from an assumption of thermal equilibrium across each interface. This however is an approximation, one which is not entirely consistent with the aforementioned thermal build-up on one interface side. Given enough time it can be assumed that the temperature across the interface will equilibrate, however, equally it must be considered that a transient thermal inequality exists at any interface. This transient inequality is the source of the thermal interface resistance.

The previous section outlined the conditions most conducive to observation of this phenomenon. Firstly, as there is heat build up at the interface for the duration of the heat pulse, should this time become large with respect to the diffusion time, a delay in the heat arriving at the sample surface is observed (i.e. a phase lag). Secondly, as the heat propagating perpendicularly to the interface is the only component sensitive to the interface, the

1-dimensional nature of the diffusion must be maximized.

Under these conditions the thermal interface resistance can be calculated as [136],

$$\frac{l}{\kappa_{eff}} = \frac{l}{\kappa_F} + R_{int} \tag{6.20}$$

where l is the film thickness, κ_F is the film thermal conductivity (previously calculated) R_{int} is the thermal interface resistance and κ_{eff} is the effective thermal conductivity as calculated by [136],

$$\frac{1}{\kappa_{eff}} = \frac{\pi}{4}\frac{l}{a}(\frac{1}{\kappa_{app}} - \frac{1}{\kappa_s}) \tag{6.21}$$

where a is the spot size diameter, κ_s is the substrate thermal conductivity, and κ_{app} is the apparent thermal conductivity as extracted for the PAS data ($\kappa_{app} = 2.48 \times 10^{-6}\ Wcm^{-1}K^{-1}$).

Using (6.20) and (6.21) the interface thermal resistance was calculated to be 0.016 cm^2KW^{-1}, this value is roughly an order of magnitude greater than literature data for amorphous silicon on a crystalline silicon substrate($R_{int} = 0.0015\ cm^2KW^{-1}$ [136]), however, again, direct comparison is not entirely justified. The phase shift resulting from this combination of thermal conductivity and thermal interface resistance is 23.36°.

Low Energy Phase Shifts

As the excitation energy reduces (to energies below the bandgap), the applicability of surface heat generation becomes questionable. The extension of the optical penetration depth, results in an extended thermal energy source, increasing the detected phase lag. The current considerations are not exhaustive but rather attempt to validate the trends of the spectra.

Low Energy Simulations

In order to account for the additional phase contributions introduced by an extended heat source, a weighted average approach is adopted. Under conditions of constant optical intensity throughout the sample, the contribution from each elementary source as a function of depth is determined by the exponential decay of diffusion wave intensities, e^{-ax}, where a is the thermal diffusion coefficient and x is the depth of the source. The presence of optical absorption within each layer and thermal reflection at the each interface, adds additional terms to the weighting function. The general expression for this was determined to be,

$$w = \sum_{n=1}^{N} \left\{ \begin{array}{c} \left[\exp\left(-\sum_{i=1}^{n-1}\left(\beta_i L_i + a_i L_i\right)\right)\prod_{i=1}^{n-1}\left(T_{i/i+1}\right)\right] \times \\ \left[\exp\left(-\left(\beta_n + a_n\right)d_n + \exp\left(-\left(\left(\beta_n + a_n\right)\left(2L_n - d_n\right)\right)\right)\right)R_{n/n+1}\right] \end{array} \right\} \tag{6.22}$$

where β is the optical absorption coefficient (taken to be the theoretically calculated values of [138]) and d_n is the depth of the thermal source within layer n and is given by,

$$d_n = x - \prod_{i=1}^{n-1} L_i \tag{6.23}$$

$R_{n/n+1}$ in (6.22) is the thermal reflection coefficient at the interface between layer n and the layer immediately below it. Equation (6.22) accounts for thermal reflections only at this first encountered interface as the impact of upward propagating heat originating from reflections at further underlying interfaces is currently considered to be negligible. The terms within the first set of square brackets of (6.22) account for optical and thermal attenuation in layers previous to the one under consideration and those in the second set of square brackets account for light attenuation and heat production, attenuation and reflection within the current layer.

The RG theory states that given a semi-infinite gas thickness in contact with the illuminated sample surface, a phase shift of $-45°$ is observed. This implies that given a semi-infinite,

uniform heat source within the sample, a further phase shift of -45° will originate within the sample. This coupled with RG's approximation that heat originating 1 thermal diffusion length from the surface results in a -45° phase shift (implied by (6.7) and borne out through calculation) allows quantification of the phase shift resultant from thermal diffusion within the sample as a function of distance travelled. Extrapolating the linear fit of these distance/phase points ($(0,0)$ and $(\mu,-45)$), expressed simply by,

$$\theta = -75x \tag{6.24}$$

where θ is the additional phase shift, gives a phase shift of -282° at $2\pi\mu$ and a spatially averaged phase shift of -43.7°, validating the previous approximation. Multiplying this line equation by (6.22) gives the weighted average phase arising from diffusion of heat to the sample surface from an extended source. Averaging this over the sample thickness gives the predicted additional phase shift as a function of optical absorption coefficient.

The dearth of numerical optical absorption data for ion-implanted materials makes accurate estimation of this property's impact difficult. The current calculations are based on the absorption spectrum of ion-implanted silicon presented in [135] (replicated in figure 6.10). This data is based on $2.8 \times 10^{14}\ cm^{-2}$ silicon self-implants at an energy of 300 keV. Although these parameters are not in line with those of the current samples, the simulations proved relatively insensitive to the optical absorption coefficient of the implanted layer most likely due to its thinness.

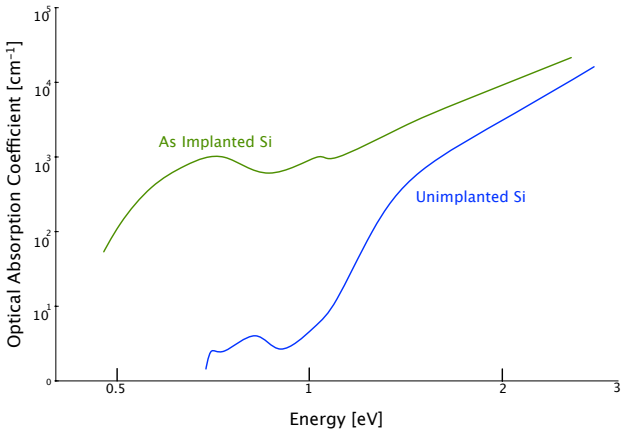

Figure 6.10: Experimental optical absorption data for crystalline and as-implanted ($2.8 \times 10^{14} cm^{-2}$ silicon self-implants at an energy of 300 keV) [133].

Figure 6.10 recounts the control and as-implanted phase data of figure 6.6. Overlayed on this graph are the simulated results of the theoretical considerations put forward. As the calculations have been relative to the high energy crystalline phase shift throughout, figure 6.10 plots the data similarly.

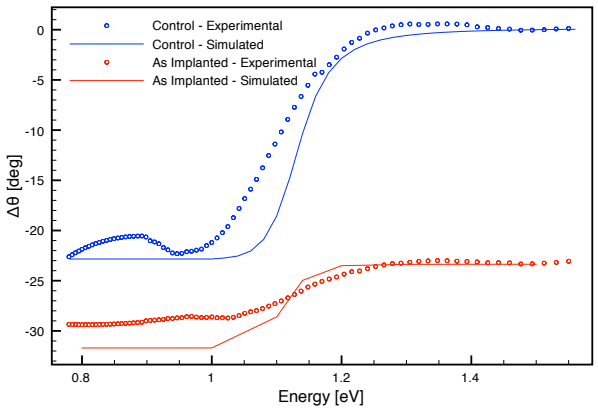

Figure 6.11: Experimental and simulated data for the control and $2 \times 10^{14} cm^{-2}$ as-implanted samples; all data has been normalised to that of the high energy response of crystalline silicon.

Figure 6.11 demonstrates excellent agreement between the experimental and simulated data. The discrepancies in the low energy region of the as-implanted spectrum are likely due to the values for the absorption coefficient used. The fact that there is reasonable agreement however, opens the possibility for future estimation of the optical absorption is these samples.

6.6 Conclusions

The experimental data presented in this section suggests that PA techniques have the capability to nondestructively monitor implant damage and the subsequent post-anneal return of crystallinity.

The similarities between the trends of the PA data and those of the electrical and Raman data are yet to be investigated, however at this point it would not seem unreasonable to speculate that the deactivation of antimony subsequent to the 800°C anneal results in additional disorder within the surface region which is detectable through variation in the thermal conductivities and interface thermal resistance at the sample surface.

Notwithstanding the further research required, the current experimental data and theoretical considerations strongly suggest that PAS is capable of identifying lattice damage caused by ultra-shallow implants. These investigations demonstrate sensitivities to layers orders of magnitude thinner than those previously reported for the gas-microphone configuration.

Chapter 7

Conclusions

This project was inspired by investigations into the solubility enhancements of antimony in ε-Si, carried out by project partners in the University of Surrey. The project, at its outset was designed to be a complementary work, investigating the stability of the ε-Si layers in response to ion-implantation and rapid thermal annealing, and expanding the range of strain levels investigated.

Initial investigations were carried out on the $Si_{0.83}Ge_{0.17}$ linearly graded samples and as such full electrical and SIMS data were available for these samples. For other strains, the electrical characterisation became problematic as Prof. Nick Cowern and Dr. Nick Bennett moved from the University of Surrey to Newcastle University and in the process lost access to the Differential Hall kit. The preparation of the samples also became problematic during this period as access to annealers became limited and subsequent to the 700°C anneals, access to this tool was also lost (other anneal temperatures were not possible due to calibration issues). Samples were thus sent to a group affiliated with another project under the Nanomaterials Processing Laboratory umbrella. HR-XRD measurements of these sample revealed no ε-Si layer and SIMS investigations (aimed at confirming/refuting the "snow-ploughing" effect

resulting from SPER) revealed that the ε-Si layer had been consumed by an oxide. Due to the expense (both time and money) involved, it was not possible to reproduce these samples.

The curtailment of the sample set was compounded by the discovery that μ -Raman spectroscopy was an unsuitable method of strain characterisation within the processed samples. The mid-project purchase of the Bede-D1 allayed some of the strain characterisation issues, however the extended scan times and initial reliability issues with the system meant that measurements had to be undertaken with specific investigative goals in mind and a full characterisation of the expanded sample set was not possible.

These limitations on the sample set and strain measurements demanded a restructuring of the project and thesis. Additionally, the emergence of non-stress related shifts in the Raman data, and the observation of, at the time, unaccounted for phase shifts in the PAS measurements both required further investigation. Although the delineation is not belaboured, the structure of this thesis was thus designed to separate the investigations into two categories; those characterizing the samples and those characterizing the techniques.

7.1 Sample Characterisation

The sample characterisation had two main goals, firstly determination of the effects of the industrial processes on strain stability within the ε-Si layers and the dynamic relationship between strain relaxation and electrical activation; and secondly, determination of the relative stability of ε-Si layers grown on linearly and terrace graded VS.

Prior to discussing the effects of sample processing, production of the base samples is considered. HR-XRD measurements revealed strain relaxed $Si_{1-x}Ge_x$ layers with ε-Si capping layers. SXRT investigations revealed the mechanism of strain relaxation within the $Si_{1-x}Ge_x$

layers, in the form of orthogonal misfit dislocation arrays. In samples demonstrating appreciable lattice miscuts HR-XRD measurements revealed decreasing lattice tilts through the relaxed $Si_{1-x}Ge_x$ layers, consistent with asymmetric misfit dislocation development. SXRT measurements supported these findings. The emergence of stacking faults within ε-Si grown on $Si_{0.70}Ge_{0.30}$ VS demonstrates the critical thickness of the 30° partial dislocation has been reached, an assertion supported by the small degree of strain relaxation within these samples. Of greatest consequence to the strain levels within the ε-Si layers is variability in the germanium content of the virtual substrates. In some cases this term varied by over 15% of it nominal value resulting in large variations in the ε-Si strain layers.

The impact of the processing steps on strain stability were, for the most part, minimal with the notable exception of the $Si_{0.83}Ge_{0.17}$, 1×10^{14} Sb cm^{-2}, 800°C and 6×10^{14} Sb cm^{-2}, 700°C samples. The fact that these two sample incorporate linearly graded substrates highlights the disparity in the stability of the two underlying structures. ε-Si layers grown on the terrace graded structure demonstrated increased stability due to the suppression of substrate originating threading dislocations. Within the linearly graded samples relaxation of the ε-Si layer was observed even in layers whose thicknesses were well below their theoretical critical thickness, suggesting an appreciable pre-existing dislocation density. The relative merits of the linearly and terrace graded virtual substrates were in line with the literature.

Calculations based on solid solubility theory revealed that the level of strain relaxation within the samples could not account for the large levels of deactivation observed subsequent to 800°C anneal. Therefore strain relaxation, while being a contributing factor, cannot be considered as the major precursor to electrical deactivation in these samples.

In conclusion, the combined results of the current work and that started by project partners in the University of Surrey, suggests that the use of biaxial tensile strained silicon and antimony ion-implantation coupled with rapid thermal annealing, presents a viable option for

the production of future generation n-type source drain extension regions. This assertion is based on the additional conductivity resulting from conduction electron effective mass reductions and antimony activation increases, coupled with minimal strain reduction in samples grown on terrace graded virtual substrates. In point of fact, the use of the $Si_{1-x}Ge_x$ virtual substrate stressor, although challenging, allows the additional dopant activation responsible for a large proportion of the reduced resistivity.

7.2 Technique Characterisation

Raman Spectroscopy

The μ-Raman measurements of this project, while originally being aimed at characterizing the ε-Si stress, quickly turned into an investigation of μ-Raman's sensitivity to crystal damage and degenerate carrier densities.

In the case of implant damage, the effects can be accounted for by the phonon coherence length, a model relating the accessible range of scattering momenta and the degree of phonon spacial confinement.

The additional sensitivity of μ-Raman spectroscopy to electronic transitions in degenerately doped silicon calls into question the proportion of the Raman shift which is attributable to stress. As a result of this, in order to characterize the sample fully, independent strain measurements are required. The interactions between continuous, Raman-active electron scattering events and discrete phonon excitations must be taken into account. The current work relies on empirical determination of the Raman-active electron transition energies and, as such, gives good results, however the values extracted are in reasonably good agreement with those available in the literature.

Photoacoustic Spectroscopy

The photoacoustic investigations within this project reveal some of the capabilities of this technique. The variation of the incident light energy results in data analogous to those of absorption spectroscopy, with the exception that the signal originates purely from the absorbed light rather than requiring extraction via transmitted and reflected measurements. Photoacoustic techniques' sensitivity to the period of chopping and spot-size provide additional sensitivity for the detection of ion-implanted layers whose thicknesses are orders of magnitude less than the overall thermal diffusion length ,i.e. probed depth. The measurements presented reveal the detection of layers an order of magnitude thinner that those previously reported in the literature.

Chapter 8

Further Research

As the studies of this project were curtailed with respect to the original goals, the first aspect of any further research should be to complete these, i.e. investigate the effects of strain variation on antimony activation and the accompanying effects on strain stability.

Beyond this, the expansion of the processing parameters to include other annealing techniques would be of interest. Examples of possible additional techniques include flash annealing, spike annealing and laser annealing as these techniques are receiving increased industrial interest.

Other possible complimentary work includes the investigation of strained $Si_{1-x}Ge_x$ and strained germanium and their prospects for both n- and p-type device structures. Indeed the issues discussed in relation to μ -Raman spectroscopy's sensitivity to carrier densities are not manifested in germanium due to the increased carrier relaxation time in this material. This makes possible fast unambiguous stress measurements within germanium.

All characterisation techniques discussed in this thesis lend themselves to investigation of germanium, $Si_{1-x}Ge_x$ and indeed III-V semiconductors, thus the current work lays the

ground-work for a broad spectrum of materials. The prospect of the variable lattice constant attainable through manipulation of $Si_{1-x}Ge_x$ VS provides an interesting lattice matching technique for the integration of III-V semiconductors on silicon, with the previously discussed techniques providing the means of stress and defect characterization.

Photoacoustic spectroscopy and the related photoacoustic microscopy (PAM) are relatively under utilized techniques and so many interesting applications remain unexplored. The fact that the technique provides information on the transfer of heat within the sample makes it an extremely useful technique to many industries concerned with this flux, not least the semiconductor industry.

The theoretical treatment used herein is sufficient for the phase response of the current samples, however an expansion is required to deal with additional layers and a distributed thermal source. Further the derivation of such an expression; solving the non-homogenous heat equation consistently with the boundary conditions of temperature and thermal flux equality is a non-trivial prospect. However such an expression would provide the means of investigating a general multi-layer structure.

Investigations of heat transfer in SOI and bonded wafers is of interest, given their current prevalence in semiconductor manufacture an related literature. This investigation could potentially provide feedback resulting in more efficient, cooler devices.

The current samples are blanket treated however using PAM, damage and delamination mapping is additionally possible, this opens the prospect of expanding the techniques to full wafer examination.

In closing, each branch of this thesis has the prospect of providing years of further research, the biggest limiting factors being time and money.

Appendix A

Dynamical Theory of Diffraction

Dynamical theory endeavours to incorporate all the nuances of X-ray diffraction. It does so by solving Maxwell's equations for incident and reflected waves and applying boundary conditions on these solutions. In this way the dynamical theory identifies what waves can sensibly co-exist [75]. It also allows consideration of multiply scattered beams, loss of incident intensity and interference effects.

The kinematical theory, considers each reflection in isolation, as the name suggests, this theory dynamically relates the amplitudes of waves within a wavefield (an amalgamation of all waves within the crystal). Thus the dynamical theory requires concurrent analysis of all waves within the wavefield, and a more specific method of wavevector identification. Dynamical theory also introduces additional wavevector magnitude considerations (elucidated in chapter A.4). For these reasons two major changes are made to the indexing scheme of the previous section.

The first change relates to the additional wavevector magnitude considerations necessary within dynamical theory. In order to avoid confusion between these newly defined dynamical

wavevectors and those defined in the previous section, capital "**K**" will be used (in the instances in which lower case "**k**" is used, this refers to the wavevector as previously defined).

Secondly in order to be able to identify and index individual scattered waves independently, the general $\mathbf{k}_s$ term of the previous section is replaced with the more specific $\mathbf{K}_h$ where the vector $\mathbf{h}$ replaces $\Delta\mathbf{k}$ (the latter substitution is purely in the interests of concision and clarity due to $\mathbf{k}$'s retention of its previous definition).

Finally, a full treatment of dynamical theory and its implications is beyond the scope of this thesis (full accounts can be found in references [75], [79] and [76]) however some of the more fundamental aspects required for later reference will be presented in the following section.

A.1 Electric Susceptibility

X-ray scattering occurs through the excitation of oscillating dipole moments, the spatial distribution of scattering events is related to the electronic density distribution $\rho(\mathbf{r})$, and the scattering strength is determined by the electric susceptibility, χ, a measure of the polarizability of the material. Far from an absorption edge, the electric susceptibility is given classically by [75]:

$$\chi(\mathbf{r}) = -\frac{e^2\rho(\mathbf{r})}{4\pi^2\epsilon_0\nu^2 m} = \frac{-R\lambda^2\rho(\mathbf{r})}{\pi} \tag{A.1}$$

where ν is the frequency of the electromagnetic wave and $\mathrm{R} = e^2/(4\pi\epsilon_0 \mathrm{m}c^2)$ is the classical radius of the electron. χ is a triply periodic function within a crystalline material and can therefore be expressed as a Fourier series:

$$\chi = \sum_h \chi_h \exp(2\pi j\mathbf{h}\cdot\mathbf{r}) \tag{A.2}$$

where the Fourier coefficients of the expansion, χ_h, are proportional to the previously defined structure factor.

A.2 Propagation Equation

The propagation equation for waves traveling within the crystal is obtained by solving Maxwell's equations:

$$\begin{aligned} \nabla \times \mathbf{E} &= -\mu_0 \frac{\partial \mathbf{H}}{\partial t} \\ \nabla \times \mathbf{H} &= \frac{\partial \mathbf{D}}{\partial t} \\ \nabla \cdot \mathbf{D} &= 0 \\ \nabla \cdot \mathbf{B} &= 0 \end{aligned} \tag{A.3}$$

where $\mathbf{E}$ and $\mathbf{D}$ are the electric field and electric displacement; $\mathbf{H}$ and $\mathbf{B}$ are the magnetic field and magnetic induction and μ_0 is the magnetic permeability of free space. We also note the material relations:

$$\begin{aligned} \mathbf{D} &= \epsilon \mathbf{E} \\ \mathbf{B} &= \mu \mathbf{H} \end{aligned} \tag{A.4}$$

where μ and ϵ are the magnetic permeability and dielectric constant of the material. By eliminating $\mathbf{H}$ from the first two equations in (A.3) (using the identity $\epsilon_0 \mu_0 = \frac{1}{c^2}$, where c is the speed of light) and solving for $\mathbf{D}$, one arrives at the propagation equation for an electromagnetic wave in a crystalline material [75]:

$$\Delta \mathbf{D} + \nabla^2 \times \chi \mathbf{D} + 4\pi^2 k^2 \mathbf{D} = 0 \tag{A.5}$$

Von Laue chose to express this equation in terms of the electric displacement rather than the electric field and it is this convention which is followed here. This choice was made on the

basis that the spatially varying electric susceptibility within the crystal renders $\Delta \cdot \mathbf{E}$ non-zero ($\mathbf{E} = \frac{\mathbf{D}}{\epsilon}$, where $\epsilon = \epsilon_0(1+\chi)$), whereas $\Delta \cdot \mathbf{D}$ remains zero, as the two are proportional, no detail is lost [75].

The solutions to (A.5) are of the form of an infinite sum of plane waves with amplitudes $\mathbf{D}_h$ and wavevectors $\mathbf{K}_h$ [75],

$$\mathbf{D}(\mathbf{r}) = \sum_h \mathbf{D}_h \exp(-2\pi i \mathbf{K}_h \cdot \mathbf{r}) \tag{A.6}$$

A.3 Fundamental Equations of Dynamical Theory

The fundamental equations of dynamical diffraction theory arise through the combination of equations (A.2), (A.5) and (A.6). This combination leads to a sum of an infinite number of terms which is equivalent to an infinite system of linear equations, these constitute the fundamental equations of dynamical diffraction [75]:

$$\mathbf{D}_{hj} = \frac{K_{hj}^2}{K_{hj}^2 - k^2} \sum_{\mathbf{h'}} \chi_{h-h'} \mathbf{D}_{\mathbf{h'}[h]j} \tag{A.7}$$

This system of equations relates the amplitude of each wave in the wavefield (associated with **h** and defined by (A.6)) to all others. In (A.7), $\chi_{\mathbf{h}-\mathbf{h'}}$ is the Fourier coefficient of the electric susceptibility associated with the reciprocal lattice vector **h** - **h'** (where **h'** is a reference wavevector) and $\mathbf{D}_{\mathbf{h'}[h]j}$ is the projection of $\mathbf{D}_{\mathbf{h'j}}$ onto a plane normal to $\mathbf{K}_{hj}$ (this last term accounts for polarization effects). The j subscript identifies a particular solution to (A.6)

In order to simplify the system of (A.7) we consider a case in which $\chi_{\mathbf{h}-\mathbf{h'}}$ equals zero for all but two beams. This simplification can be justified by considering the Ewald sphere, where, in general, a maximum of two reciprocal-lattice points lie on the sphere's surface in

any given configuration. Under this condition (A.7) becomes [75]:

$$\begin{aligned} 2K_iD_i - kC\chi_hD_G &= 0 \\ -kC\chi_hD_i + 2X_hD_G &= 0 \end{aligned} \tag{A.8}$$

where

$$\begin{aligned} X_i &= K_i - nk \\ X_h &= K_h - nk \end{aligned} \tag{A.9}$$

In (A.8) C is equal to 1 if $\mathbf{D}_h$ is perpendicular to the $\mathbf{K}_i\mathbf{K}_h$ plane and equal to $cos\,(2\theta)$ if it lies in this plane. The significance of X_i and X_h will become clear when dispersion surfaces are considered.

A.4 Dispersion Surfaces

The dispersion surface is a surface of constant energy, mapped out by the locus of tiepoints (points of intersection) of the $\mathbf{K}_i$ and $\mathbf{K}_h$ vectors in reciprocal space. In the case of the two-beam situation (described by (A.8)) this tiepoint locus generates two intersecting spheres centered on the reciprocal lattice points O and H and an ajoining surface between them. Within the crystal, the spheres are of radius nk (where n is the refractive index), figure A.1 shows the dispersion surface [75].

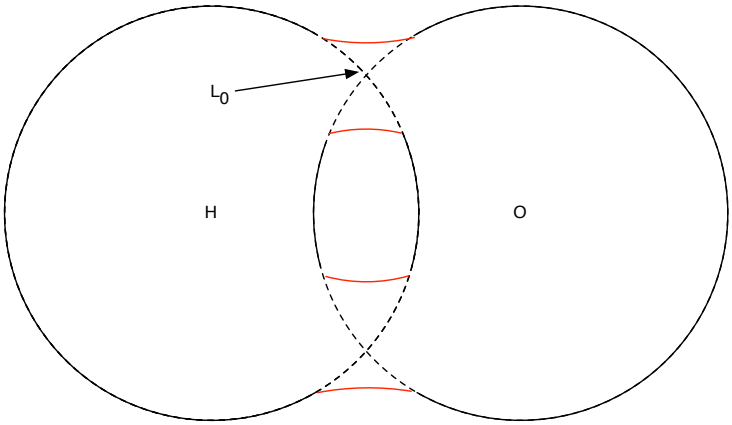

Figure A.1: Dispersion surface of the two-beam dynamical theory. When the tiepoint lies on either circle away from the intersection point, only one beam propagates within the crystal. In order for both incident and diffracted beams to be stimulated simultaneously, the tiepoint must lie on the intersection surface, marked in red.

Trivial solutions to the wavefield involve the tiepoint existing on either of the spheres far from the intersection region. In these cases only one wave propagates. In order to obtain non-trivial solutions, the tie point must lie on the intersection surface, the equation for this surface is given be setting the determinant of (A.8) equal to zero [75]:

$$X_i X_h = {}^{k^2 C^2 \chi_h \chi_{\bar{h}}}/_4 \tag{A.10}$$

The point L_0 in figure A.1 describes the criteria required for kinematical diffraction (ignoring for a moment the radial length differences introduced by the refractive index). Dynamical theory however, introduces a more realistic range of tiepoint positions which can give rise to diffraction of varying intensity. The additional length of the reciprocal lattice vectors, $\mathbf{X}_i$ and $\mathbf{X}_h$, depicted in figure B.1 [75] define the distances between the respective sphere and the tiepoint.

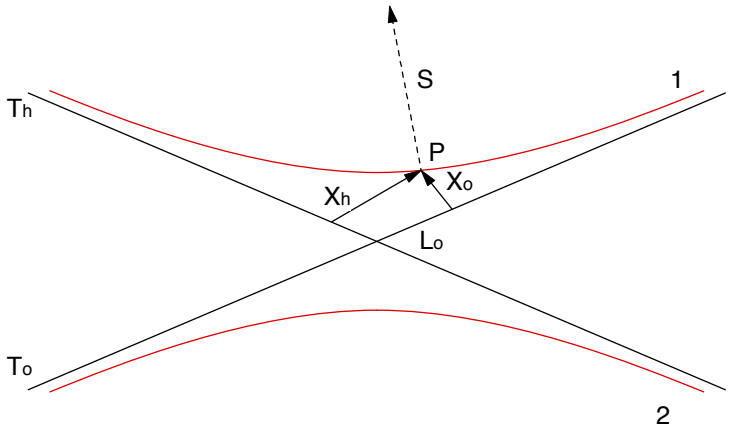

Figure A.2: Dispersion surface of the two-beam dynamical theory. When the tiepoint lies on either circle away from the intersection point, only one beam propagates within the crystal. In order for both incident and diffracted beams to be stimulated simultaneously, the tiepoint must lie on the intersection surface, marked in red.

In the two-beam case currently considered, the wavefield is defined by the wavevector tiepoint and therefore by the incident and diffracted vectors $\mathbf{K}_i$ and $\mathbf{K}_h$. The amplitude ratio of these waves is by [75] :

$$\xi = \frac{|D_h|}{|D_i|} = \frac{2X_0}{kC\chi_{\bar{h}}} = \frac{-2\pi V K_i}{R\lambda C F_{\bar{h}}} \tag{A.11}$$

A.5 Solution to Dynamical Theory of Diffraction

In order to calculate the diffracted intensity for a given angle of incidence, one must determine the wavevector tiepoints which are excited. In order to identify these, it is necessary to apply continuity boundary conditions to the electric and magnetic fields at the crystal/vacuum

interface:

$$\begin{aligned} \mathbf{E}_{T1} &= \mathbf{E}_{T2} \\ \mathbf{D}_{N1} &= \mathbf{D}_{N2} \\ \mathbf{H}_{T1} &= \mathbf{H}_{T2} \\ \mathbf{B}_{N1} &= \mathbf{B}_{N2} \end{aligned} \tag{A.12}$$

where the N and T subscripts denote normal and transverse components respectively.

In vacuum, the incident and reflected waves are defined by the wavevector $\mathbf{k}_i$ and $\mathbf{k}_s$ and the tiepoint M, which lies on spheres of radius k centered at O and H respectively. The application of the boundary conditions implies that the excited tiepoints are defined by the points of intersection of the surface normal passing through M and the dispersion surface, figures A.3 (a) and (b) [75] depict the transmission (Laue) and reflection (Bragg) configurations respectively.

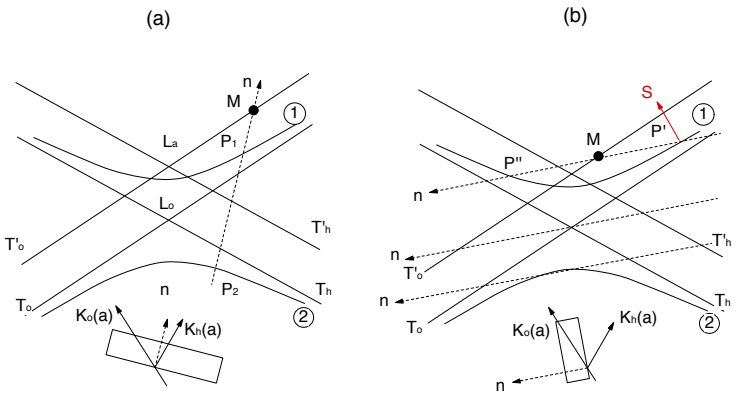

Figure A.3: (a) Reciprocal space representation of transmission dynamical diffraction. Excited tiepoints correspond to the points of intersection of the surface normal passing through M and the dispersion surface. (b) Corresponding reflection configuration.

Having identified the excited tiepoints, the amplitude of the reflected wave is given by [75]:

$$D_{hj} = D_{ij}\left(-S\left(C\right)S\left(\gamma_h\right)\left[\sqrt{F_h F_{\overline{h}}}\Big/F_{\overline{h}}\right]\left[\eta \pm \sqrt{\eta^2 + S\left(\gamma_h\right)}\right]\Big/\sqrt{|\gamma|}\right) \tag{A.13}$$

where the plus sign corresponds to a tiepoint on branch 1 (j=1) (shown in figure A.3) and the minus sign signifies a tiepoint on branch 2 (j=2), $S\left(\gamma_h\right)$ is the sign of γ_h (+1 in transmission geometry and -1 in reflection geometry).

Appendix B

HRXRD Transformations

The processing of the raw $\omega - 2\theta$, ω_{rel} data of the experimental RSM data into analytically meaningful lattice constant and tilt measurements is made relatively straight forward through the use of relative measurements. During pre-measurement calibration, all relevant degrees of freedom are optimized to maximized the intensity of a chosen substrate reflection. The initial parameter space is defined by a priori knowledge of the material in question and its diffraction peak positions. In this case the substrate is silicon with a 224 reflection at $\omega =$ and $2\theta =$. Variations in the precision of sample mounting can result in variation of the actual ω and 2θ values at which the peak is detected and can be nullified by calibrating the experimental peak position to that of theory.

When sitting on the diffraction peak, $\omega - 2\theta$, ω_{rel} are calibrated to zero meaning all measurements are relative to this known standard. The absolute angle values are generated simply by adding the relative experimental values to the a priori calibration values. In calculating the reciprocal lattice dimensions, the $\omega - 2\theta$ values are used, with the ω_{rel} axis bringing the layer into diffraction. Equations B.1 and B.2 relate the experimental measurements to the reciprocal parameters [**?**],

$$\Delta q_{\perp} = \left(4\pi/\lambda\right)(\omega - 2\theta)\cos\theta_B \tag{B.1}$$

$$\Delta q_{||} = \left(4\pi/\lambda\right)\omega_{rel}\sin\theta_B \tag{B.2}$$

$\theta_B\mu_0 t >> 1\mu_0 t\mu_0 t$ [84]

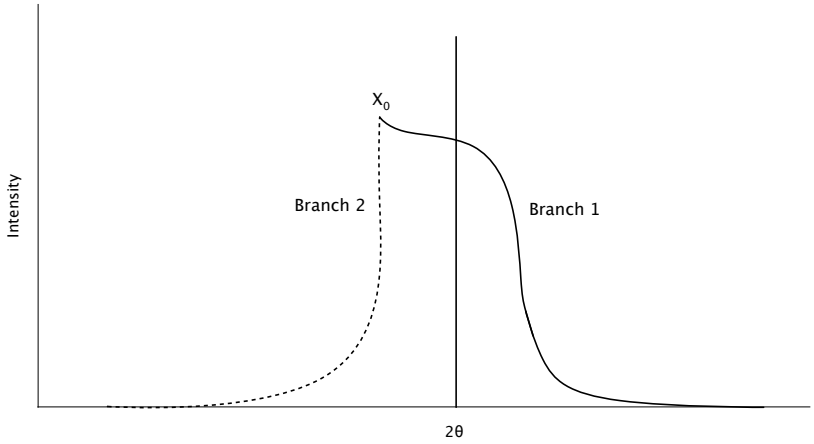

Figure B.1: Rocking curve, indicating the contributions from branches 1 (solid) and 2 (dashed) of the dispersion curve.

The dynamical theory (chapter A)describes the diffraction process by means of a "dispersion" curve. This curve consists of two branches separated in phase by π radians. In the rocking curve of a crystalline material, both branch 1 and branch 2 contribute to the excited beams. This is depicted in figure B.1 where the solid and dashed lines represent the contributions from branches 1 and 2 respectively. The wavefield associated with branch 2, having the nodes of its standing wave located between atomic planes (demonstrated in figure B.2 [139]), experiences greatly reduced absorption.

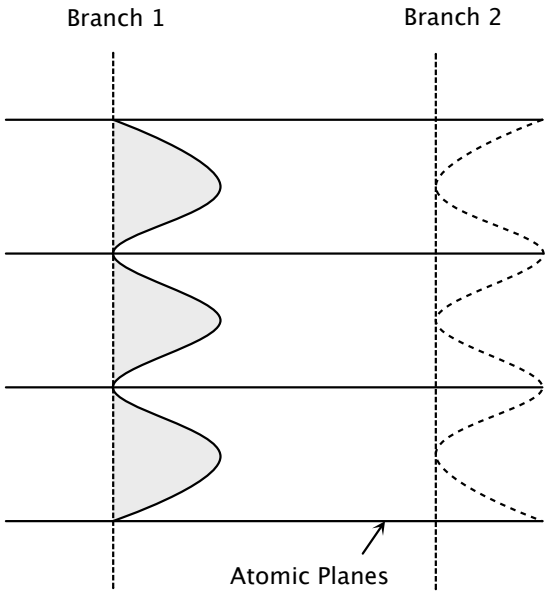

Figure B.2: Standing wave pattern associated with with branches 1 and 2 of the dispersion surface. Branch 2, having nodes located between atomic planes experiences greatly reduced absorption.

As with extinction contrast, the breakdown of this effect in the presence of defects introduces image contrast in the topograph (in this case reducing the diffracted intensity from defect regions).

Appendix C

SXRT Modes of Operation

SXRT experiments can be carried out in 1 of 4 modes of operation. The orientation of the experimental set-up used depends on the location of the defects of interest and the type of contrast most likely to reveal them. Below is a brief description of the 4 experimental configurations.

C.1 Large Area Transmission (LAT)

In this set-up, the dimensions of the incident x-ray beam are extended to a few millimeters in each direction. White beam synchrotron radiation is then incident on one side of the sample, as shown in figure C.1, the x-rays are diffracted as they pass through the sample and the resulting pattern is collected by high resolution x-ray film. This technique investigates the entire sample thickness as the diffracted x-rays must pass through the sample to be recorded.

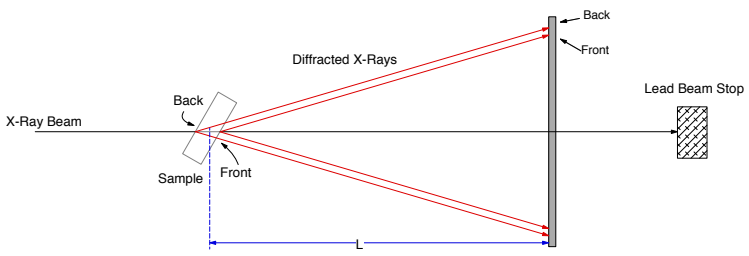

Figure C.1: Experimental set up for large area transmission SXRT.

C.2 Large Area Back Reflection (LABRT)

As described in figure C.2 the LABRT configuration involves incident x-rays passing through a central hole in the detection film, followed by Bragg reflection at the sample's surface and finally detection by high resolution x-ray film. This configuration investigates the surface region of the sample only and the depth which is investigated is determined by the penetration depth of the x-rays associated with the chosen reflection.

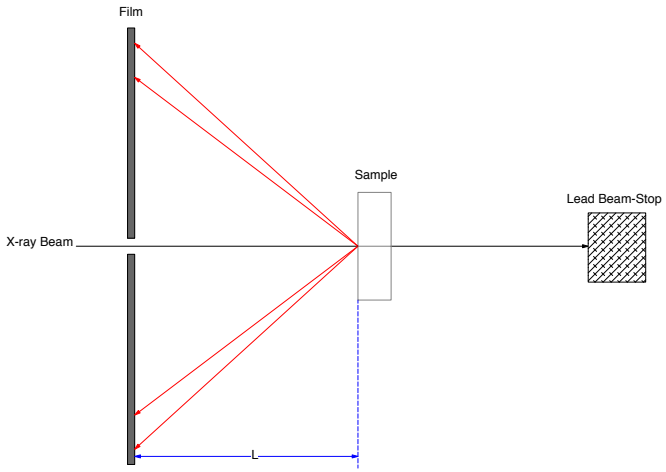

Figure C.2: Experimental configuration for large area back reflection SXRT.

C.3 Section Transmission (ST)

In section topography, the dimensions of the incident beam are reduced to a ribbon, generally on the order of microns in width. As can be seen from figure C.3 one end of the section topograph is the result of diffraction from the front of the sample while the opposite end originates at the back of the sample. Because of this, the spacial intensity distribution resulting from such an exposure gives information analogous to taking a section through the sample.

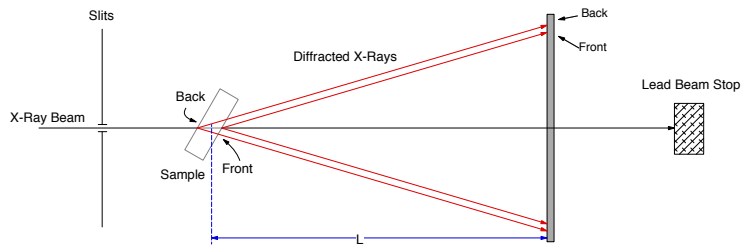

Figure C.3: Experimental configuration for section transmission SXRT

C.4 Back Reflection Section Topography (BRST)

This configuration gives information similar to that of the section transmission with the exception that the section only extends into the sample a distance equivalent to the penetration depth of the reflection being considered. Figure C.4 shows this set-up.

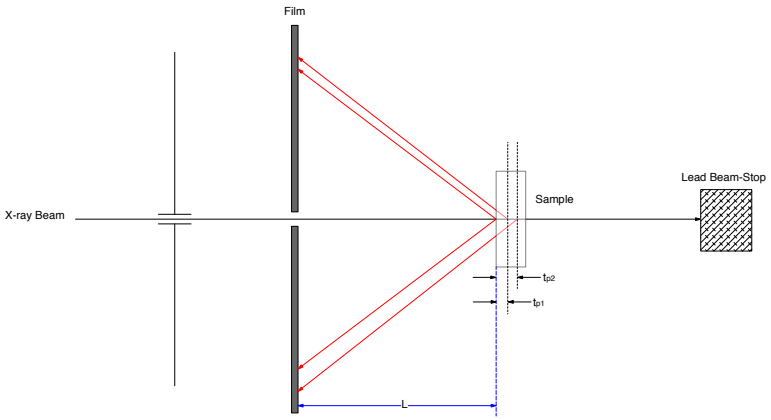

Figure C.4: Experimental configuration for section back-reflection SXRT.

Appendix D

Thermal Thickness

The concept of thermal thickness of a layer, can greatly simplify the nomenclature of photoacoustic analysis. It refers to the layer thickness relative to the thermal diffusion length within that layer. A layer or sample is said to be thermally thick if the thermal diffusion length is less that the thickness. A layer can similarly be described in terms of its optical thickness with an opaque sample being considered optically thick. In these terms a sample or layer can be described in one of four ways.

D.1 Optically & Thermally Thick

In this situation the thickness of the layer is greater than both the optical penetration depth and the thermal diffusion length. In a layered structure, have a surface layer of this description, the surface temperature profile is dominated by the surface layer as no heat from any under-lying layers can reach the surface. In addition to this, the heat generation in any sub-layer is minimal due to the low light intensity.

In the optical extreme of this case, where the optical penetration depth becomes negligible, the thermal energy can be considered to originate entirely at the sample surface. This situation is commonly known as Photoacoustic saturation and the surface temperature profile becomes purely a function of the sample's thermal properties.

D.2 Optically Thin & Thermally Thick

Although in this case an appreciable intensity of light reaches the under-lying layers, the fact that the thermal diffusion length is shorter than the layer thickness results in no contributions to the surface temperature profile from the sub-layers.

D.3 Optically & Thermally Thin

In this case the underlying layers can contribute to the surface temperature profile as as appreciable intensity of light penetrates the top layer, and the sufficiently long thermal diffusion length provides a route back to the surface for the heat.

D.4 Optically Thick & Thermally Thin

Although this configuration provides a mechanism for transporting heat back to the surface from any under-lying layers, the fact that the light intensity penetrating the top layer is insubstantial, means that little or no signal will be detected from this region of the sample.

Bibliography

[1] M. Chu, Y. Sun, U. Aghoram, S. E. Thompson, *Annu. Rev. Mater. Res.*, **39**, pp. 203-229 (2009). 1

[2] R. G. Arns, *Eng. Sci. and Edu. J.*, **7**, pp. 233-240 (1998). 2

[3] M. Ieong, B. Doris, J. Kedzierski, K. Rim, and M. Yang, *Science*, **306**, pp. 2057-2060 (2007). 3

[4] G. E. Moore, *Electronics*, **38** (1965). 3

[5] G. E. Moore, *Inter. Elec. Dev. Meet.*, **11** (1975). 3

[6] Intel, *Microprocessor Chart* (Intel). 3

[7] F. F. Fang, A. B. Fowler, *Phys. Rev.* (3), **169**, pp. 619-631 (1968). 5

[8] G. Abstreiter, H. Brugger, T. Wolf, H. Jorke, and H. J. Herzog, *Phys. Rev. Lett.*, **54** (22), pp. 2441-2444 (1985). 6

[9] E. A. Fitzgerald, Y. H. Xie, M. L. Green, D. Brasen, A. R. Kortan, *Mat. Res. Soc. Symp. Proc.*, **220**, 211 (1991). 6

[10] F. Schaffler, D. Tobben, H. Herzog, G. Abstreiter, and B. Hollander, *Semicon. Sci. Tech.*, **7**, pp. 260-266 (1992). 6

[11] M.T. Currie, C.W. Leitz, T.A. Langdo, G. Taraschi, E.A. Fitzgerald, D.A. Antoniadis, *J. Vac. Sci Technol. B*, **19** (6), pp.2268 - 2277 (2001) 6, 145

[12] J. Welser, J. L. Hoyt, J. F. Gibbons, *Elect. Dev. Meet.*, pp. 1000-1220 (1992). 6

[13] J. Welser, J. L. Hoyt, S. Takagi, J. F. Gibbons, *IEEE Trans. Elect. Dev.*, pp. 373-376 (1994). 7

[14] K. Rim, J. L. Hoyt, and J. F. Gibbons, *IEEE Trans. Elect. Dev.*, pp. 707-710 (1998). 7

[15] D. K. Nayak, J. C. S. Woo, J. S. Park, K. L. Wang, and K. P. MacWilliams, *Appl. Phys. Lett.*, **62** (22), 2853-2855 (1993). 7

[16] D. Monroe, Y. H. Xie, E. A. Fitzgerald, P. J. Silverman, G. P. Watson, *J. Vac. Sci. Technol. B***11** (4), pp. 1731-1737 (1993). 7

[17] K. Ismail, F. K. LeGoues, K. L. Saenger, M. Arafa, J. O. Chu, P. M. Mooney, B. S. Meyerson, *Phys. Rev. Lett.*, **73** (25), pp. 3447-3452 (1994). 7

[18] D. K. Nayak, K. Goto, A. Yutani, J. Murota, Y. Shiraki, *IEEE Trans. Elect. Dev.*, **43** (10), pp. 1709-1716 (1996). 7

[19] G. Hock, E. Kohn, C. Rosenblad, H. von Kanel, H. Herzog, and U. Konig, *Appl. Phys. Lett.*, **76** (26), pp. 3920-3922 (2000). 7

[20] M. L. Lee, C. W. Leitz, Z. Cheng, A. J. Pitera, T. Langdo, M. T. Currie, G. Taraschi, E. A. Fitzgerald, D. A. Antoniadis, *Appl. Phys. Lett.*, **79** (20), pp. 3344-3346 (2001). 7, 32

[21] P. Kringhoj, A. N. Larsen, S. Y. Shirayev, *Phys. Rev. Lett.*, **76** (18) pp. 3372-3375 (1996) 8, 38

[22] N. E. B. Cowern, P. C. Zalm, P. van der Sluis, D. J. Gravesteijn, W. B. de Boer, *Phys. Rev. Lett.*, **72** (16), pp. 2585-2588 (1994). 8, 37

[23] B. Sadigh, T. J. Lenosky, M. Caturla, A. A. Quong, L. X. Benedict, T. D. de la Rubia, M. M. Giles, M. Foad, C. D. Spataru, S. G. Louie, *Appl. Phys. Lett.*, **80** (25), 4738-4740 (2002). 8, 11, 34

[24] N. S. Bennett, H. H. Radamson, C. S. Beer, A. J. Smith, R. M. Gwilliam, N. E. B. Cowern, and B. J. Sealy, *Thin Solid Films*, **517** (1), 331-333 (2008). 8, 55

[25] N. S. Bennett, A. J. Smith, R. M. Gwilliam, R. P. Webb, B. J. Sealy, N. E. B. Cowern, L. O'Reilly, and P. J. McNally, in , *J. Vac. Sci. Technol. B*, **26** (1), p. 391-395. 8, 48, 49, 55

[26] C. Ahn, N. Bennett, S. T. Dunham, N. E. B. Cowern, *Phys. Rev. B*, **79**, 073201 (2009). 8, 35, 36, 44, 53, 89

[27] A. D. Capewell, T. J. Grasby, T. E. Whall, and E. H. C. Parker, *Appl. Phys. Lett.*, **81** (25), 4775-4777 (2002). 8, 26, 88

[28] *ITRS, 2007 Edition* (International Technological Roadmap for Semiconductors, 2007). 8, 40, 147

[29] A. R. Denton, N. W. Ashcroft, *Phys. Rev. A*, **43**, 3161 (1991). 10

[30] J. P. Dismukes, L. Ekstrom, R. J. Paff, *J. Phys. Chem.*, **68** (6), 3021-3164 (1964). 10

[31] E. Kasper, *Appl. Sur. Sci.***224**, 3-8 (2004). 10, 11, 16

[32] J. W. Matthews, A. E. Blakeslee, *J. Cryst. Grow.***27**, 118-125 (1974). 11, 12

[33] R. People, *IEEE J. Quant. Elect.*, **22** (9), pp. 1696-1710 (1986). 11, 13

[34] P. M. J. Maree, J. C. Barbour, J. F. van der Veen, K. L. Kavanagh, C. W. T. Bulle-Lieuwma, M. P. A. Viegers, *J. Appl. Phys.*, **62** (11), 4413-4420 (1987). 11, 12, 15, 17, 39

[35] S. J. Zhou, D. L. Preston, P. S. Lomdahl, D. M. Beazley, *Science*, **279**, 1525-1527 (1998). 12

[36] J. Weertman, J. R. Weertman, *Elementary Dislocation Theory* (The Macmillan Company, New York, 1964). 12, 13

[37] D. Hull and D. J. Bacon, *Introduction to Dislocations* (Elsevier, Oxford, 2001). 12

[38] C. G. Van de Walle, R. M. Martin, *Phys.Rev.B* (8), **34**, 5621-5634 (1986). 12

[39] A. G. Cullis, *MRS Bulletin*, **21**, 21 (1996). 16

[40] L. J. Nash, *Growth and Characterisation of Terrace Graded Virtual Substrates with Si(1-x)Ge(x) 0.15-x-1* (University of Warwick, 2005). 16

[41] A. Sakai, K. Sugimoto, T. Yamamoto, M. Okada, H. Ikeda, Y. Yasuda, S. Zaima, *Appl. Phys. Lett.***79** (21), 3398-3400 (2001). 16

[42] L. B. Freund, S. Suresh, *Thin Film Materials* (Cambridge University Press, Cambridge, 2003). 16, 21

[43] F. K. LeGoues, B. S. Meyerson, J. F. Morar, and P. D. Kirchner, *J. Appl. Phys.*, **71** (9), 4230-4243 (1992). 22, 25

[44] F.K. LeGoues, P.M. Mooney, J.O Chu, *Appl. Phys. Lett.*, **62** (2) pp. 140-142 (1993) 26

[45] F.Riesz, *J. Vac. Sci. Technol. A*, **14** (2) pp. 425-429 (1996) 26, 28

[46] D.J. Paul, *Semicond. Sci. Technol*, **19**, pp. R75-R108 (2004). 30

[47] T. Vogelsang, K. R. Hofmann, *Appl. Phys. Lett.*, **63**, 186 (1993). 31, 32, 33

[48] L. Hoyt, H. M. Nayfeh, S. Eguchi, I. Aberg, G. Xia, T. Drake, E. A. Fitzferald, D. A. Antoniadis, in *Intl. Elect. Dev. Meeting Technical Digest*, (IEEE, 2002), p. 23. 31, 34

[49] M. V. Fischetti, S. E. Laux, *Phys. Sci.*, RC 20398 (1996). 32

[50] D. Long, *Phys. Rev.*, **120** (6), pp. 2024-2032 (1960). 33, 34

[51] W. A. Harrison, *Phys. Rev.*, **104** (5), 1281-1290 (1956). 34

[52] J. Adey, R. Jones, P. R. Briddon, *J. Phys.: Cond. Mat.*, **16**, pp. 9117-9126 (2004). 34, 35

[53] M. Diebel, in *Simulation of Semiconductor Processes and Devices - SISPAD* (2004), pp. 37. 35

[54] P. Fahey, G. Barbuscia, M. Moslehi, R. W. Dutton, *Appl. Phys. Lett.*, **46** (8), pp. 784-786 (1985). 37

[55] D. A. Antoniadis, I. Moskowitz, *J. Appl. Phys.*, **53** (10), pp. 6788-6796 (1982). 37

[56] P. Pichler, H. Ryssel, R. Ploss, C. Bonafos, A. Claverie, *J. Appl. Phys.*, **78** (3), pp. 1623-1629 (1995). 37

[57] N. E. B. Cowern, *J. Appl. Phys.*, **64** (9), pp. 4484-4490 (1988). 37

[58] A. Ural, P. B. Griffin, J. D. Plummer, *J. Appl. Phys.*, **85** (9), pp. 6440-6446 (1999). 37

[59] M. Tang, L. Colombo, J. Zhu, T. Diaz de la Rubia, *Phys. Rev. B* (21), **55** (14), pp. 279-289 (1997). 38

[60] A. N. Larsen, N. Zangenberg, J. Fage-Pedersen, *Mat. Sci. Eng. B*, **124-125**, pp. 241-244 (2005). 38

[61] P.R Chidambaram, C. Bowen, S. Chakravarthi, C. Machala, R. Wise, *IEEE Trans. Electron Dev.*, **53** (5). pp. 944 - 964 (2006) 38, 145

[62] J. Ziegler, *Partical Interactions with Matter* (James Ziegler, 2010). 41, 139

[63] R. Duffy, T. Dao, Y. Tamminga, K. V. D. Tak, F. Roozeboom, and E. Augendre, *Appl. Phys. Lett.*, **89**, 071915 (2006). 42

[64] J. Narayan and O. W. Holland, *Appl. Phys. Lett.*, **41**, 239 (1982). 42, 43

[65] L. Csepregi, J.W. Mayer, T.W. Sigmon, *Appl. Phys. Lett.*, **29**, 92-93 (1976) 43

[66] N.S. Bennett, A.J. Smith, R.M. Gwilliam, R.P. Webb, B.J Sealy, N.E.B. Cowern, L.O'Reilly, P.McNally, *J. Vac. Sci. Technol. B***26** (1), pp. 391-395 (2008). 44

[67] Y.Lai, N.S. Bennett, C. Ahn, N.E.B. Cowern, N. Cordero, J.C. Greer, *Solid State Elect.*, **53**, pp. 1173-1176 (2009). 44, 54

[68] N.S. Bennett, C. Ahn, N.E.B. Cowern, P Pichler, *Solid State Phenomena*, **156-158** pp. 173-180 (2010). 44

[69] N. S. Bennett, N. E. B. Cowern, A. J. Smith, R. M. Gwilliam, B. J. Sealy, L. O'Reilly, P. J. McNally, G. Cooke, and H. Kheyrandish, *Appl. Phys. Lett*, **89**, pp. 182122 (2006) 44

[70] N.S. Bennett, PhD. Thesis, *Ultrashallow Junctions for Strain-Engineered NMOS Devices*, University of Surrey (2008) 45, 48

[71] L. J. van der Pauw, *Philips Res. Repts.* **13** (1), pp. 1-9 (1958) 46

[72] http://www.eaglabs.com/training/tutorials/sims_theory_tutorial/rsf.php 52

[73] W. Freidrich, P. Knipping, P. von Laue. *Proc. Bav. Acad. Sci.*. 1912. 59

[74] W.L. Bragg. *Proc. R. Soc. London, Ser. A*. 1913. 59

[75] A. Authier, *Dynamical Theory of X-Ray Diffraction* (Oxford University Press Inc., New York, 2001). 60, 62, 66, 186, 187, 188, 189, 190, 191, 192, 193, 194

[76] A. Guinier, *X-Ray Diffraction In Crystals, Imperfect Crystals, and Amorphous Bodies* (Dover Publications, New York, 1994). 62, 97, 187

[77] C. Kittel. *Introduction to Solid State Physics*, 7th Edition. (Wiley & Sons, Inc., USA, 1996). 64, 65, 66, 67, 114, 115, 118

[78] R. W. James, *The Optical Principles of the Diffraction of X-Rays* (Ox Bow Press, Woodbridge, Connecticut, 1954). 66

[79] D. K. Bowen and B. K. Tanner, *High Resolution X-Ray Diffractometry and Topography* (Taylor & Francis Ltd, London, 1998). 68, 69, 70, 187

[80] Unpublished 71, 73, 74

[81] M. Erdtmann, T.A. Langdo, *J. Mater. Sci.: Mater. Elect.*, **17**, pp.137-147 (2006) 79, 80, 82

[82] P. Van derSluis, *J. Phys. D: Appl. Phys.*, **26**, pp. A188-A191 (1993) 84

[83] S.B. Samavedam, W.J. Taylor, J.M. Grant, J.A. Smith, P.J. Tobin, A. Dip, A.M. Philips, R. Liu, *J. Va. Sci.Technol. B*, **17**, 4, pp. 1424-28 (1999). 88

[84] D. R. Black, *X-Ray Topography* (National Institute of Standards and Technology, Washington DC, 2004) 95, 98, 196

[85] A. Authier, S. Lagomarsino, B. K. Tanner, *X-Ray and Neutron Dynamical Diffraction Theory and Applications* (Plenum Press, New York, 1996). 95, 96, 97

[86] T. Tuomi, K. Naukkarinen, and P. Rabe, *Phys. Stat. Sol. (a)*, **25**, pp. 93-106 (1974). 95

[87] T. Baumbach, J. Gottlicher, and M. Hagelstein, *ANKA Instrumentation Book* (ANKA Angstroemquelle Karlsruhe, Eggenstein Leopoldshafen, Germany, 2006). 99

[88] Huang, X. R. *J. Appl. Cryst.***43**, 926-928 (2010). 102

[89] R.Rantamaki, T. Tuomi, P.J. McNally, J.Curley, A. Danilewsky, *J. X-ray Sci. Tech.*, **8**, pp.159-169 (1998). 102

[90] http://henke.lbl.gov/optical_constants/atten2.html 102

[91] A. Smekal, *Naturwiss***11**, pp. 873 (1923). 111

[92] C. V. Raman, *Nature***121**, pp. 721 (1928). 111

[93] S. P. S. Porto D. L. Wood, *J. Opt. Soc. Am.*, **52**, pp. 251 (1962). 111

[94] H. Baranska, A. Labudzinska, J. Terpinski, *Laser Raman Spectrometry: analytical applications* (Ellis Horwood Limited, Chichester, 1987). 111, 116

[95] E. Anastassakis, *J. Appl. Phys.*, **82** (4), 1582-1591 (1997). 111, 134

[96] J. Chen and I. De Wolf, *IEEE Trans. Comp. Pack. Techol***28** (3), 484-492 (2005). 111

[97] P. M. A. Sherwood, *Vibrational Spectroscopy of Solids* (University Press, Cambridge, 1972). 112

[98] B.P. Pandey, B. Dayal, *J. Phys. C.: Sol. Stat. Phys.*, **6**, pp. 2943-2946 (1973). 113

[99] W. H. Weber, R. Merlin, *Raman Scattering in Material Science* (Springer, Berlin, Heidelberg, New York, 2000). 114, 115

[100] E. Smith, D. Dent, *Modern Raman Spectroscopy - A Practical Approach* (Wiley, England, 2005). 119

[101] S. Ganesan, A. A. Maradudin, J. Oitmaa, *Ann. of Phys.*, **56**, 556 (1970). 121

[102] I. De Wolf, *Semi. Sci. and Tech.*, **11**, 139 (1996). 121, 122, 134

[103] R. W. Keyes, *IBM Journal of Research and Development*, pp. 266 (1961). 122

[104] F. Cerdeira, M. Cardona, *Phys. Rev. B*, **5**, pp. 1440 (1972). 123, 143

[105] J. C. Hensel, H. Hasegawa, and M. Nakayama, *Phys.Rev.*, **138**, pp. A225 (1965). 124

[106] V. Sverdlov and S. Selberherr, *Sol. Stat. Elect.*, **52**, pp. 1861 (2008). 124, 125

[107] I. De Wolf, H. E. Maes, and S. K. Jones, *J. Appl. Phys.*, **79**, pp. 7148 (1996). 125, 128, 134, 135

[108] D. Rouchon, V. Destefanis, J. Hartmann, A. Crisci, and M. Mermoux, *ECS Trans*, **16**, pp. 203 (2008). 125

[109] D. E. Aspnes, A. A. Studna, *Phys. Rev. B*, **27** (2), 985-1009 (1983). 128

[110] Omega Optical, *Filters for Raman Spectroscopy* (2010). 129, 130

[111] Horiba Jobin Yvon, *HR800 User Manual* (2008) 131

[112] K. Horan, L. O'Reilly, N.S. Bennett, P.J. McNally, B.J. Sealy, N.E.B. Cowern, *Optimization of UV-Raman spectroscopy analysis of ultra-shallow junctions in strained silicon*, in: IOM3 3rd International Conference on Nanomaterials and Nanomanufacturing, 2007. 132

[113] L. O'Reilly, N.S. Bennett, P.J. McNally, B.J. Sealy, N.E.B. Cowern, A. Lankinen, T.O. Tuomi, *J. Mat. Sci: Mater Electron*, **19**, pp. 305-309 (2008). 135

[114] H. Richter, Z. P. Wang, L. Ley, *Solid State Comm.*, **39** (5), pp. 625-629 (1981). 136

[115] I. H. Campbell, P.M. Fauchet, *Solid State Comm.*, **58** (10) pp. 739-741 (1986). 136, 137

[116] J. Macia, E. Martin, A. Perez-Rodriguez, J. Jimenez, J.R. Morante, B. Aspar, J. Margail, *J. Appl. Phys.*, **82**, (8) pp. 3730-3735 (1997). 137

[117] X. Huang, F. Ninio, L. J. Brown, *J. Appl. Phys*, **77** (1) pp. 5910-5915 (1995). 139

[118] K. R. C. Mok, M. Jaraiz, I. Martin-Bragado, J. E. Rubio, P. Castrillo, R. Pinacho, and J. Barbolla, M. P. Srinivasan, *J. Appl. Phys*, **98**, pp. 046104 (2005) 139, 141

[119] M. Chandrasekhar, J. B. Renucci, and M. Cardona, *Phys. Rev. B*, **17**, 1623 (1978). 142, 143

[120] Insert reference! 151

[121] A. Rosencwaig and A. Gersho, *J. Appl. Phys.*, **47**, pp. 64 (1976). 151, 153, 155, 156

[122] A.G. Bell, *Philos. Mag.*, **11**, pp. 510 (1881). 151

[123] W.H. Preece, *Proc. R. Soc. London*, **31**, pp. 506 (1881). 151

[124] A. Rosencwaig and A. Gersho, *Science*, **190**, pp. 556 (1975). 152, 157

[125] J.A. Balderas-Lopez and A. Mandelis, *Rev. Sci Instr.*, **74**, pp. 5219 (2003). 152

[126] F.A. McDonald and G.C. Wetsel Jr., *J. Appl. Phys.*, **49**, p. 2313 (1978). 152, 162

[127] F.A. McDonald, *Appl. Phys. Lett.*, **36**, pp. 123 (1980). 152, 163

[128] A. Mandelis, *Physics Today*, **August**, pp.29 (2000). 152

[129] D. P. Almond P, *Absorption in a thin surface* (Chapman & Hall, 1996), p. 45. 158, 160

[130] F.A. McDonald, *J. Appl. Phys.*, **52**, pp. 381 (1980). 158, 163

[131] A. Othonos, C. Christofides, and A. Mandelis, *Appl. Phys. Lett.* , **69**, pp. 821 (1996). 159

[132] F.A. McDonald, *Am. J. Phys.*, **48**, pp. 41 (1980). 162

[133] F.A. McDonald, *J. Phys.*, **44** (10), C6-21 (1986). 163

[134] A. Mandelis, *IEEE Trans. Ultrason. Ferroel. Freq. Con.*, **5**, vol. 33, pp. 590-614 (1986). 167

[135] U. Zammit, K.N. Madhusoodanan, M. Marinelli, F. Scudieri, R. Pizzoferrato, F. Mercuri, E. Wendler, W. Wesch, *Phys. Rev. B.*, **49**, vol 20, pp. 14332-14330 (1994). 167, 176

[136] B. S. W. Kuo, J. C. M. Li, A. W. Schmid, *Appl. Phys. A*, **55**, pp.289-296 (1992) 171, 174

[137] U. Zammit, M. Marinelli, F. Scudieri, S. Martellucci, *Appl. Phys. Lett*, **50**, vol 13, pp. 830-832 (1987). 173

[138] http://www.virginiasemi.com/pdf/Optical Properties of Silicon71502.pdf 175

[139] B.W. Batterman, H. Cole, *Rev. Mod. Phys.***36** (3) 681-717 (1964) 196